The University of Nottingham

UNITED KINGDOM • CHINA • MALAYSIA

Compartmentalised signalling and trafficking of CXCR4 and ACKR3

Noemi Karsai
MSc, PharmD

A Thesis Submitted to the University of Nottingham for the Degree of Doctor of Philosophy

July, 2024

I. Declaration

This thesis is entirely the candidate's work. The experiments described in this thesis were performed between October 2020 and November 2023 in the Canals-Lane research group at the Centre of Membrane Proteins and Receptors (COMPARE), University of Nottingham, UK. All experiments were completed solely by the author. Additionally, for completeness of the thesis, a RICS experiment has been included where a different researcher (Dr. Joelle Goulding) performed the experiments before the start of the author's PhD candidature. Express permission was obtained to present this experiment in this thesis, and full credit was given to the experimenter in the appropriate Chapter. No part of this material has been previously submitted for a degree or any other qualification at any university.

II. Abstract

The atypical chemokine receptor 3 (ACKR3) and the C-X-C chemokine receptor type 4 (CXCR4) are known to share the chemokine ligand CXCL12. CXCR4 and ACKR3 involvement in various types of cancer and their tumour environment has also been well-documented. Previous research indicated that, while CXCR4 canonically signals through G proteins, ACKR3 does not couple to G protein and suggested that this atypical receptor functions as a chemokine 'scavenger'. Understanding the dynamic organisation of these receptors at the plasma membrane is crucial because this profoundly influences their signalling capabilities and receptor desensitisation. This thesis explored the membrane dynamics and organisation of CXCR4 and ACKR3 at the plasma membrane using a variety of advanced imaging and spectroscopic techniques. In addition, it provided insight into the roles of G protein-receptor kinases (GRKs) in ACKR3 trafficking.

To begin with, Surface-Alexa Flour 488-labelled SNAP-CXCR4 was used to assess receptor localisation and receptor diffusion parameters by Fluorescence Correlation Spectroscopy (FCS) and Fluorescence Recovery After Photobleaching (FRAP). CXCR4 oligomeric state was investigated with Photon Counting Histogram (PCH) analysis. Membrane diffusion and oligomerisation parameters were compared in basal, agonist (CXCL12) and antagonist (IT1t) treated conditions. CXCR4 diffusion in the plasma membrane did not change upon ligand stimulation but showed a CXCL12-induced increase in oligomerisation and ligand-induced reduction in mobility, suggesting cluster formation.

ACKR3 dynamics and organisation were assessed using labelled SNAP-ACKR3. Confocal imaging already revealed a partial membrane but mainly the intracellular location of ACKR3 in both basal and CXCL12-stimulated conditions. ACKR3 dynamics were studied using FCS, FRAP and Raster Image Correlation Spectroscopy (RICS) which provide diffusion characteristics at different scales. The nanoscale (FCS) and microscale (FRAP) diffusion coefficients of ACKR3 showed significant reduction upon CXCL12 addition, whilst there was no significant change on the macro scale (RICS). The

oligomeric state of the receptor was determined with Photon Counting Histogram (PCH) and Number and Brightness (N&B) analysis showing the presence of distinct oligomeric states of ACKR3, indicating cluster formation in both basal and CXCL12 conditions. Moreover, CXCL12 stimulation led to the reduction of ACKR3 mobility and a decrease in the number of particles on macro scale, suggesting internalisation or higher order oligomerisation and cluster formation.

Furthermore, this study investigated the role of G protein-coupled receptor kinases (GRKs) in the internalisation and trafficking of ACKR3 using CRISPR-Cas9 cells edited to lack GRK expression. Our data suggest that ACKR3 undergoes basal internalisation even in the absence of GRKs. However, GRKs appear to influence post-internalization trafficking of the receptor, as the absence of GRKs shifts ACKR3 towards a degradation (LAMP1-positive) pathway.

In conclusion, the data in this thesis provide insights into the distinct dynamics and organisation of CXCR4 and ACKR3 at the plasma membrane at various spatial scales. Additionally, our findings obtained with GRK depletion cell lines demonstrated a potential GRK role in ACKR3 localisation and trafficking post-internalisation.

III. Publications

Research Papers:

Dekkers S, Comez D, Karsai N, Arimont-Segura M, Canals M, Caspar B, de Graaf C, Kilpatrick LE, Leurs R, Kellam B, Hill SJ, Briddon SJ, Stocks MJ. *Small Molecule Fluorescent Ligands for the Atypical Chemokine Receptor 3 (ACKR3).* ACS Med Chem Lett. 2023 Dec 8;15(1):143-148. doi: 10.1021/acsmedchemlett.3c00469. PMID: 38229752; PMCID: PMC10788940.

Kirchhofer SB, Lim VJY, Ernst S, Karsai N, Julia RG, Canals M, Kolb P, Bünemann M. Differential interaction patterns of opioid analgesics with μ opioid receptors correlate with ligand-specific voltage sensitivity. Elife. 2023 Nov 20;12:e91291. doi: 10.7554/eLife.91291. Epub ahead of print. PMID: 37983079.

Karsai N*, Goulding J*, Soave M, Stoddart L, Kilpatrick LE, Hill SJ, Canals M, Briddon SJ – Methods for the analysis of the chemokine receptor CXCR4 dynamics at the cell membrane - *Manuscript in preparation*

Conference Proceeding:

Karsai N, Goulding J, Briddon SJ, Canals M. *Ligand-induced changes in the plasma membrane organisation of the chemokine receptor CXCR4*. Poster presentation at SoLS UoN PGR Symposium (2022, Nottingham, UK)

Karsai N, Goulding J, Briddon SJ, Canals M. *Ligand-induced changes in the plasma membrane organisation of the chemokine receptor CXCR4*. Poster presentation at 4GPCRnet Conference (2022, Leipzig, GE)

Karsai N, Goulding J, Briddon SJ, Canals M. *Ligand-induced changes in the plasma membrane organisation of the chemokine receptor CXCR4*. Poster presentation at iGPCR conference (2022, Wurzburg, GE)

Karsai N, Goulding J, Briddon SJ, Canals M. *Dynamics and organisation of the chemokine receptor CXCR4 and ACKR3 within the plasma membrane*. Poster presentation at the Gordon Research Conference (2023, Les Diablerets, CH)

Karsai N, Goulding J, Briddon SJ, Canals M. *Dynamics and organisation of the chemokine receptor CXCR4 and ACKR3 within the plasma membrane*. Poster presentation at COMPARE Annual symposium (2023, Birmingham, UK)

Karsai N, Goulding J, Briddon SJ, Canals M. *Dynamics and organisation of the chemokine receptor CXCR4 and ACKR3 within the plasma membrane*. Oral presentation at SoLS UoN PGR Symposium (2023, Nottingham, UK)

Karsai N, Goulding J, Canals M, Briddon SJ. *Plasma membrane organisation and dynamics of CXCR4 and ACKR3.* Oral presentation at ONCORNET 2.0 Final Symposium (2023, Amsterdam, NL)

IV. Acknowledgement

First of all, I would like to thank my amazing supervisors, Prof. Meritxell Canals and Dr Steve Briddon, for making me feel welcome in the lab from the start and for their guidance and great support throughout my PhD. Steve, thank you for introducing me to the world of fluorescence spectroscopy and for brightening up our meetings with your dad jokes. Meri, thank you for the coffee walks during the pandemic and for creating a great lab environment, filled with kind and wonderful people.

I would also like to extend my thanks to other members of the Nottingham ONCORNET team: Prof. Steve Hill, Dr. Laura Kilpatrick, and Dehan Comez. Steve, thank you for your support. To Laura, thank you for your endless kindness and motivation; our chats helped me greatly. To Dehan, thank you for being my ONCORNET 'partner in crime'. I am grateful to Prof. Martine Smit and the ONCORNET 2.0 team for creating an amazing collaborative network. It has been a privilege to be a part of this consortium.

I also want to thank everyone in the Canals/Lane lab and Cell Signalling lab group for being an amazing community. Thank you all for the fantastic lab socials, Christmas dinners, and fuddles. A special thank you to Jackie for teaching me everything in TC and for our coffee chats. To Julie, for your support inside and outside of the lab. To Hannah, for our endless chats and your friendship. To Joelle, for all the training and help with the microscopes. To Kelvin for our lunch breaks and to Lydia, Marieke and Desi for your support even from afar. Also, thanks to Sean, Nikki, James, Simon, Eddy, Lucy, Robert and everyone else for making me feel at home in Nottingham.

Thank you to my family and friends, especially to my sister Anett for believing in me and keeping me going. To my friend Eszti for her visits and countless phone calls. Finally, a massive thank you to George for his unwavering support and motivation, for always being there for me (and pushing me when I needed it), and for making me laugh even through the hardest times.

V. Acronyms and Abbreviations

ΔGRK 2/3	G protein-coupled receptor kinase 2 and 3 knock-out
ΔGRK 5/6	G protein-coupled receptor kinase 5 and 6 knock-out
ΔQGRK	Quadruple G protein-coupled receptor kinase (2/3/5/6) knock-out
2D	Two-dimensional
3D	Three-dimensional
7TM	Seven transmembrane
A3AR	A3 adenosine receptor
AC	Autocorrelation curve
ACKR	Atypical chemokine receptor
ACKR3	Atypical chemokine receptor 3
AP-2	Adaptor protein-2
APC	Antigen-presenting cells
AU	Airy Unit
BG	Benzylguanine
BRET	Bioluminescence resonance energy transfer
BSA	Bovine serum albumin
cAMP	Cyclic AMP
CCP	Clathrin-coated pits
CD14	Cluster of differentiation 14
CME	Clathrin-mediated endocytosis
CPM	Count Per Molecule
CR	Count rate
CRISPR/Cas9	Clustered regularly interspaced palindromic repeat/ CRISPR-associated protein 9
CRS	Chemokine recognition site
CXCR4	C-X-C Chemokine Receptor 4
D	Diffusion coefficient
DAG	1,2-diacylglycerol
DMEM	Dulbecco's modified Eagle's medium
DMSO	Dimethyl sulfoxide
DUB	De-ubiquitinating enzyme

ECL	Extracellular loops
EDTA	Ethylenediamine tetraacetic acid
EEA	Early endosome antigen
EGFR	Epidermal growth factor receptor
ERK	Extracellular signal-regulated kinase
ES	Embryonic stem
FBS	Foetal Bovine Serum
FCS	Fluorescence Correlation Spectroscopy
FLIM	Fluorescence lifetime imaging microscopy
FPR1	Formylpeptide receptor 1
FRAP	Fluorescence Recovery After Photobleaching
G418	Geneticin 418
GABA	Gamma-aminobutyric acid
GAG	Glycosaminoglycan
GEF	Guanyl nucleotide exchange factors
GPCR	G protein-coupled receptor
GRK	G protein-coupled receptor kinase
HBSS	Hank's Balanced Salt Solution
HEK 293	Human embryonic kidney 293
HEK G	Human embryonic kidney Glosensor™
ICAM-1	Intracellular cell adhesion protein 1
ICL	Intracellular loops
IP3	Inositol 1,4,5-trisphosphate
JAK	Janus kinase
k	Offset
KD	Kinase domain
KO	Knock out
LAMP-1	Lysosomal-associated membrane protein 1
LSM	Laser Scanning Microscope
MAPK	Mitogen-activated protein kinase
MMP	Matrix metalloprotease
MOR	μ-opioid receptor
N	Particle number
N&B	Number and Brightness

Nluc	Nanoluciferase
NPY	Neuropeptide Y
PAR1	Protease-activated receptor 1
PBS	Phosphate-buffered saline
PCH	Photon Counting Histogram
PDL	Poly-D-lysine
PEI	Polyethylenimine
PFA	Paraformaldehyde
PH	Pleckstrin Homology
PKA	Protein kinase A
PKC	Protein kinase C
PLC	Phospholipase C
PSF	Point spread function
PtdIns3-Ks	Phosphoinositide 3-kinase
RFP	Red fluorescent protein
RH	Regulator of G protein signalling homology domain
RICS	Raster Image Correlation Spectroscopy
ROI	Region of interest
RPM	Revolution per minute
RT	Room temperature
SDF-1	Stromal cell-derived factor-1
SEM	Standard error of the mean
Squassh	Segmentation and quantification of subcellular shapes
STORM	Stochastic optical reconstruction microscopy
TAS2	Fizzled/taste2
TIFF	Tag Image File Format
TLR2	Toll-like receptor 2
VCAM-1	Vascular cell adhesion protein 1
WT	Wildtype
β2AR	β2-adrenergic receptor

VI. Table of Contents

Chapter 1: General Introduction 14

1.1. G protein-coupled Receptors 15
1.1.1. Classification and Structure 15
1.1.2. Canonical GPCR Signalling 17
1.1.3. G Protein-Coupled Receptor Kinases (GRKs) 19
1.1.4. β-arrestins 19
1.1.5. Receptor Trafficking 20

1.2. Chemokines and Chemokine Receptors 22
1.2.1. Chemokines 22
1.2.2. Chemokine Receptors 24
1.2.3. Physiological Functions of Chemokine and Chemokine Receptors 27

1.3. CXCR4 and ACKR3 28
1.3.1. Structure and Function 28
1.3.2. Signalling 31
1.3.3. Trafficking 33

1.4. Approaches Used to Assess the Membrane Dynamics and Organisation of Membrane Proteins 34
1.4.1. Confocal Microscopy 34
1.4.2. Fluorescence Correlation Spectroscopy 35
1.4.3. Fluorescence Recovery After Photobleaching (FRAP) 36
1.4.4. Raster Image Correlation Spectroscopy (RICS) 37
1.4.5. Bioluminescence Resonance Energy Transfer (BRET) 38

1.5 Thesis Aims 40

Chapter 2: General Materials and Methods 41

2.1 Cell Culture 42
2.1.1. Passaging Cells 42
2.1.2. Freezing and Thawing Cells 43
2.1.3. Generation of Mixed Population Stable Cell Lines 43
2.1.4. Poly D-Lysine Coating 44
2.1.5. Transient Transfection 44
2.1.6. Cell Seeding 45

2.2 Functional Assays 46
2.2.1. Bystander Arrestin Recruitment Assay (K-Ras) 46

2.3 Confocal Microscopy 48
2.3.1. Microscope Set-up 48
2.3.2. SNAP Labelling 48
2.3.3. Ligand Addition 49
2.3.4. Time-series, Single Focal Plate Imaging 49
2.3.5. Imaging Receptor Co-localisation with Early Endosome Marker 49
2.3.6. Imaging Receptor Co-localisation with LAMP-1, Lysosomes Marker 50

2.4 Fluorescence Spectroscopy 52
2.4.1. Microscope Set-up 52
2.4.2. SNAP Labelling 52
2.4.3. Ligand Addition 52
2.4.4. Fluorescence Correlation Spectroscopy (FCS) 53

2.4.5. Fluorescence Recovery After Photobleaching (FRAP) 57
2.4.6. Raster Image Correlation Spectroscopy (RICS) 58

2.5. Data Analysis 59
2.5.1. FCS Data Analysis 59
2.5.2. Photon Counting Histogram (PCH) Analysis 63
2.5.3. FRAP Data Analysis 65
2.5.4. RICS Data Analysis 67
2.5.5. Number and Brightness Analysis 69
2.5.6. Statistical Analysis of FCS, FRAP and RICS Data 71
2.5.7. Early Endosomes Marker and LAMP-1 Marker Co-localisation Analysis Using Segmentation and Quantification of Subcellular Shapes (Squassh) 72
2.5.8. Analysis of Average LAMP-1 and SNAP-tagged Receptor Intensity Per Cell 74
2.5.9. Functional Assays Analysis 75

Chapter 3: Plasma Membrane Organisation and Dynamics of CXCR4 ..76

3.1. Introduction 77

3.2. Methods 81
3.2.1. Cell Culture 81
3.2.2. Confocal Microscopy 81
3.2.3. Fluorescence Correlation Spectroscopy (FCS) 81
3.2.4. Fluorescence Recovery After Photobleaching (FRAP) 82

3.3. Results 84
3.3.1. Organisation of CXCR4 Under Basal and Ligand-stimulated Conditions 84
3.3.2. Plasma Membrane Organisation and Dynamics of CXCR4 – FCS Studies 86
3.3.3. Optimisation of FRAP Parameters 90
3.3.4. Plasma Membrane Organisation and Dynamics of CXCR4 – FRAP Studies 93
3.3.5. Relationship Between Bleaching Area Size and FRAP Diffusion Coefficient 96

3.4. Discussion 98

3.5 Conclusion 104

Chapter 4: Plasma Membrane Organisation and Dynamics of ACKR3 105

4.1 Introduction 106

4.2. Methods 108
4.2.1. Cell Culture 108
4.2.2. Confocal Imaging 108
4.2.3. Fluorescence Spectroscopy 109

4.3. Results 112
4.3.1. The Organisation of ACKR3 Upon Different SNAP Labelling Temperature 112
4.3.2. The Organisation of ACKR3 Under Basal and Stimulated Conditions 117
4.3.3. Plasma Membrane Organisation and Dynamics of ACKR3 – FCS Studies 118
4.3.4. Plasma Membrane Organisation and Dynamics of ACKR3 – FRAP Studies ... 121
4.3.5. Plasma Membrane Organisation and Dynamics of ACKR3 – RICS Studies 124

4.4. Discussion 129

4.5. Conclusion 137

Chapter 5: Effect of GRK Depletion on ACRK3 Receptor Localisation 138

5.1 Introduction 139

5.2 Methods **142**

5.3 Results **143**

5.3.1 Effect of GRK Depletion on ACKR3 Location and Function 143

5.3.2. Assessment of CXCR4 and ACKR3 Co-localisation with Early Endosome Markers 147

5.3.3. ACKR3 Co-localisation with Lysosomes Upon GRK Depletion 150

5.3.4. ACKR3 Distribution Upon GRK2/3 or GRK5/6 Depletion 152

5.4 Discussion **158**

5.5. Conclusion **165**

Chapter 6: General Discussion ***166***

6.1. General Discussion: Membrane Organisation and Dynamics of CXCR4 and ACKR3 ..... **168**

6.2. General Discussion: GRK Involvement in ACKR3 Trafficking **173**

6.3. Outlook and Future Directions **175**

6.4. Key Conclusions **177**

Chapter 7: References ***178***

Chapter 1: General Introduction

1.1. G protein-coupled Receptors

1.1.1. Classification and Structure

G protein-coupled receptors (GPCRs) form one of the largest protein superfamilies in the genome with a wide range of functions. Based on the GRAFS classification, five main families can be identified within the GPCR superfamily, the glutamate, the rhodopsin, the adhesion, the fizzled/taste2 (TAS2) and the secretin family [1, 2]. The first 3D crystal structure of a GPCR to be solved was that of rhodopsin [3]. Later on, the structural determination of the β2-adrenergic receptor gave further insight into GPCR structure [4]. Recently, the landscape of GPCR research has been dramatically changed by advances in structural biology, especially through the use of cryo-electron microscopy (cryo-EM) [5, 6]. While it is known that different receptor families within GPCRs are highly variable, they all share certain common features.

All the structures of GPCRs solved so far show a seven α-helix polypeptide chain arranged in an anti-clockwise direction that crosses the plasma membrane and forms the receptor. These seven transmembrane (7TM) parts are connected by three extracellular loops (ECL1-3) and three intracellular loops (ICL1-3). The C-terminus of the receptor is localised in the cytoplasm and plays an important part in receptor signalling while a more variable N-terminus is located in the extracellular region and can have ligand-binding features and glycosylation sites [3, 7]. The glutamate receptor family, which includes Gamma-aminobutyric acid (GABA) and calcium sensing receptors, shows a long, two-lobed N-terminus, which forms a 'Venus fly trap' for their ligand binding. The secretin family has a shorter N-terminus than the glutamate receptor and contains Cys bridges within their binding site. The adhesion receptor family has a variable length of N-terminus which contains glycosylation sites and proline residues. Conversely, the frizzle/TAS2 receptor family presents a short N-terminus without a ligand-binding site. The largest family of GPCRs is the rhodopsin family, which is divided into four subgroups α, β, χ, δ and several clusters within the subgroup have a very short N-terminal region [1]. All five families of GPCRs contain one disulfide bridge in their

extracellular loop formed by cysteine residues located between TM1 and TM2 also between TM3 and TM4. Moreover, the different families also share other structural motifs, and their ratio of proline and glycine is also related [1, 8]. In the extracellular region of the receptor, the second extracellular loops are likely to function as binding pockets directly or be involved in ligand binding [9]. In some GPCRs that bind to hydrophobic ligands that bind within the 7TM core of the receptor, the extracellular loop 2 and N-terminus can cover and block the binding pocket by creating a β-hairpin conformation. In other receptors with a hydrophilic ligand, ECL2 is more likely to form helix or sheet structures, which can vary between subfamilies. In the transmembrane part of the receptor, TM3 is suggested to have a role in maintaining structural and folding stability. Together with TM1 and TM2, TM3 demonstrates major conformational changes after receptor activation. The intracellular region of the receptor connects them with their downstream signalling effectors and structurally differs between families. However, a short helix (H8) before the C terminus seems to be present in many GPCRs of the rhodopsin family [10]. Also, the rhodopsin family presents three shared characteristics; one in TM7, the NSxxNPxxY motif, the DRY motif at the junction of TM3 and IL2 and the WxP motif located in the TM6 (Figure 1.1). These motifs have a role in receptor activation; the DRY motif has a role in G protein coupling and conformation changes; the NPxxY motif can stabilise the active state of the receptor, and WxP provides help with conformational rearrangements [1, 11, 12].

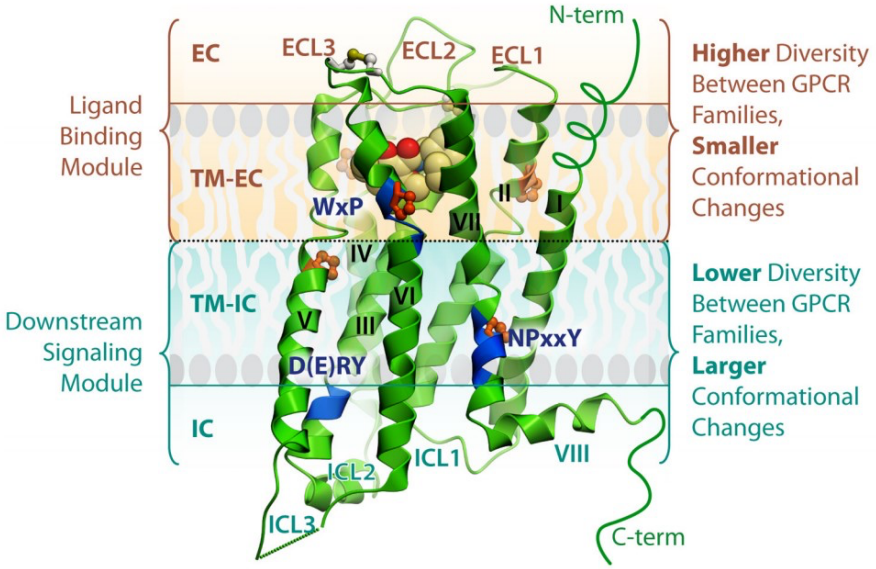

Figure 1.1: General structure of class A GPCRs. *Class A GPCRs consist of a 7TM structure connected via three extracellular loops (ECL1-3) and three intracellular loops (ICL1-3). The N-terminus is located on the extracellular side, while the C-terminal is intracellular [11].*

1.1.2. Canonical GPCR Signalling

GPCRs have complex downstream signalling. These receptors are canonically connected to and signal through heterotrimeric GTP-binding proteins (G proteins) and act as guanyl nucleotide exchange factors (GEFs) upon agonist activation. The G protein has three subunits α-, β- and γ, where the βγ is a constitutive dimer. Upon agonist activation, the receptor undergoes a conformational change that results in an outward movement of TM5/TM6, creating a cavity on the cytoplasmic side. This intracellular pocket functions as a docking site for the G protein [2, 13].

Upon receptor coupling, the G_{α}-subunit exchanges GDP for GTP. The GTP-liganded G_{α} -subunit depending on its subtype, may partially dissociate or reorganise with the βγ dimer and the receptor and can bind to effector proteins and induce various downstream signals. Besides this, the βγ dimer is also able to interact with intracellular effectors and induce downstream signalling [14, 15]. G_{α} -subunits are divided into four families: G_s, $G_{i/o/z}$, $G_{q/11}$, and $G_{12/13}$, which are the basis of the canonical G protein-dependent signalling. They have high structure homology, including a Ras-like GTPase domain and an α-helix

domain connected with two linkers. Furthermore, there are 5 G_{β} and 12 G_{γ} subunit isoforms [16, 17].

The classical classification of G proteins into G_s, $G_{i/o/z}$, $G_{q/11}$, and $G_{12/13}$ is based on the downstream effectors of the G_{α} -subunits (Figure 1.2). $G_{\alpha q/11}$ activates the β-isoform of phospholipase C (PLC), which results in cleavage of membrane phospholipid phosphatidylinositol 4,5-bisphosphate to yield 1,2-diacylglycerol (DAG) and inositol 1,4,5-trisphosphate (IP_3). The increased IP_3 and DAG lead to elevated intracellular Ca^{2+} and activation of protein kinase C (PKC), respectively. $G_{\alpha s}$ activation results in the activation of adenylyl cyclase, increasing cyclic AMP (cAMP) levels and activating cAMP-dependent protein kinase (PKA) through the binding of cAMP to its regulatory subunit. In contrast, $G_{\alpha i/o/z}$ inhibits adenylyl cyclase, therefore, reducing cAMP generation. Lastly, $G_{12/13}$ activate the monomeric GTPase RhoA and inhibit Rho kinase [18]. Finally, $G_{\beta\gamma}$ subunits also have an important role in GPCR signalling. Effectors of $G_{\beta\gamma}$ include ion channels and MAPK amongst others [19].

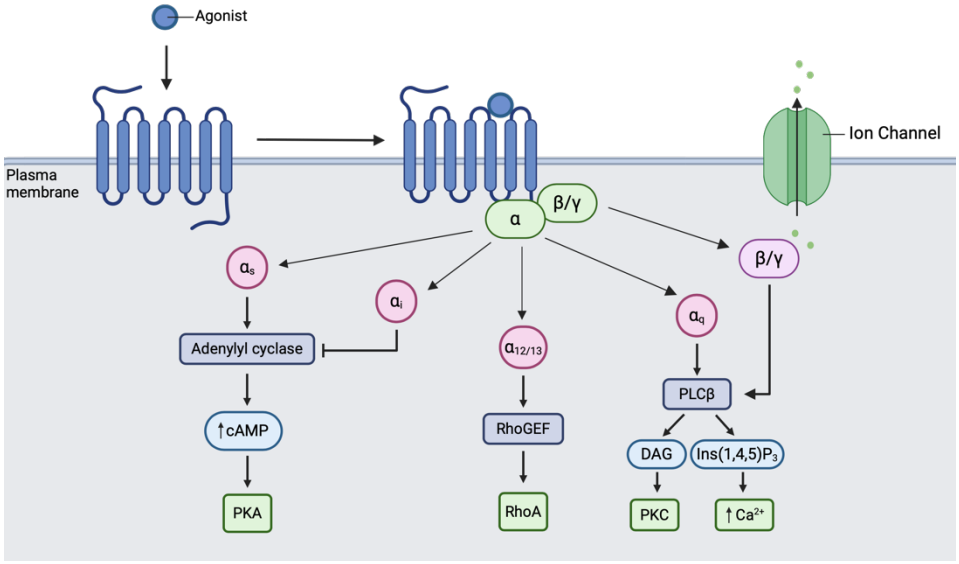

Figure 1.2: Canonical signalling pathways of GPCRs. *$G_{\alpha q}$ pathway causes IP_3 and DAG increase via PLCβ, which leads to elevated intracellular Ca^{2+} and PKC activation. $G_{\alpha s}$ activates adenylyl cyclase and leads to increases in cAMP levels and PKA activation. $G_{\alpha i}$ inhibits adenylyl cyclase, therefore, reducing cAMP levels. $G_{12/13}$ activates the monomeric GTPase RhoA. The figure was created with BioRender.com based on Ritter & Hall, 2009 [20].*

1.1.3. G Protein-Coupled Receptor Kinases (GRKs)

Aside from their canonical signalling through G-proteins, GPCRs can act and be regulated through alternative pathways. One such regulatory mechanism involves G protein-coupled receptor kinases (GRKs). GRKs consist of a unique N-terminus, a regulator of G protein signalling homology domain (RH), and a Serine/Threonine protein kinase domain (KD) [21]. GRKs bind to the cytoplasmic region of activated GPCR and phosphorylate the receptor at intracellular serine and threonine residues. This phosphorylation occurs at sites overlapping within the G protein interacting sites, thereby partially inhibiting the G protein coupling [22, 23]. A recent structural study also implicated the N-terminus of GRKs in the docking of activated GPCR and GRK activation [24].

There are three classes of GRKs; GRK 1 and 7 are membrane-localised due to prenylation at their C-terminus. The GRK2/3 isoforms are found in the cytosol and translocate to the membrane after binding to $G_{\beta\gamma}$ through their pleckstrin homology (PH) domain. The GRK 4/5/6 subfamily is associated with the plasma membrane via their interaction with membrane phospholipids and they lack both the PH domain and prenylated C-terminal [14, 20, 21].

GRK2/3 and GRK5/6 are widely expressed in mammalian tissues. However, GRK1 and GRK 7 expression is limited to the vertebrate rod and cone photoreceptors, and pinelocytes, while GRK4 is mainly expressed in the testis and proximal tubule cells in the kidney [21, 25, 26]. Due to their role in phosphorylating activated GPCRs, GRKs are important for the recruitment of β-arrestin to the phosphorylated receptor [23, 27].

1.1.4. β-arrestins

Another important participant in GPCR signalling pathways is arrestin. Four isoforms of arrestin are known, categorised into visual/sensory arrestins (arrestin1 and arrestin4) and non-visual arrestins (β-arrestin1 and β-arrestin2) [28, 29]. Arrestin is composed of two β-sandwich domains, an N- and C-domain, which are linked by a ‘central crest’ and a C-terminal tail. β-arrestins

are suggested to play a role in most non-visual GPCR signalling and regulation. They can bind to the activated, phosphorylated GPCR (by GRKs and other intracellular kinases such as PKC and PKA), leading to receptor desensitisation and internalisation. Upon binding, β-arrestin undergoes conformational change. Structural studies propose that β-arrestin has two main interaction sites with GPCRs: one involving the N-domain of arrestin binding to a phosphorylated region of the receptor and another involving the insertion of the arrestin finger loop region into the cytoplasmic site of the GPCR core. By binding to the GPCR core, arrestin can result in the termination of G protein-mediated signalling [30-32]. β-arrestins classically promote GPCR internalisation through their association with clathrin and adaptor protein-2 (AP2), and they are key components of the internalisation machinery [14]. However, it has recently been shown that G proteins and β-arrestins can form a megaplex with the receptor and induce distinct signalling [33]. Whether β-arrestin-mediated signalling is G protein independent is still a matter of debate [34, 35]. However, it has been shown that β-arrestins can mediate MAPK ERK 1/2 activation via Src-dependent pathway [33].

1.1.5. Receptor Trafficking

Receptor trafficking and compartmentalised signalling are increasingly acknowledged as contributors of the complex cellular responses of GPCRs, in particular for regulating signal amplitude and duration. As previously described, upon GPCR activation, GRKs can phosphorylate the receptor and induce the recruitment of β-arrestins. Through β-arrestin binding to the receptor and its association with clathrin and AP2, prolonged stimulation of receptors results in internalisation and clathrin-mediated endocytosis (CME) by the formation of clathrin-coated pits (Figure 1.3) [36, 37].

Based on their β-arrestin binding and internalisation, GPCRs have been classified into Class A and Class B groups. Class A receptors bind β-arrestin2 with higher affinity (compared to β-arrestin1), internalise in membrane vesicles and dissociate early from β-arrestin. In contrast, Class B receptors show similar affinity towards β-arrestin1 and β-arrestin2 and present endosomal

trafficking, forming stable complexes with β-arrestins. Another difference between the two groups is their ubiquitination [28, 38]. Ubiquitination involves the reversible attachment of ubiquitin molecules to a protein serving as a target signal for receptor degradation. By tagging the receptor, ubiquitination can play an important role in regulating receptor degradation, cell surface expression and different cellular responses [39, 40]. Class A is associated with transient β-arrestin interactions and limited ubiquitination, while Class B has stable β-arrestin interactions leading to ubiquitination [28, 38]. These distinct ubiquitination patterns between receptor classes contribute to their various trafficking and signalling pathways [40, 41].

Once internalised, GPCRs traffic through the endocytic network. The endosomal compartments can be classified into early and late endosomes based on their maturing and small GTPase Rab content. Rab5 is specific for early endosomes, while Rab7 is characteristic of late endosomes, and Rab4 or 11 is for recycling endosomes. From the early endosome, two paths are possible: degradation by a lysosomal pathway or recycling back to the plasma membrane either through the trans-golgi network or directly [33]. It has been shown that ubiquitination can also play a role in receptor trafficking as several GPCRs have a ubiquitin target lysine in their 3rd intracellular loop. This can be a critical motif for ligand-mediated internalisation and the determination of downstream trafficking pathways [33, 36, 37].

Increasingly, evidence points to GPCR localisation and its critical regulatory effect on downstream signalling and biological responses. Besides cell surface signalling, GPCRs are able to induce signals in different subcellular compartments, such as the endoplasmic reticulum, mitochondria and nucleus [42]. A study has also shown that the golgi/trans-golgi network includes a G protein pool and is able to stimulate AC and cAMP local signalling [43]. In addition, receptor ‘hot spots’ were discovered on the cell surface, indicating a further regulation of downstream signalling depending on the precise localisation within the plasma membrane. This spatiotemporal regulation might be the key to the different physiological effects of GPCRs and might play a role

in the development of pathophysiological conditions as well as avenues for therapy [42].

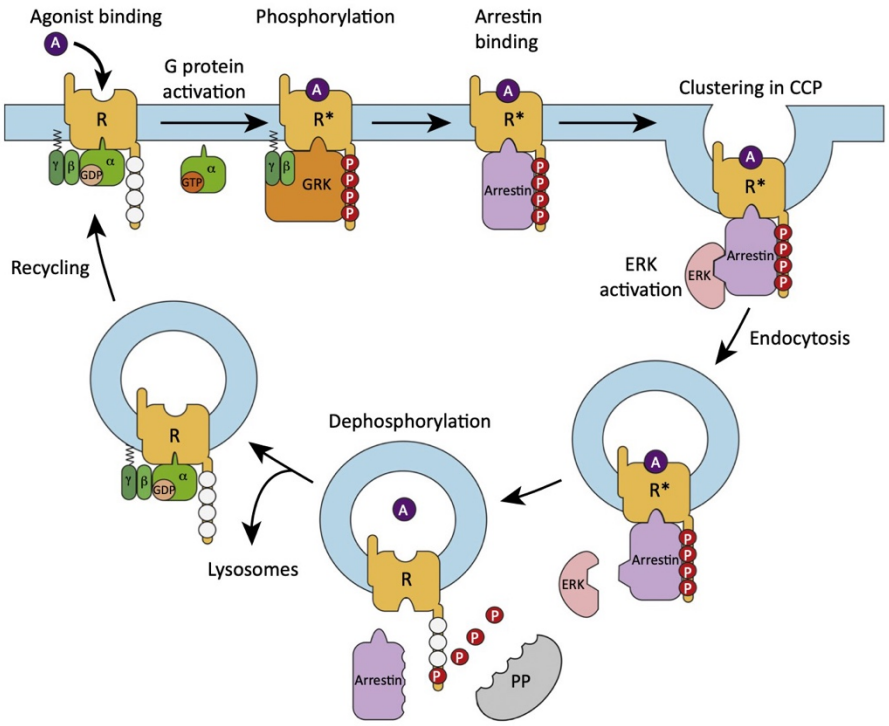

Figure 1.3: GPCR trafficking. *After agonist binding, GRKs phosphorylate the receptor and recruit β-arrestin which induces receptor internalisation. From the early endosome, two paths are possible, receptor degradation by a lysosomal pathway or recycling back to the membrane [44].*

1.2. Chemokines and Chemokine Receptors

1.2.1. Chemokines

Chemokines (chemoattractant cytokines) are diverse small peptides that contain around 67-127 amino acids and are well known for their role in leukocyte migration. Chemokines can be classified based on their function but also on their structure. One of the functional subfamilies distinguishes between the inflammatory chemokines, whose members regulate the recruitment of leukocytes and are expressed during inflammation, infection and tumours. In the case of infection, sentinel cells such as dendritic cells and macrophages detect pathogenic stimuli and induce a cascade response which results in the expression and production of inflammatory chemokines. These chemokines

can control the local inflammatory milieu and recruit additional T-cells and macrophages that act as a source of further chemokines. In contrast, the other chemokine subfamily, the homeostatic chemokines, are involved in the physiological immune response and play a role in leukocyte navigation during haematopoiesis. These chemokines are present in the lymphoid structure, and their cellular expression is vital for physiological conditions; however, they can also play a role in autoimmune diseases. Finally, some chemokines do not fit into these two functional groups and have a role in both immune defence and surveillance [45].

Structurally, chemokines show high sequence homology with a conserved C-terminal helix four cysteine (Cys) motif, forming two disulphide bridges and a flexible N-terminal region essential for receptor activation (Figure 1.4). We can classify chemokines into two major and two minor structural families based on the spacing between the first two Cys residues. The CXC family (α subclass) has a single amino acid spacer in between the cysteine residues in contrast to the other major family, CC (β subclass), where the cysteines are in adjacent positions. In the CX3CL minor family, N-terminal Cys residues are separated by three amino acids, while the XCL family lacks two cysteines towards the N-terminal side [46, 47].

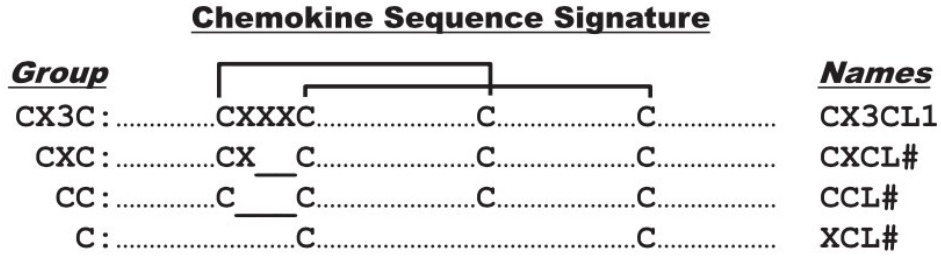

Figure 1.4: Chemokine structural characterisation: *Chemokines can be classified into two major and two minor families based on their conserved Cys residue signature [48].*

The N terminal region of the chemokines is a key region in receptor binding. The ELR motif seems essential for receptor binding, and its mutation results in decreased affinity and switches from agonist to antagonist nature [48, 49]. Upon binding to GPCR chemokine receptors (see below), chemokines can

activate several downstream signalling pathways involving cyclic AMP (cAMP), calcium mobilisation and kinase phosphorylation cascades. Moreover, besides chemokine receptor binding, chemokines can also bind to glycosaminoglycans (GAGs), which immobilise them at the cell surface, thereby controlling local chemokine activity and concentration [46, 50]. Previous studies indicate that CXC and CC chemokines can also form homo- and heterodimers, regulating their activation and function [48]. Chemokines are degraded by proteases released by activated leukocytes. Enzyme families like the matrix metalloprotease (MMP) family, which has a role in the inhibition of cell migration and degradation of the extracellular matrix, also fulfil a function in chemokine degradation, more precisely MCPs can cleave CXCL12 and inactivate it [49].

1.2.2. Chemokine Receptors

Chemokines bind to and activate chemokine receptors. Chemokine receptors are part of the rhodopsin or Class A GPCR family, and within that, they belong to the c subgroup [1]. They can be classified into four subfamilies; CCR, CXCR, XCR and CX_3CR, based on the subfamily of chemokine ligands that they bind. A fifth group is the atypical chemokine receptor (ACKR) sub-family, which differs from the other families in both structural and signalling properties.

So far, the structure of five members of the chemokine receptor family have been determined and based on that, shared structural characteristics can be deduced. The most conserved structure throughout the chemokine receptor families is the DRYLAIV motif at the intracellular end of TM3; however, the atypical family lacks this characteristic [48]. Besides the general disulphide bridge presented in most GPCRs, in the chemokine receptors, an additional bridge is located between the N terminus and ECL3. Another unique characteristic within the chemokine receptor family, and relevant for ligand binding, is an unusual helical kink caused by a longer N terminus that repositions it towards the TM7 domain. In addition to this feature, the S/TxP motif at the top of TM2 seems to have an essential role in ligand binding [49].

As mentioned above, atypical chemokine receptors lack the DRYLAIV motif. This has been proposed to explain their lack of coupling and signalling via G proteins. Currently, four members of the ACKR family have been characterised, ACKR1, ACKR2, ACKR3 and ACKR4. Previous studies showed that they could bind to specific CC and CXC chemokines and have a functional and scavenging role whereby they bind chemokines and internalise them, effectively depleting chemokine concentration in the extracellular milieu [51].

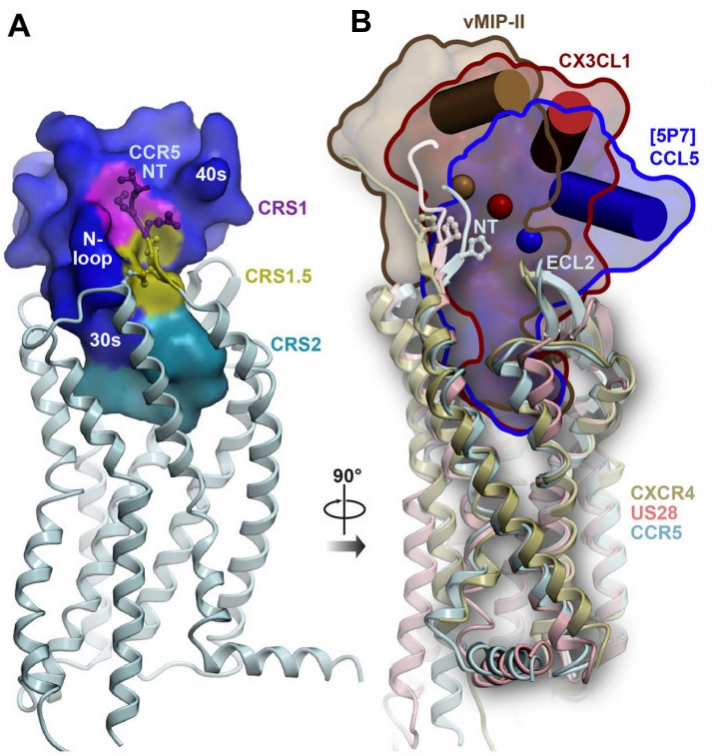

Figure 1.5: Chemokine receptor structure. A. *The CCR5 receptor complex and the binding sites observed during receptor-chemokine binding. The chemokine recognition sites are observed and highlighted as CRS1, CRS1.5 and CRS2 on the CCR5-CCL5 complex. B. The position of the chemokine core relative to the TM domain of three ligand-bound receptors: CCR5, US28 and CXCR4 [52].*

The interaction of chemokines with their receptor is described by the two-site, two-step binding model, which involves two recognition sites (Figure 1.5). The chemokine recognition site 1 (CRS1) can be found in the extracellular surface of the receptor around the N-terminus, and it binds to the core of the

chemokines. It can create the adequate conformation for the N terminus of the chemokine to interact with the orthosteric binding site in the 7TM domain of the receptor. The orthosteric binding site can be divided into a minor and a major subpocket, where the ligand can bind to both or just one subpocket. This change due to CRS1 leads to the formation of the chemokine recognition site 2 (CRS2) within the 7TM, which seems to be a chemokine-specific site and leads to receptor activation [47, 52]. Some studies have proposed an additional third site, CRS1.5, found in between CRS1 and 2 which might establish a particular order for the chemokine-receptor interaction [49]. This suggested three-step model involves a nonspecific binding with CRS1, then a specific binding through CRS2, followed by a conformational change as a third step resulting in the receptor activation and downstream signalling [53]. An additional intracellular allosteric binding pocket (distinct from where the endogenous chemokines bind) was discovered for small ligands and partially overlaps with the G protein and β-arrestin binding sites [54].

Chemokine receptors are typically coupled to the G_i heterotrimeric G proteins, except atypical chemokine receptors, which do not couple to G proteins and only elicit β-arrestin recruitment and chemokine scavenging. The activated G_i protein reduces cAMP levels via AC inhibition and also stimulates phospholipase-Cβ which triggers phosphoinositide 3-kinase (PtdIns3-Ks) and c-Src family tyrosine kinase activation. The PtdIns3-Ks activation can induce migration of immune cells such as macrophages and neutrophils. As with most GPCRs, chemokine receptors are phosphorylated upon activation by their ligands and internalise. After internalisation, the receptor can either degrade or recycle to the plasma surface. This receptor internalisation process can regulate the chemokine gradient and redistribution [45, 48].

The ligand-receptor pairs are not typically a one-on-one type relationship as most chemokines can bind to several chemokine receptors, and most chemokine receptors bind more than a single type of chemokine (Figure 1.6) [46].

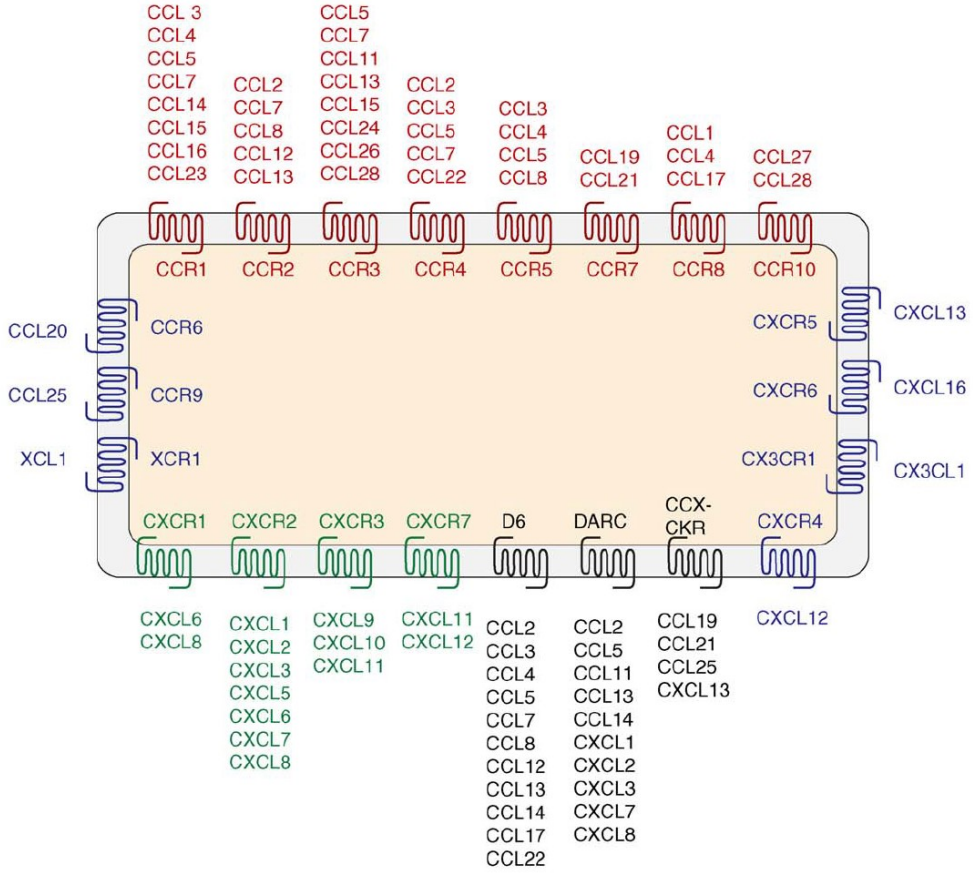

Figure 1.6: Chemokine receptors and their ligand. *Chemokine can bind to several chemokine receptors and receptors are also able to bind multiple chemokines. This figure refers to ACKR3 as CXCR7 [55].*

1.2.3. Physiological Functions of Chemokine and Chemokine Receptors

The most acknowledged role of chemokines is an immune regulatory function, including controlling immune function and regulating inflammatory processes [46]. As part of their immune function, they control leukocyte recruitment. The underlying mechanism starts with leukocytes rolling on the endothelial surface. Chemokine binding and activation of chemokine receptors expressed in leukocytes triggers a firmer adhesion through integrins binding to endothelial adhesion molecules, Vascular cell adhesion protein-1 (VCAM-1) and intracellular cell adhesion protein-1 (ICAM-1). Depending on the chemokine gradient, this trans-endothelial migration of leukocytes can either stay localised or induce additional inflammatory responses. As previously mentioned, there are two main functional classes of chemokines, having a different role in immune responses. The inflammatory chemokines, like CXCL12 and CCR6,

act in the migration of lymphocytes and antigen-presenting cells (APC). In contrast, homeostatic chemokines such as CCL17 affect T cell differentiation and act in a more monogamous (one chemokine to one receptor) binding way. Chemokines also induce the generation of oxygen radicals and upregulation of adhesion molecules and modify cell activation [56].

Based on their control of the migration and activation of leukocytes, chemokines represent an essential part of the immune defence and the promotion of inflammation. However, upon overexpression, chronic inflammation or autoimmune disease can be developed. Also, several studies have described the role of chemokines and their receptors in cancer and herpesvirus-associated inflammatory disease [57]. As inflammatory processes are a significant element of tumour development, chemokines can act as tumorogenic chemo-attractants. Tumour site expression of chemokines can modify the activation and phenotype of leukocytes and promote tumour angiogenesis and growth. Several chemokine axes, most notably the CXCL12/CXCR4, stimulate migration in breast cancer by MAPK/ERK pathway. Via these actions, antagonists of chemokine receptors could be a promising target in cancer therapy [58].

1.3. CXCR4 and ACKR3

1.3.1. Structure and Function

CXCL12, also known as stromal cell-derived factor-1 (SDF-1), is a shared chemokine ligand for CXCR4 and ACKR3 receptors. CXCL12 has six splice variants in human CXCL12α-θ, which differ in their amino acid number (Figure 1.7). The first eight amino acids of the CXCL12 N-terminal structure are relevant for activation, especially the terminal Lys and Pro. The receptor-binding motif of CXCL12 contains RFFESH sequences, and its binding is proposed to follow the two sites, two-step model detailed in the chemokines section above. In adult tissues, the variant CXCL12α and β are the most abundant and well-studied. In physiological conditions, CXCL12 is a homeostatic chemokine. However, CXCL12 has been shown to be

upregulated in hypoxia via hypoxia-inducible factor-1 (HIF-1) and promotes angiogenesis in tumours by activating the CXCR4 and ACKR3 receptors [59].

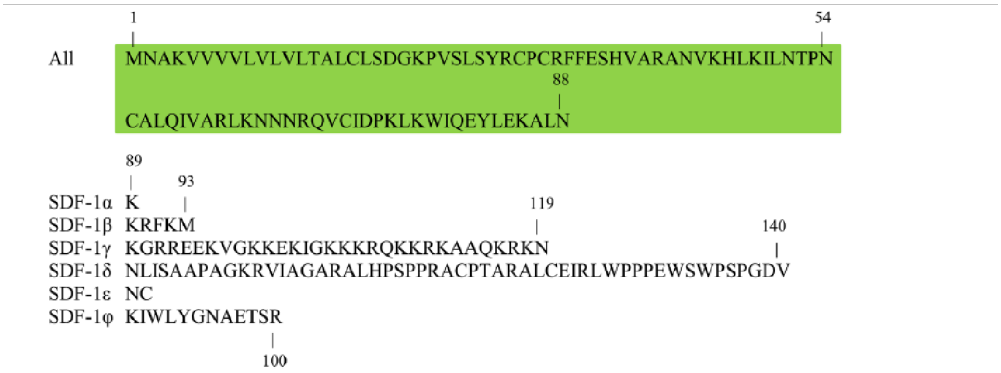

Figure 1.7: Sequences of the different CXCL12 (SDF-1) isoforms. *The six isoforms differ in their amino acid length [60].*

CXCR4 belongs to the classical chemokine receptor group, and CXCL12 is the only chemokine it binds to. CXCR4 structure was analysed upon co-crystallization with IT1t, a small ligand antagonist (Figure 1.8). Similar to other GPCR structures, it has a 7TM α-helix and three extracellular and intracellular loops. It presents a homology with other chemokine receptors detailed in the Chemokine receptor section (1.2.2 Chemokine receptor). The two disulphide bridges in the ECLs are essential for CXCL12 binding by forming a binding pocket divided into minor and major pockets. The C terminal end of CXCR4 does not show helix 8, and upon chemokine binding, the N-terminal pocket shifts outwards of the transmembrane helix. Structural studies also presented that CXCR4 tends to form receptor dimers which might functionally differ from monomers [61, 62].

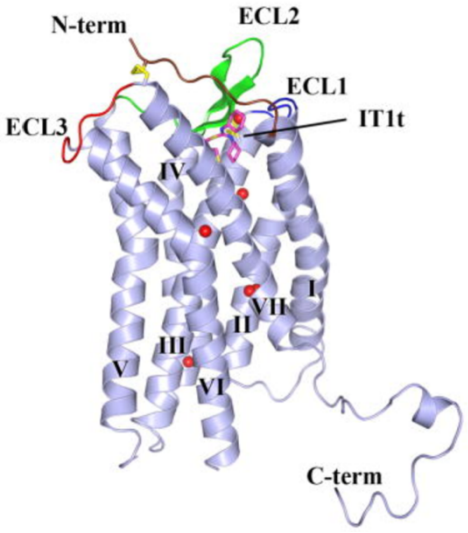

Figure 1.8: CXCR4 receptor structure. *Crystal structure of CXCR4 bound to small antagonist molecule IT1t. In the structure, the receptor is coloured in blue, the N-terminus extracellular loops ECL1, ECL2 and ECL3 are coloured brown, green and red and the conserved water molecules are marked as red dots [61].*

CXCR4 has several important physiological functions such as a role in hematopoiesis, vascularisation and cell migration. In pathophysiology, CXCR4 was found to act as a co-receptor for HIV virus entry and is associated with different types of cancer. CXCR4 can also promote metastasis, angiogenesis and tumour growth. Additionally, mutations of CXCR4 are connected to the immunodeficiency disease causing warts, hypogammaglobulinemia, infection and myelokathexis (WHIM syndrome) [63, 64].

ACKR3, previously known as CXCR7, binds CXCL12 with ten-fold higher affinity than CXCR4 and also has another chemokine ligand, CXCL11 (which also binds to CXCR3) [64]. The ACKR3 sequence lacks the typical DRYLAIV motif which is important for G protein coupling and signalling. Instead of the classical motif, ACKR3 has a DRYLSIT sequence, and studies have shown that it does not interact with G proteins [51, 65]. The ACKR3 structure has been recently determined (Figure 1.9), showing some typical characteristics of class A GPCR activation, such as the outward shift of helix 6. Next to this, some unique aspects were identified, including the unconventional orientation of CXCL12, a short helix in intracellular loop 3, and the absence of the kink at

the N-termini. These atypical features might contribute to the absence of G protein signalling of the ACKR3 receptor [66-68].

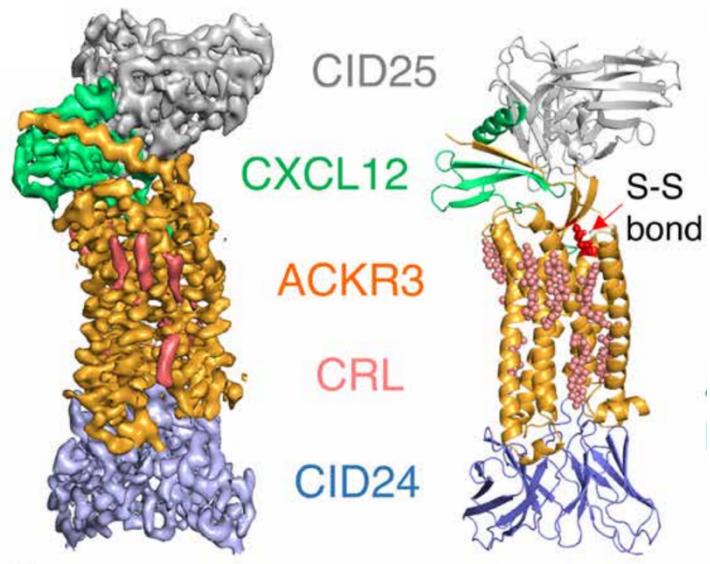

Figure 1.9: ACKR3 receptor structure. *Cryo-EM structure of ACKR complex with CID25-CXCL12 and CID24 [67].*

ACKR3 can function as a 'scavenging' receptor, modulating CXCL12 availability, and through that, it can modulate chemokine gradient and immune response [64, 69]. Like CXCR4, ACKR3 also promotes metastasis and tumour growth in several cancer types such as breast and prostate cancer and cardiovascular diseases [51, 59, 65]. A previous study also showed ACKR3 is able to scavenge opioid ligands, suggesting a broader function of ACKR3 beyond chemokines [70].

1.3.2. Signalling

CXCR4 receptor signalling has been extensively studied (Figure 1.10) [60]. CXCR4 is canonically coupled to G_i-proteins. This pertussis toxin-sensitive pathway reduces cAMP levels via AC inhibition and stimulates PI3K/AKT-dependent cascade and PKC. In cancer cells, CXCR4 also showed $G_{\alpha 12/13}$-coupling and a $G_{\alpha q}$ pathway was also presented in immune cells. Besides its G protein-dependent signalling, CXCR4 can be phosphorylated by GRKs and recruit β-arrestins and signal through p38 MAPK. In addition, CXCR4 can recruit Janus kinase (JAK) 2/3 and induce calcium mobilisation and

chemotaxis via signal transducer and activation of transcription (STAT) molecules [64, 71].

In contrast to CXCR4, upon CXCL12 or CXCL11 binding, ACKR3 does not signal through G proteins (Figure 1.10). Previously, ACKR3 was classified as a “decoy” receptor for CXCR4 as it scavenges CXCL12 and prevents CXCR4 activation, desensitisation and degradation. However, it has been suggested that upon agonist binding, ACKR3 internalises and induces β-arrestin-mediated downstream signalling via ERK1/2 activation [72], although these results are still being debated. After agonist activation, ACKR3 is phosphorylated by GRKs, which is essential for β-arrestin1 or β-arrestin2 recruitment [73]. It has been proposed that β-arrestin triggers downstream signalling and ERK1/2 activation via MAPK or AKT cascade as well as inducing cell migration and tumorigenesis through c-Src activation [59, 64, 73].

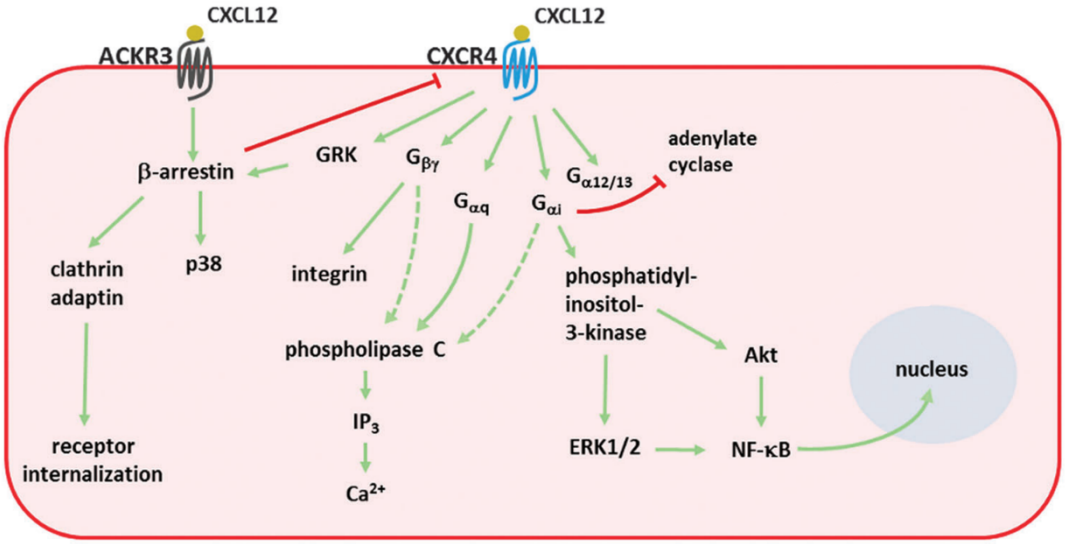

Figure 1.10: CXCR4 and ACKR3 receptor downstream signalling. *CXCR4 canonically signals through $G_{\alpha i}$-protein dependent pathway which inhibits AC and stimulates the PLC and ERK1/2 pathway. The receptor is also able to signal through $G_{\alpha q}$ and $G_{\alpha 12/13}$ pathways and can recruit JAK2/3 and induce calcium mobilisation and chemotaxis. In contrast, ACKR3 does not signal through a G protein-mediated way. Upon activation, ACKR3 recruit β-arrestin, internalise and activate β-arrestin mediated downstream signalling [59].*

1.3.3. Trafficking

Desensitisation of CXCR4 and regulation of its signal duration can be controlled by receptor trafficking. Phosphorylation of the CXCR4 receptor via GRKs follows receptor activation by CXCL12, leading to β-arrestin recruitment and G protein uncoupling. This type of desensitisation of the CXCR4 receptor is called homologous desensitization and is induced by GRK2/3/6 upon agonist binding. The other possible mechanism is heterologous receptor desensitisation via PKC, which does not require agonist binding as PKC can be activated through other mechanisms. The C-tail phosphorylation of the CXCR4 receptor, namely two serine residues, also promotes ubiquitination and leads to well-regulated receptor trafficking towards lysosomal receptor degradation [74].

The ACKR3 receptor tends to internalise after activation by CXCL12 or CXCL11. Zarca et al. also showed that upon CXCL12 stimulation, ACKR3 receptor internalised quickly upon recruitment of GRK 2/3/5 and β-arrestin1 and β-arrestin2 (Figure 1.11) [73]. The rapid internalisation of the early endosomes was followed by ACKR3 recycling back to the plasma membrane. The C-terminal SETEYS cluster of the receptor seemed to be essential for both β-arrestin1 and 2 interaction and β-arrestin mediated receptor internalisation [73]. Another study suggested that deubiquitination of ACKR3 has a crucial role in ACKR3 internalisation and endosomal trafficking. Data showed that in contrast to CXCR4, the ACKR3 receptor is basally ubiquitinated in the plasma membrane. Upon CXCL12-mediated receptor activation, β-arrestin recruitment and interaction with the de-ubiquitinating enzyme (DUB) resulted in receptor deubiquitination and internalisation. During the recycling towards the plasma membrane, it was suggested that the receptor uncoupling from the β-arrestin allows the receptor to get ubiquitinated again and remain on the cell surface [72].

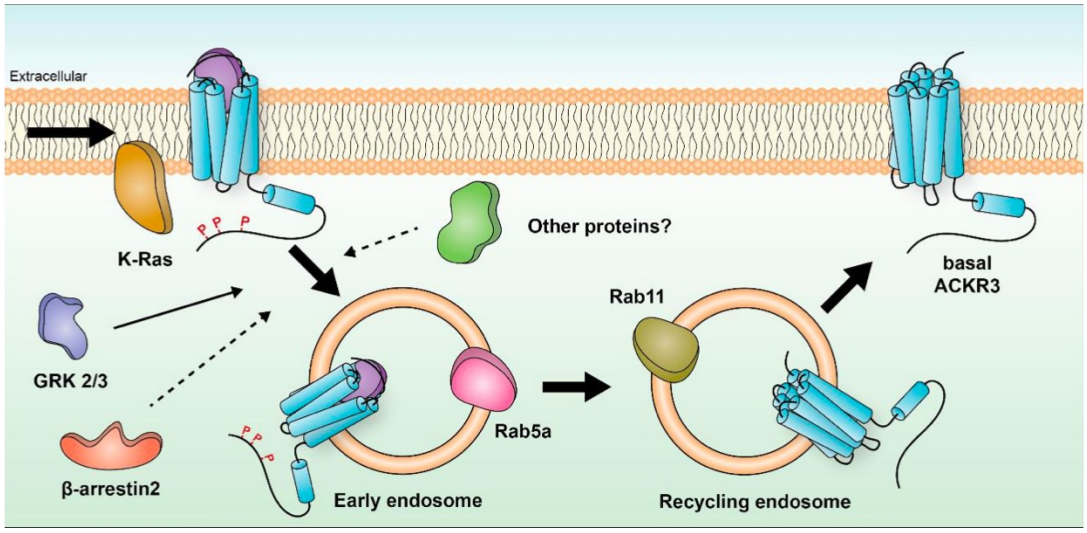

Figure 1.11: ACKR3 receptor internalisation and trafficking. *After receptor activation, the ACKR3 receptor internalises to the early endosome upon phosphorylation and β-arrestin binding. Afterwards, the receptor recycles back to the plasma surface via recycling endosomes [73].*

1.4. Approaches Used to Assess the Membrane Dynamics and Organisation of Membrane Proteins

1.4.1. Confocal Microscopy

Confocal microscopy is extensively used for determining the localisation of fluorescent species and to monitor live cell dynamics. The confocal microscope uses a laser as the light source and focuses illumination and detection optics on the same spot during scanning. The pinhole rejects any out-of-focus light and allows us to image one focal plane at a time while the scanning provides us with the x-y resolution. Properties of confocal microscopy such as the numerical aperture of the lenses and filter for wavelength selection, provide a high resolution (~250 nm) and enable detection and capture of small features. Confocal microscopy supports multi-colour imaging and allows for the adjustment of the pinhole size to offer different thicknesses of optical sections. In addition, confocal microscopy also accommodates both live and fixed cell samples [75].

1.4.2. Fluorescence Correlation Spectroscopy

As previously mentioned, fluorescence-based technologies such as confocal microscopy can provide information about the co-localisation of different proteins. However, these methods lack the ability to quantify the binding properties of ligand-receptor complexes within membrane microdomains and give quantitative information about receptor concentration and organisation.
Fluorescence Correlation Spectroscopy (FCS) can determine the receptor number and properties of its movement which provides information about its organisation (Figure 1.12). FCS is based on confocal optics and due to its laser, high numerical aperture objective and confocal pinhole, it can create a small detection volume, approximately 0.25 fl. The diffusion and movement of fluorescent molecules within this Gaussian-shaped detection volume cause changes in the fluorescence intensity of the emitted photons. The autocorrelation analysis of this time-dependent fluorescent intensity fluctuation provides information about the diffusion coefficient and concentration of the fluorescent species. The autocorrelation traces can be fitted to a 2D or 3D model, providing information about the dwell time and the number of molecules within the detection volume. Dwell time is related to molecular mass; small fluorescent molecules show a fast diffusion, while larger fluorescent species, present a slower movement with a reduced diffusion coefficient. Based on these changes in the diffusion speed, FCS allows the detection of receptor interactions and ligand-induced changes in organisation as they alter the diffusion properties of the receptor alone. Through these data, FCS can provide quantitative information about the diffusion, density and concentration of the receptor within a membrane microdomain [76-78]. FCS is a powerful technique for studying the dynamics of receptors, offering single-molecule sensitivity and the ability to measure a broad diffusion rate. This makes it ideal for investigating membrane-bound receptor organisation within a small defined region [77, 79]. FCS has previously been used to successfully study ligand-receptor complexes and the organisation of different GPCRs [80, 81], hence an ideal technique to assess CXCR4 and ACKR3 receptor dynamics at the membrane.

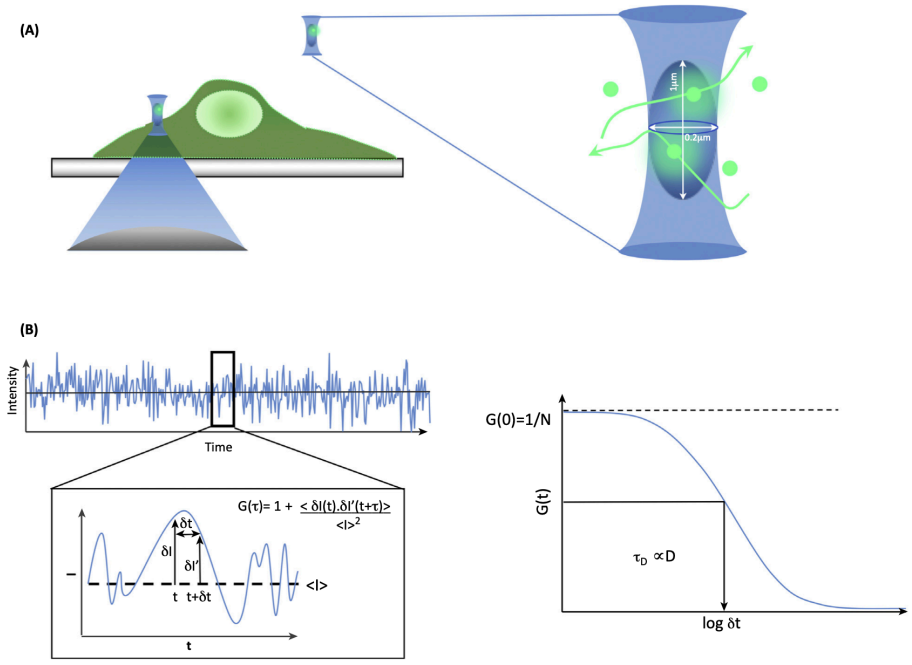

Figure 1.12: Principles of FCS: *Using a high aperture and focusing the laser and pinhole can create a Gaussian-shaped detection volume (**A**). Fluorescent molecules passing through this volume are exited and emitted photons creating fluctuation in the fluorescent intensity. Autocorrelation analysis of this fluctuation can provide information on average dwell time (τ_D) and the number of molecules (N). From these data, the diffusion coefficient (D) can be calculated (**B**) [77].*

1.4.3. Fluorescence Recovery After Photobleaching (FRAP)

FRAP is an alternate image-based technique for assessing the diffusion and movement of fluorescent species within a cell. It can be complementary to FCS as it elucidates additional information. In contrast to FCS, FRAP provides information concerning the mobility status of the fluorescently labelled species by measuring the rate of fluorescence recovery at a precise area which has been previously photobleached. During FRAP a small defined area of the cell is irreversibly photobleached using high laser power. As time elapses, non-bleached fluorescent molecules from the surrounding membrane will diffuse to the bleached area which leads to a recovery of fluorescence. This recovery is recorded over time and plotted on a kinetics graph with fluorescence change over time, providing information about mobile and immobile fractions (Figure 1.13). From this kinetics plot, the half-life of recovery can be determined, and

the diffusion coefficient can be calculated. Changes in the mobile:immobile ratio can help interpret temporal and spatial changes in cell microdomains and via FRAP we can also obtain information about the immobile fraction of fluorescent molecules (which are not detected in FCS) [82, 83].

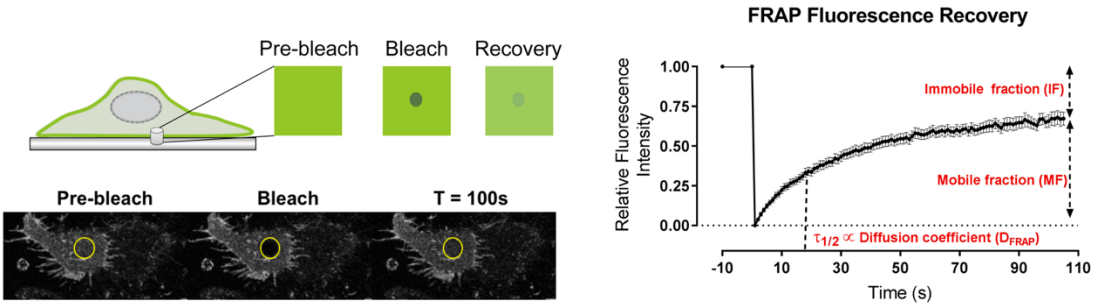

***Figure 1.13: Principles of FRAP**: During FRAP a small defined area of the cells is irreversibly photobleached. The recovery of the bleached area is recorded over time and plotted in a kinetics graph providing information about the mobile and immobile fractions and recovery half life time. From these data, the diffusion coefficient can be calculated [84].*

1.4.4. Raster Image Correlation Spectroscopy (RICS)

Raster Image Correlation Spectroscopy (RICS) is a fluorescence- and confocal-based advanced spectroscopy technique that can provide information about molecular dynamics over a larger scale through raster scanning. While FCS can only provide information over a small region, RICS can assess spatial-temporal information over a larger cell area with a high spatial resolution via scanning across and measuring the fluorescence intensity of one pixel per time and correlating fluctuations in pixel intensity between different locations and times (Figure 1.14). The raster scanning means that the fluorescence intensity data is collected in a specific order row by row from the top left pixel to create a RICS image. As each pixel intensity is measured in different time, analysis of RICS can also provide temporal information from the generated image. Following the application of a 2D diffusion model, concentration and the diffusion coefficient of fluorescent species can be obtained within a dynamic range of microseconds to milliseconds [85-87].

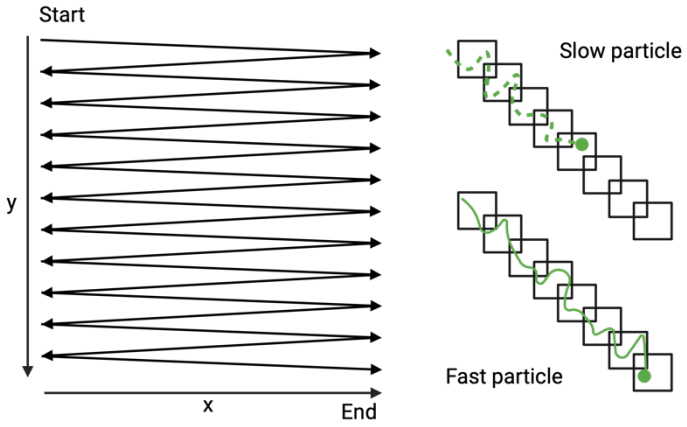

Figure 1.14: Principles of RICS*: RICS applies laser scanning to perform a raster scan across the image (x-axis) and in y-axis lines, capturing fluorescent intensity information pixel by pixel. During the beam movement, the fluorescent molecules may shift between pixels, depending on their diffusion speed. Analysing RICS, correlation curves can reveal information about the diffusion coefficient and concentration of fluorescent particles.*

1.4.5. Bioluminescence Resonance Energy Transfer (BRET)

BRET technology is based on non-radiative energy transfer between a donor enzyme and a fluorescence acceptor molecule. The donor enzyme is a luciferase such as nanoluciferase (NanoLuc) from deep sea shrimp which, upon degradation of its substrate, furimazine, emits bioluminescence that excites the fluorescent acceptor (such as yellow fluorescent protein, YFP) when in close proximity (<10 nm). In case of changes in the distance between the donor and the acceptor, the BRET ratio will be altered (Figure 1.15).

BRET approaches have become a useful tool in GPCR studies. Previous studies have extensively used this technique to assess receptor-protein interactions, fluorescent ligand binding to the receptor, changes in conformation and location of GPCRs and determination of receptor signalling [88-91]. Two different approaches have been developed to measure receptor-proteins interactions using BRET either expressing a receptor tagged with Nluc on the C-termini or using a membrane or specific subcellular marker as a BRET donor (and an untagged receptor) and observing BRET change upon translocation of the protein upon receptor activation [92, 93].

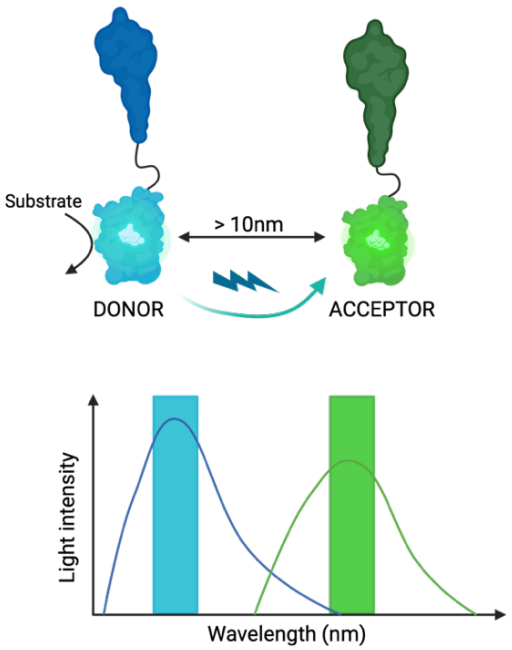

Figure 1.15: BRET Principle. *The BRET technique operates on the principle that the donor (Nluc) protein (following its oxidation by its substrate), transfers energy to the acceptor protein when they are in close proximity (<10 nm), resulting in a change in BRET ratio.*

1.5 Thesis Aims

As described in this chapter, the CXCR4 and ACKR3 receptors share the same ligand, CXCL12, and have been shown to play a role in various aspects of tumour development and metastasis. While CXCR4 signalling and regulation have been extensively studied, and some of the "unusual" characteristics of ACKR3 have been discovered, the CXCR4 and ACKR3 spatial and temporal dynamics at the cell membrane have not been assessed. This project, therefore, aims to further understand CXCR4 dynamics at the membrane and gain insight into ACKR3 receptor organisation and membrane dynamics through microscopy and spectroscopic approaches that provide high spatial and temporal resolution.

Chapter 3 aimed to assess the dynamics and organisation of CXCR4 at the plasma membrane by using confocal imaging, Fluorescence Correlation Spectroscopy (FCS), and Fluorescence Recovery After Photobleaching (FRAP). In addition, this chapter aimed to assess the effect of agonists (CXCL12) and antagonists (IT1t) on CXCR4 diffusion and mobility.

Chapter 4 aimed to assess the dynamics and organisation of ACKR3 at the plasma membrane via using confocal imaging, FCS, FRAP, and Raster Image Correlation (RICS) techniques. Moreover, it assessed the effect of CXCL12 on the receptor organisation.

Chapter 5 aimed to assess the effect of GRK deletion on ACKR3 receptor localisation with confocal microscopy and on receptor function with bioluminescence resonance energy transfer (BRET). Following our findings, co-localisation imaging with fluorescent subcellular markers was used to study and compare ACKR3 localisation in the absence of GRKs and determine the potential role of GRKs in ACKR3 subcellular localisation.

Chapter 2: General Materials and Methods

2.1 Cell Culture

Human embryonic kidney 293 (HEK293) Glosensor™ (HEKG) cells stably expressing the human SNAP-CXCR4 receptor were created previously, as described by Dekker et al. [94]. HEK 293 cells stably expressing the human SNAP-ACKR3 receptor were obtained from Kylie Pan at InterAx Biotech. The different combinations of CRISPR (clustered regularly interspaced palindromic repeat)/Cas-9 GRK-knockout HEK293 cell lines and HEK293 control cell line were received from Carsten Hoffmann's lab, created, and described by J Drube et al. [95]. The HEK293 ΔQGRK cell line was used to create the following mixed population stable cell lines: HEK293 ΔQGRK SNAP-ACKR3 and HEK293 ΔqGRK SNAP-CXCR4. The double GRK knock-out HEK293 ΔGRK2/3 and ΔGRK5/6 cell lines were used to create stable cell lines of HEK293 ΔGRK2/3 SNAP-ACKR3 and HEK293 ΔGRK5/6 SNAP-ACKR3. The generation of these cell lines is discussed later in this chapter.

2.1.1. Passaging Cells

Cells were cultured at 37 °C in a humidified atmosphere of 5% CO_2 in Dulbecco's modified Eagle's medium (DMEM, Sigma Aldrich, Gillingham, UK) with 10% Foetal Calf Serum (FBS, Sigma Aldrich, Gillingham, UK) and they were grown until they reached ≥70% confluency. The morphology and confluency of the cells were checked regularly and before passaging under an inverted microscope (Zeiss Primovert). During passaging, the medium was removed, and cells were washed with Dulbecco's phosphate-buffered saline (PBS/ Sigma Aldrich, Gillingham, UK). Following the wash, 1 ml of Trypsin (0.5 g/l trypsin, 0.2 g/l ethylenediamine tetraacetic acid (EDTA), ThermoFisher Scientific, UK) was added for 1-2 minutes to detach the cells from the flasks. The cells were washed off with 10 ml of DMEM/ 10% FBS and transferred to a Universal tube (30 ml). The cell suspension was centrifuged for 3 minutes at 1000 RPM. After removing the supernatant, the pellet was resuspended in 10 ml DMEM/10% FBS. The corresponding dilution of the cells was transferred into a T75 flask containing 15-20 ml media for maintenance purposes and was plated for experiments according to the protocol. To maintain stable selection

and receptor expression, HEK293 SNAP-ACKR3, ΔQGRK SNAP-ACKR3, ΔQ GRK CXCR4, ΔGRK2/3 ACKR3 and ΔGRK5/6 ACKR3 mixed population cell lines were cultured with 0.6 mg/ml G418 (Geneticin, Invitrogen), while HEK G SNAP-CXCR4 was cultured without the addition of G418.

2.1.2. Freezing and Thawing Cells

Cells were prepared for frozen storage using a freezing mix (90% FBS and 10% dimethyl sulfoxide (DMSO)). The freezing mix was filtered using a 0.2 μm syringe filter and a 20 ml syringe. After centrifugation, the cells were resuspended with 2-3 ml of freezing mix and transferred into cryovials in 1 ml aliquots (ThermoFisher Scientific, Loughborough, UK). The vials were placed in an isopropanol-insulated container providing slow freezing to -80 °C, then placed in the -80 °C freezer and transferred to storage in liquid nitrogen vapour within two months.

Cells from cryovials were thawed slowly at room temperature and were mixed with 10 ml of growth media. The cell suspension was then centrifuged for 3 minutes at 1000 RPM, followed by a pellet resuspension in 1 ml of media. Then, based on the size of the pellet, the cells were added into a T25 flask containing new media.

2.1.3. Generation of Mixed Population Stable Cell Lines

HEK293 ΔQGRK, HEK293 ΔGRK2/3 and HEK293 ΔGRK5/6 cells were grown in T25 flasks (Thermo Fisher Scientific, Loughborough, UK) and transfected when 60 - 70% confluent. For the transfection, 3 μg SNAP-ACKR3 or 3 μg SNAP-CXCR4 (in the case of ΔQGRK cells) DNA was used, mixed with 10 μl polyethylenimine (PEI) /condition in 150 mM sterile sodium chloride (NaCl) in a total volume of 250 μl. After vortexing, the mixture was incubated for 10 minutes in RT and then added to the cells. After 24 hours, 1 mg/ml of the antibiotic geneticin (G418) was added to the media for selection. The media (DMEM /10% FBS/G418) was changed every two to three days. After cell death plateaued, the antibiotic concentration was lowered to 0.6 mg/ml. After cells reached confluency, they were transferred into T75 and frozen as described above.

2.1.4. Poly D-Lysine Coating

White, clear bottom 96-well cell culture plates (Greiner Boi-One GmbH, Germany) were coated with 100 µl/well of 10 µg/ml poly-D-lysine (PDL) solution in PBS and the 8-well Labtek #1 borosilicate chambered coverglasses (Nunc Nalgene International, Thermo Fisher Scientific) were coated with 200 µl/well of the same. The plates were incubated for 30 minutes at room temperature and then washed with 100/200 µl/well PBS, respectively.

2.1.5. Transient Transfection

2.1.5.1. K-Ras Membrane Recruitment Assay

Cell lines were plated at different densities into 24-well cell culture plates, one well for each condition per cell line. The HEK293 ΔQGRK SNAP-ACKR3 and HEK293 ΔQGRK SNAP-CXCR4 cell lines were plated at 300,000 cells per well while HEK293 control, HEK SNAP-ACRK3 and HEKG SNAP-CXCR4 cell lines were plated 200,000 cells per well in 2ml DMEM/10% FBS media. The 24-well plates were incubated overnight at 37 °C in 5% CO_2. For transfection, FuGENE® HD Transfection Reagent (Promega, UK), a non-liposomal transfection reagent, was used. All cells were transfected with 0.6 µg K-Ras Venus, 0.05 µg β-arrestin Nanoluc (Nluc) and were divided into two transfection conditions either with 0.6 µg pcDNA3.1 or 0.6 µg GRK2 plasmid in 25 µl Opti-MEM™ - Reduced Serum Media (Thermo Fisher Scientific Inc., UK) per well. FuGENE HD was added to the DNA mixture in a 3:1 FuGENE HD: DNA ratio and incubated for 6 minutes in RT. Following that, 25 µl of the DNA mixture was added to each well, and the cells were incubated for 24 hours before seeding.

2.1.6. Cell Seeding

2.1.6.1. Cell Counting

The cells were counted using 10 µl of cell suspension loaded into the haemocytometer. The average cell count of at least 3 out of 4 central squares was taken. The calculated average multiplied by 10000 provided the number of cells per millilitre of media. Following the cell counting, the appropriate dilution was carried out based on the required seeding density for that cell line.

2.1.6.2. 8-well Plate Cell Seeding

For confocal imaging, FCS, FRAP and RICS experiments, PDL-coated Nunc 8-well chambered coverglasses were used. The cells were passaged as described previously (see 2.1.1. Passaging cells), and after the pellet resuspension, the appropriate dilution was carried out based on the required seeding density for that cell line (ranging from 15,000 to 80,000 cells per well) using 300 µl total volume per well. Cells were typically used for experiments 48 hours after seeding, except for the GRK knock-out cell lines, where the incubation time after seeding was 72 hours.

2.1.6.2. 96-well Plate Cell Seeding

The transfected plates were incubated overnight at 37 °C in 5% CO_2. In the case of replating cells from 10 ml dishes, the media was removed, and 2 ml trypsin was added to detach the cells. The cells were washed with 5 ml of DMEM/ 10% FBS and were transferred to a Universal tube and centrifuged for 3 minutes at 1000 RPM. After removing the supernatant, the pellet was resuspended with 1 ml DMEM/ 10% FBS media and then completed to 5 ml with additional media. The cells were seeded at 100 µl/well in a PDL-coated clear bottom white 96-well plate and incubated overnight at 37 °C in 5% CO_2.

For replating from 24-well plates, after the media was removed, 50 µl of trypsin was used per well to detach the cells. The cells were washed with 2 ml of DMEM/ 10% FBS and transferred into a Universal tube, and centrifuged for 3 minutes at 100 RPM. The supernatant was removed, and the pellet was re-

suspended with 600 µl DMEM/ 10% FBS media. The cells were seeded at 100 µl/well (6 wells per condition for each cell line) in a PDL-coated clear bottom white 96-well plate and incubated overnight at 37 °C in 5% CO_2.

2.2 Functional Assays

2.2.1. Bystander Arrestin Recruitment Assay (K-Ras)

Bioluminescence Resonance Energy Transfer (BRET) is a quantitative method employed to investigate receptor-protein interactions, elucidate localisation changes of GPCRs, and study receptor signalling. BRET relies on a non-radioactive energy transfer between a luciferase enzyme, which functions as the bioluminescent donor and a fluorophore serves as an acceptor. Upon addition of the luciferase substrate, furimazine, it emits bioluminescence that excites the fluorophore if it is located within 10 nm of the donor. Changes in the spatial proximity between the donor and the acceptor result in the alteration of the BRET signal [91, 92, 96].

In our study, the BRET assay assessed the receptor's ability to recruit β-arrestin-2. In this assay, the Venus-tagged K-ras functioned as a plasma membrane-bound acceptor and β-arrestin-2 Nluc is the donor. Upon ligand activation, the receptor recruits the β-arrestin-2 Nluc sensor, which results in an increased BRET ratio due to the close proximity of the acceptor K-ras Venus and donor β-arrestin-2 Nluc (Figure 2.1).

Following an overnight incubation after seeding, the media was replaced with Hank's Balanced Salt Solution (HBSS; contains 2mM sodium pyruvate, 145mM NaCl, 5mM KCl, 1mM $MgSO_4.7H_2O$, 10mM HEPES, 1.3mM $CaCl_2.H_2O$, 1.5mM $NaHCO_3$) with the addition of 5 mM glucose, and the cells were incubated for 30 minutes at 37 °C. After incubation, furimazine was added to the cells at a final concentration of 5 µM and incubated for 5 minutes at 37 °C in 5% CO_2. Furimazine is a substrate that is oxidised by nanoluciferase, creating light (luminescence), carbon dioxide and furimadine. Following ligand preparation, 10 nM (final concentration) CXCL12 (PeproTech, London, UK) was added and incubated for 5 minutes in the PHERAstar FS

Plate Reader (BMG Labtech) at 37 °C. After incubation, BRET was measured on the PHERAstar Plate Reader using the BRET1 filter set (535 ± 30 nm fluorescence, 475 ± 30 nm luminescence).

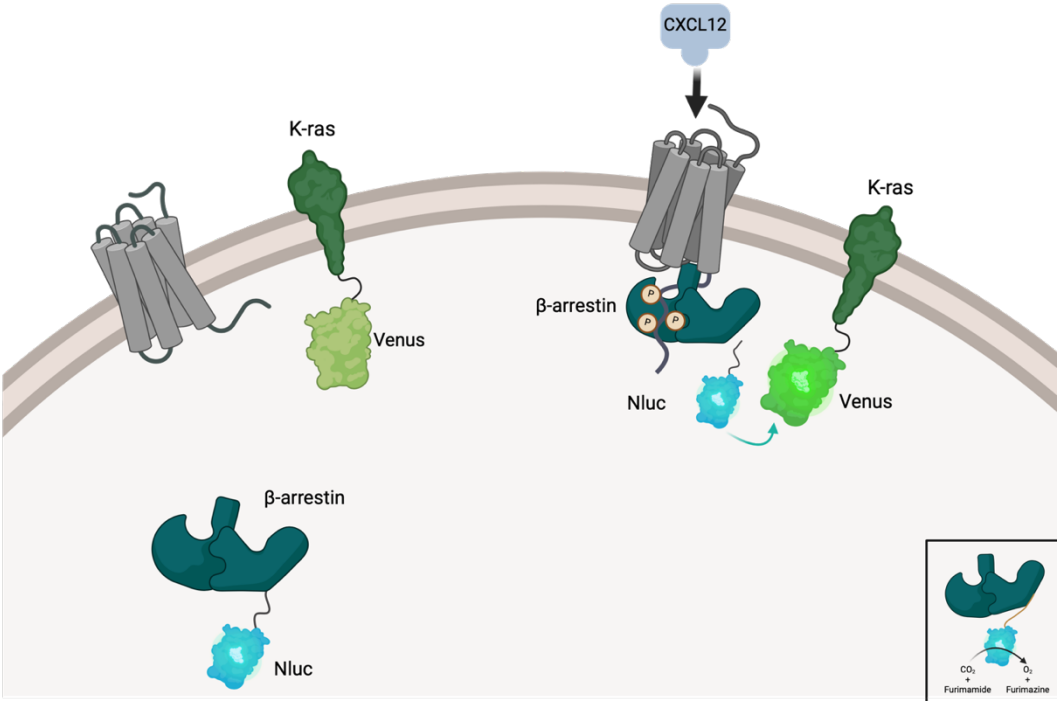

***Figure 2.1: K-ras membrane recruitment assay**. Upon ligand activation, the receptor recruits β-arrestin, resulting in an increased BRET signal due to close proximity and energy transfer between β-arrestin Nluc (donor) and K-Ras Venus (acceptor). The figure was created with BioRender.com.*

2.3 Confocal Microscopy

2.3.1. Microscope Set-up

All experiments were performed on a Zeiss Laser Scanning Microscope (LSM) 880 confocal microscope (Carl Zeiss, Germany) using a 40x c-Apochromat 1.2 NA water immersion objective. The precise laser, channel, laser scan speed, laser power and zoom were dependent on the type of measurement and are detailed for each experiment in the corresponding chapter/figure. All experiments, except imaging of lysosomal-associated membrane protein 1 (LAMP-1) lysosome marker, were carried out in live cells. After locating the cells and focusing, the gain of the channel was set up at the beginning of each individual experiment and kept consistent throughout the whole experiment for all cell lines on that day. Signal saturation was checked using the 'Range Indicator', and the gain was further adjusted prior to imaging to avoid oversaturated areas. The pinhole was kept in 1 Airy Unit (AU) for single equatorial images, and the image resolution was set to 1024x1024 pixels for all experiments.

2.3.2. SNAP Labelling

SNAP labelling was used to detect and image the SNAP-tagged receptor. The 20 kDa SNAP-tag is a modified DNA repair protein - an O^6-alkylguanine-DNA alkyltransferase. Upon specific reaction with benzylguanine (BG) derivatives, it forms a covalent bond, resulting in irreversible labelling with the BG-linked fluorescent SNAP dye [97]. For live cell imaging purposes, impermeant SNAP-dye, SNAP-Surface Alexa Flour 488 (New England BioLabs Ltd., UK) was used to label the membrane receptor in cells plated in 8-well chambers. First, the media was removed from the cells and cells were washed with 200 µl/well Hank's Balanced Salt Solution (HBSS) containing 5mM glucose. Then SNAP-Surface Alexa Flour 488 at 500 nM final concentration were added to the cells in HBSS/glucose buffer and incubated for 30 minutes at 37 °C. After incubation, the cells were washed with 200 µl/well HBSS/glucose three times with 5,5- and 20-minute incubation time between washes.

2.3.3. Ligand Addition

For ligand-induced observation, the cells in specific wells were treated with either CXCR4 and ACKR3 agonist, CXCL12 (recombinant Human SDF-1α, PeproTech, Inc., UK), CXCR4 antagonist IT1t (Tocris Bioscience, UK) or ACKR3 inverse agonist VUF16840 (received from VU Amsterdam, Netherlands). After the final washing steps of SNAP labelling described in 2.3.2 10 µl/well It1T was added to the cells at a final concentration of 1 µM and incubated for 30 minutes at 37 °C. To study the effect of CXCL12, 10 µl/well of CXCL12 at a final concentration of 10 nM was added in 190 µl HBSS /glucose and incubated for 10 minutes at 37 °C. In the case of VUF16840, cells were preincubated for 2 hours with 100 nM or 1 µM /well final concentration in DMEM / 10% FBS media before SNAP labelling. Following that, the SNAP labelling protocol described above was used; however, the VUF16840 compound remained present during the whole course of the labelling and the imaging. Following the ligand incubation step, the cells were equilibrated to room temperature for 10 minutes before imaging.

2.3.4. Time-series, Single Focal Plate Imaging

Confocal images of the cells were taken to assess receptor localisation in different conditions. For confocal imaging, SNAP Surface 488 was imaged using the 488 nm line of the argon laser for excitation at 2% laser power, with emission collected through a bandpass (BP) 505-610IR filter. The ligand was added to the wells immediately before imaging to capture potential receptor re-localisation. Images were collected every 30-60 seconds over a 20–30-minute period. Images were acquired using zoom at 3x, and scan speed at 2.05 µs/pixel.

2.3.5. Imaging Receptor Co-localisation with Early Endosome Marker

To assess the co-localisation of the receptor with early endosomes, CellLight™ Early Endosomal marker - red fluorescent protein (RFP) BacMam 2.0 (Thermo Fisher Scientific, UK, cat. N C10587) was used. This endosomal label is based on BacMam technology, where the fusion construct of the Rab5a (Early

endosome delivery sequence) fused to TagRFP is packed in the insect virus baculovirus, which delivers the construct into the cell and releases it for transcription. Cells were plated in 8-well chambers (described in 2.1.6.2. 8-well Plate Cell Seeding) and incubated for 24 hours at 37 °C in 5% CO_2. Early Endosome-RFP marker was then added to the wells at ~2 µl reagent / 10,000 cells (calculated based on the cell density for each cell line). After at least 16 hours of overnight incubation with the marker at 37 °C in 5% CO_2, cells were SNAP-labelled as described in 2.3.2. with SNAP-Surface Alexa Flour 488. Following SNAP labelling and ligand addition (if applicable), cells were equilibrated to room temperature for 10 minutes before imaging. For the microscope set-up, SNAP Surface 488 was imaged using the 488 nm line of the argon laser for excitation at 2% laser power, with emission collected through a BP495-543 IR filter. The Early Endosomes RFP marker was imaged using the 561nm line of Diode pumped solid state (DPSS) laser for excitation at 2% laser power, with emission collected through a BP 550-610 IR filter. The microscope was set up as previously described (in 2.3.1. Microscope Set-up). Confocal images were captured on Zoom 3x with 2.05 µs/pixel laser speed. The pinhole was set to 1 AU in the SNAP488 channel (36 µm) and close to 1 AU (48 µm) on the RFP channel. The two channels were imaged sequentially. At least three individual experiments were carried out for each cell line or condition. On each individual experiment day, images were collected from two separate wells per condition.

2.3.6. Imaging Receptor Co-localisation with LAMP-1, Lysosomes Marker

The cells were plated in 8-well chambers (described in 2.1.6.1 8-well cell seeding) and incubated for 48-72 hours at 37 °C in 5% CO_2. After the incubation period, the SNAP-tagged receptor was SNAP-labelled with SNAP-Surface 549 (New England BioLabs Ltd., UK). The media was removed from the cells, and 10 µl/well of SNAP-Surface 549 was added at a final concentration of 500 nM in a final volume of 200 µl HBSS/glucose buffer and incubated for 30 minutes at RT and protected from light. Following the incubation, the cells were washed once with 200 µl/well HBSS/glucose before fixing with 200 µl /well of 4% paraformaldehyde (PFA, Sigma Aldrich, UK) for

15 minutes at RT. After fixing, the cells were washed 3 times with PBS each for 3 minutes of incubation. The fixed 8-well chambers were kept in parafilm and tin foil in the fridge until the next staining step. Following that, the cells were permeabilised with 200 µl 0.3% Triton X-100 per well for 5 minutes at RT, then washed 3 times 3 minutes with PBS. The cells were blocked using 200 µl / well 2% bovine serum albumin (BSA, Sigma Aldrich, UK) diluted in PBS for 1 hour at RT. The blocking solution was removed from the cells and the LAMP-1 Alexa Flour™ 488 antibody (Thermo Fisher Scientific, UK, Catalog # **MA5-18121**) diluted in 1:100 in 2% BSA was added and incubated for 1.5-2 hours (RT). Cells were then washed for 3 x 5 minutes with 0.1% Triton/PBS solution. For nuclei stain, 10 µl/well Hoechst 33342 Solution (final concentration 10 nM, Thermo Fisher Scientific, UK) was added in PBS buffer to the cell for 10 minutes and then washed 2 times with PBS. Cells were kept in PBS, wrapped in foil and placed in the fridge until imaged.

For the microscope set-up, SNAP Surface Alexa 549 was imaged using the 561 nm line of DPSS laser for excitation at 2% laser power, with emission collected through a BP 566 – 679 IR filter. The LAMP-1 Alexa 488 maker was imaged using the 488 nm line of the argon laser for excitation at 2% laser power, with emission collected through a BP 499 – 552 IR filter. The Hoechst nuclei staining was imaged using the 405/30 diode laser for excitation at 2% laser power, with emission collected through a BP 410-481 IR filter. The slice depth was matched, and the pinhole was set around 1 AU for all channels: the SNAP 488 channel (37 µm), the SNAP 549 channel (44 µm) and the DAPI channel (32 µm). The confocal image was captured on Zoom 3x with 2.05 µs/pixel laser speed, and the channels were imaged sequentially. At least three individual experiments were carried out for each cell line or condition. On each individual experiment day, images were collected from 2 separate wells per condition.

2.4 Fluorescence Spectroscopy

2.4.1. Microscope Set-up

All experiments were performed on a Zeiss 880 LSM confocal microscope (Carl Zeiss, Germany) with a 40x c-Apochromat 1.2 NA water immersion objective and 488 nm line of an argon laser with emission collected through a 508-691 nm BP emission filter for the SNAP Surface 488 channel. The temperature of the microscope room was controlled and set to 24 ± 2 °C for all measurements. The precise pinhole, gain, laser scan speed, laser power and zoom were varied depending on the type of measurement and are detailed in the sections below. All experiments were carried out with live cells.

2.4.2. SNAP Labelling

Cell membrane impermeant SNAP-dye, SNAP-Surface Alexa Flour 488, was used to label SNAP-tagged receptors plated in 8-well chambers. The SNAP labelling protocol was carried out for FCS, FRAP and RICS experiments as described in 2.3.2. SNAP labelling with a 100 nM SNAP dye at final concentration.

2.4.3. Ligand Addition

In specific experiments, selected wells were treated with either CXCL12 (CXCR4 and ACKR3 agonist) or It1t (CXCR4 antagonist). The ligand addition is described further in 2.3.3 above.

2.4.4. Fluorescence Correlation Spectroscopy (FCS)

2.4.4.1. Calibration

Before each Fluorescence Correlation Spectroscopy (FCS) measurement, the microscope was calibrated, and radial and axial parameters of the detection volume were determined with a dye of known diffusion co-efficient, ATTO 488 (Merck, Germany). The ATTO 488 dye was diluted with HPLC water (CHROMASOLV^{TM} Plus, Honeywell, Germany) in two different concentrations and 200 µl/well was added into two separate chambers of an 8-well slide. The high concentration (1 µM) chamber was excited using 0.015% 488 nm laser power to adjust the count rate (CR) for ATTO488, which was set to be ~300 kHz, and the objective correction collar position and the pinhole position was adjusted to give the maximum count rate. Following that, the low concentration (20 nM) of ATTO 488 was excited using 1.5% laser power, and the Count Per Molecule (CPM) was checked (appropriate count is ~80 kHz) to confirm alignment was optimal. The fluorescent fluctuations for the autocorrelation curve (AC) acquisition were then collected of 20 nM ATTO488 for 10 times 10 seconds reads (Figure 2.2/A). Following that, a read for Photon Counting Histogram (PCH) calibration was taken for 60 seconds (Figure 2.2/B).

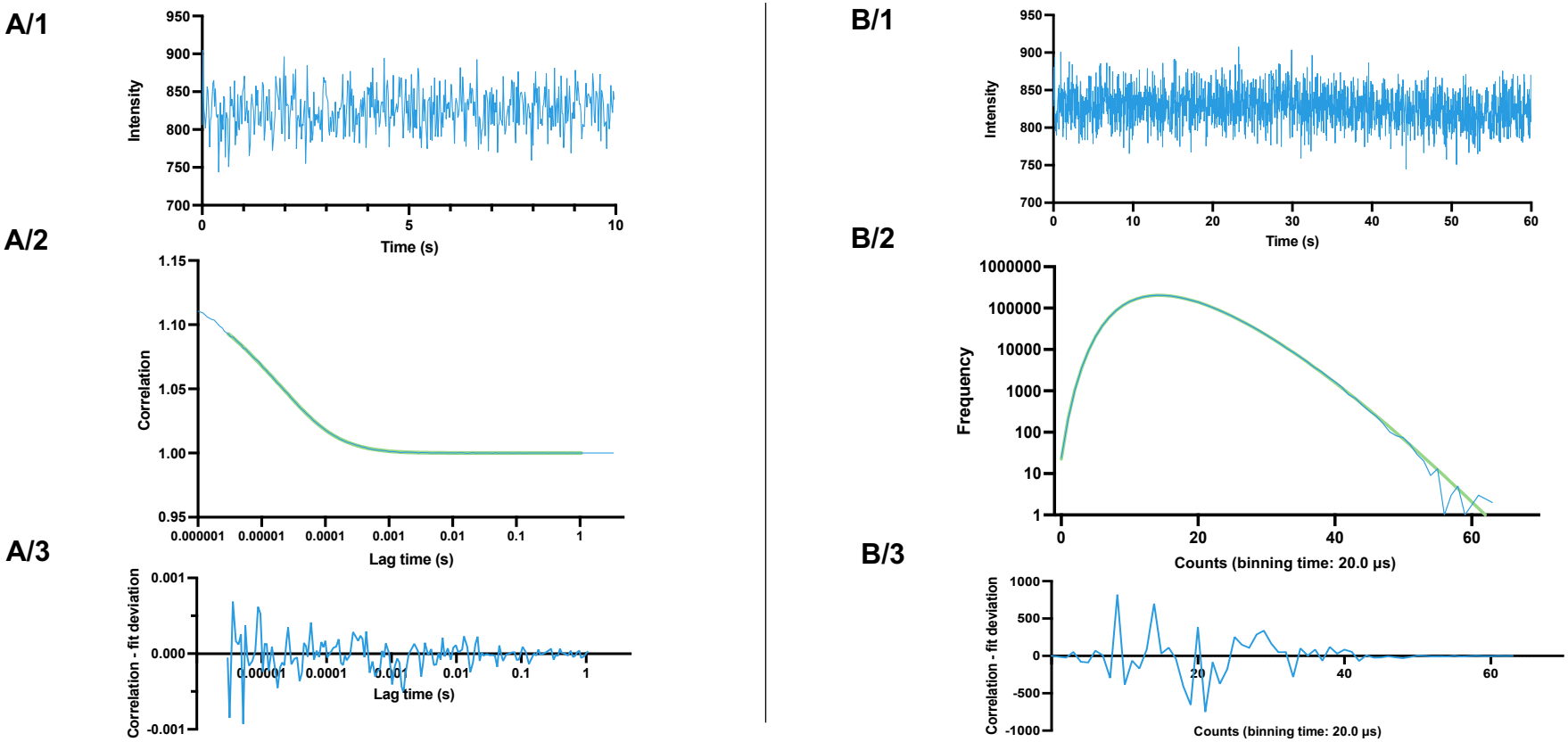

***Figure 2.2: FCS calibration with ATTO dye**. **A - Autocorrelation curve**: **A/1:** raw data read, **A/2:** Autocorrelation curve with a one-component 3D diffusion component fit, the blue line is the data and the green line is the fitting. **A/3:** Correlation – fit deviation of the Autocorrelation which reflects the fit of the data to the curve (zero represents the best fit). **B – PCH: B/1**: raw data read, **B/2**: one component PCH fit with binning time 20 µs, the blue line is the data and the green line is the fitting. **B/3**: Correlation- fit deviation of PCH.*

2.4.4.2. Cell-based FCS Measurements

The cells were located and brought into focus using brightfield illumination. After the localisation of cells, live imaging with Alexa488 channel was used to find appropriate cells for FCS measurements (512x512 pixels, Zoom 3x, pinhole 1AU). The fluorescence gain was set to avoid saturation on each experimental day and make sure that cells with optimal expression for FCS analysis were within the dynamic range for imaging. In the case of FCS, appropriate cells were those which did not overlay with each other, showed lower fluorescence signal and were not saturated. First, the detection volume was positioned on the x and y axis over the cell cytosol by moving the stage (Figure 2.3/A). Following that, the z-position was modified manually so the upper membrane of the cell was in focus. A z-scan with 0.25 µm steps for ± 2 µm was performed to define the peak of the intensity, which indicated the precise position of the plasma membrane (Figure 2.3/B). The z-scan data and z-scan curve were saved for every cell measurement. Fluorescence fluctuations were recorded on the apical plasma membrane using 488 nm excitation at 0.1% laser power for 30 seconds. The raw data read (Figure 2.3/C) of the fluctuation trace was saved and analysed (see 2.5.1. and 2.5.2).

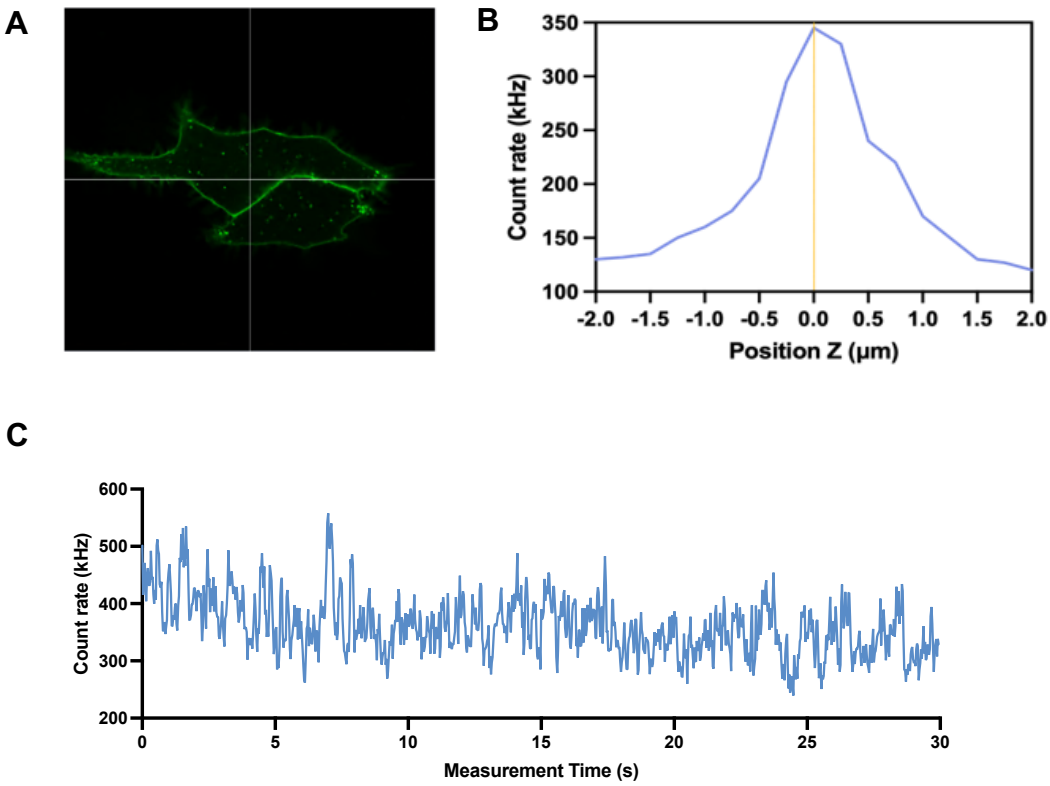

Figure 2.3: Cell-based FCS. A: *Position detection volume in x-y.* ***B:*** *Position detection volume in z.* ***C:*** *Representative example of fluctuation trace of cell membrane read.*

2.4.5. Fluorescence Recovery After Photobleaching (FRAP)

The cells were located and focused in brightfield, and the gain was set around ~800 and kept the same for the whole course of the experiment. The focus was manually placed on the basal membrane. Brighter cells were chosen to reach appropriate fluorescence intensity, and they were checked with the range indicator to avoid saturation. The circular bleaching area was set on the cell before the measurement. The FRAP read was taken with 488 nm excitation (500-550 nm emission filter, integration mode) on 2% laser power, 512x512 pixels, 1.5 Airy unit (pinhole diameter 56 µm), and zoom 3 with 1.52 µs pixel dwell time. The circular bleaching area was set to a 20-pixel (2.73 µm) diameter (Figure 2.4/A red circle). Following 5 cycles of baseline read, the bleaching area was bleached using 100% laser power for 50 iterations and the fluorescence recovery measured for a total number of 60 cycle scans (~1 second/cycle). Further FRAP experiments were carried out with varied sizes of circular bleaching areas (5,10,20,30, and 40-pixel diameter) following the same protocol.

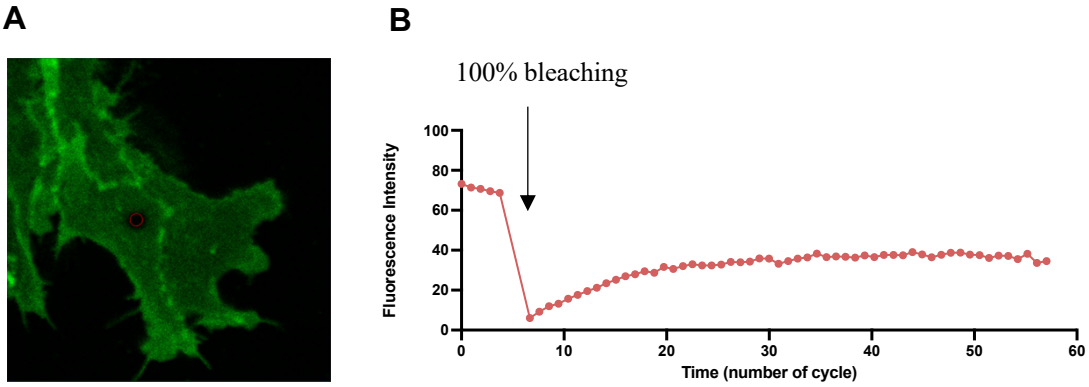

Figure 2.4: Fluorescence Recovery After Photobleaching (FRAP). A: *z-axis manually placed on the basal membrane; red circle represents the circular bleaching area.* ***B:*** *Raw data of the fluorescence intensity change of the bleached area over time.*

2.4.6. Raster Image Correlation Spectroscopy (RICS)

Before RICS measurement, the microscope was calibrated by FCS calibration with ATTO 488 dye (described in 2.4.4.1. Calibration). After focusing on the cells in brightfield, the SNAP488 channel was selected (488 nm excitation, 500-550 BP emission, 1AU pinhole), and the channel acquisition was switched to Photon Counting mode. After locating the cell, the focus was adjusted manually to the basal membrane. The pixel size was set to 50 nm (oversampling; Zoom 17x), and the field of view was 256x256 pixels with a pixel dwell time of 8.24 µs. A 100-frame image time series was captured with 0.3% laser power.

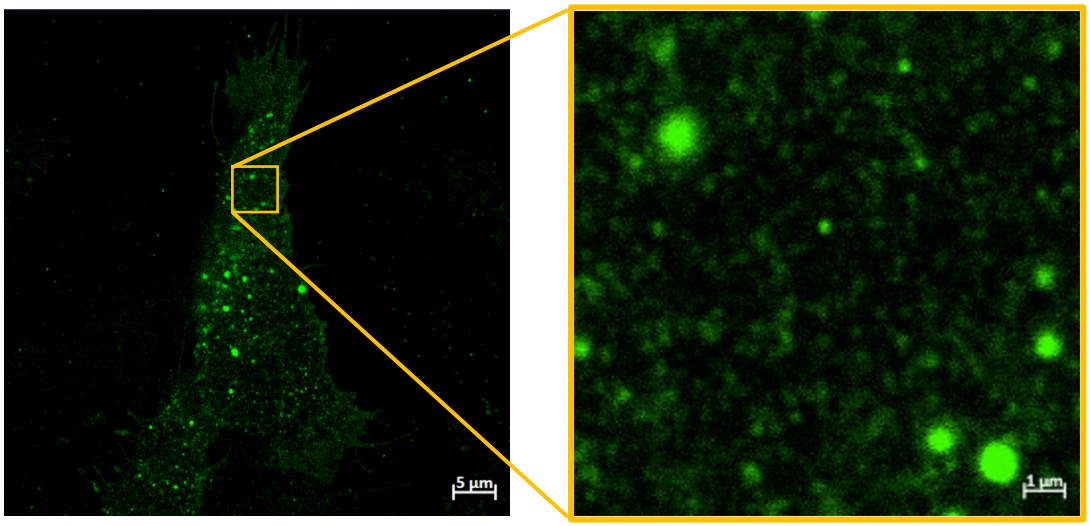

Figure 2.5: Raster Image Correlation Spectroscopy. *Representative example cell with z-axis focus on the basal membrane. Inset: the pixel size is set to 50 nm with Zoom 17x and the field of view 256x256 pixels. Scale bar = 5 µm.*

2.5. Data Analysis

2.5.1. FCS Data Analysis

2.5.1.1. FCS Calibration Analysis

FCS analysis was performed using ZEN Black software (Carl Zeiss, Jena, Germany). The calibration parameters of the ATTO 488 provided information about the dimensions and integrity of the detection volume (volume radius and structural parameters (height to diameter ratio)). To obtain the ATTO 488 autocorrelation curve (AC), the 10 seconds fluorescence fluctuation reads were fitted into a single three-dimensional (3D) diffusion component representing the free-moving ATTO 488 dye with a pre-exponential to account for fluorophore photophysics (triplet state) (Figure 2.2.A). All 10 autocorrelation curves from the calibration read were plotted and fitted globally to obtain the calibration parameters. The trace fit, and the diffusion parameter of ATTO 488 were checked based on the expected values from the literature [98]. From the fitted diffusion time and the known diffusion coefficient of ATTO488 ($4x10^{-10}$ m^2/s) the confocal radius (ω_0) and the half height of the volume (ω_2) were calculated (see equation below).

$$\omega_0 = \sqrt{4 \cdot Diffusion\ time(s) \cdot D_{\mathrm{ATTO}}\left(\frac{m^2}{s}\right)} \qquad (1)$$

$$\omega_2 = \text{Translation Structural Parameter (S)} \cdot \omega_0 \qquad (2)$$

Following that, the 60 seconds fluorescence fluctuation read was fitted in a one-component PCH model with a binning time of 20 µs to check the fit, brightness and first order correction of the read (Figure 2.2/B). These numbers of the PCH ATTO 488 were noted and compared to the expected values.

2.5.1.2. FCS Analysis of the Cell Measurement

Cell FCS data was analysed using ZEN Black software (Carl Zeiss, Jena, Germany). To compensate for the possible bleaching of the fluorophore, the data corresponding to the first ~5 seconds of the FCS read were removed [84].

Then, the autocorrelation curve (AC) was fitted to a two-component diffusion model containing a three-dimensional (3D), fast-moving component to account for any free SNAP-488 label and a two-dimensional (2D), slow-moving component indicating the plasma membrane-bound labelled receptor as previously described for β2-adrenoreceptor [79]. In the 3D diffusion model, the autocorrelation function (G(τ)) that describes the diffusion of the fluorescent species, can be defined as the following algebraic equation,

$$G(\tau) = 1 + \frac{A}{N} \cdot \sum_{i=1}^{m} \cdot f_i \cdot \left(1 + \frac{\tau}{\tau_{D_i}}\right)^{-1} \cdot \left(1 + \frac{\tau}{S^2 \cdot \tau_{D_i}}\right)^{-\frac{1}{2}} \quad (3)$$

where;

$$A = 1 + \frac{T}{1-T}\, e^{-\tau/\tau T} \quad (4)$$

N is the number of fluorescence particles with the τ_{Di} mean dwell time, and f_i is the fraction of the species *i,* from *m* total number of species, S is the structural parameter, which is the ratio of the vertical/axial radius. A is the triple state that defines the contribution of the fluorophore photophysics to the signal. The 2D diffusion model where S → ∞, G(τ) can be defined with the equation of,

$$G(\tau) = 1 + \frac{A}{N} \cdot \sum_{i=1}^{m} \cdot f_i \cdot \left(1 + \frac{\tau}{\tau_{D_i}}\right)^{-1} \quad (5).$$

The normalised form of the intensity autocorrelation function, G(τ), can be described with the following,

$$G(\tau) = 1 + \frac{\langle \delta I(t) \cdot \delta I(t+\tau) \rangle}{\langle I \rangle^2} \quad (6)$$

where angular brackets define the collective average. The intensity fluctuation δI(t) around the average intensity (I) at the time t, which is compared with the fluctuation at a later time point (τ) [79, 80]. For each time point, G(τ) is calculated and plotted against lag time (s), resulting in a sigmoidal decay function (Figure 2.6/B).

For the fitting, the structure parameter was fixed to 5, and the *triplet state relaxation time* was constrained to 1-10μs, while the *average dwell time of the first component* (representing the free SNAP-488) was constrained to 20-80μs as previously determined [79]. In cases where the autocorrelation curve could not be fitted with an asymptote of 1, an offset was introduced to facilitate the fit.

The average receptor dwell time (τ_D) and particle number (N) were obtained from the fit of the AC curve. The diffusion coefficient was calculated from the average dwell time (τ_D) of the SNAP-tagged receptor obtained from the AC curve and the beam waist radius of the detection volume (ω_0) determined from the ATTO488 calibration AC curve using the following equation,

$$D_{coefficient} = {\omega_0}^2/(4 \cdot t_D) \ . \qquad (7)$$

The particle number (N) was calculated from the total particle number (determined by the G(0) of the AC curve) multiplied by the fraction of the receptor diffusion component (τ_{D2}). The receptor density (N/μm^2) was calculated from the particle number and the waist radius (ω_0) with the following equation,

$$Density\ \left(\frac{N}{\mu m^2}\right) = N/(\pi \cdot {\omega_0}^2) \text{ [84].} \qquad (8)$$

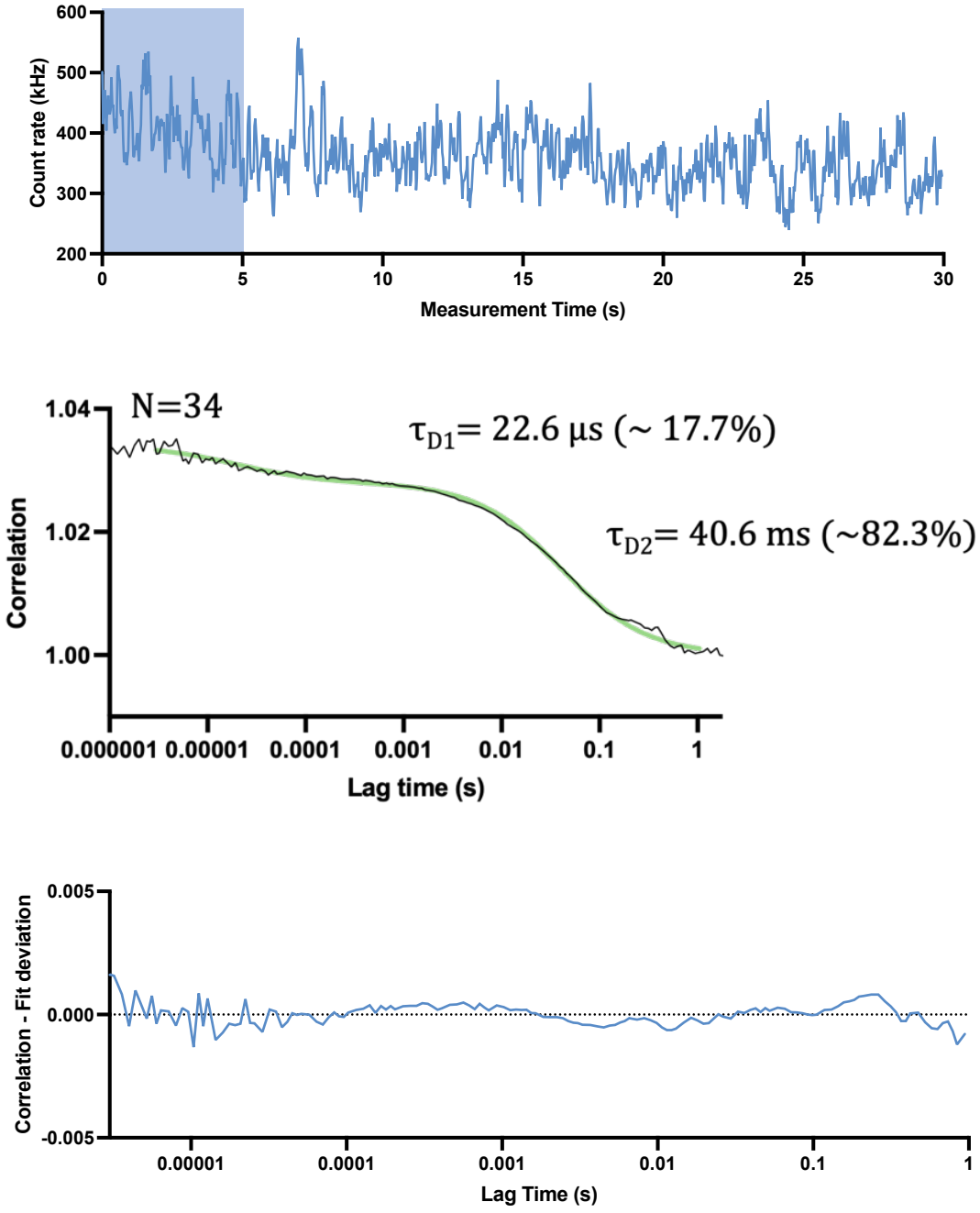

Figure 2.6: Cell-based FCS analysis. *Representative FCS read from SNAP-CXCR4 data set.* ***A: Raw FCS read*** *with the first ~5 seconds that were removed for fitting indicated with blue shading.* ***B****:* ***Autocorrelation curve*** *with a mixed 2D (receptor) and 3D (free dye) two-component model. The AC gives information about the particle number (N) and dwell times (τ_D) of the components with their percentage.* ***C: Correlation – Fit deviation*** *of the data, optimal correlations show minimal deviation from 0.*

2.5.2. Photon Counting Histogram (PCH) Analysis

The fluorescence fluctuation traces were also used for Photon Counting Histogram (PCH) analysis within the Zen Black software. The histogram stratifies fluorescence fluctuation trace based on the number of photons per time bin. The deviation of the histogram from a Poissionian distribution is used to determine the average molecular brightness of the diffusing species, which gives an indication of clustering or oligomerisation of the diffusing species. The binning time was set to 100 µs during the PCH curve fitting and *the first order correction value* was set to that determined from ATTO488 PCH calibration. Initially, a one-component PCH fit was used (Figure 2.7/A). In cases where there was a significant deviation from the fit at high photons per bin, a second component was added and a two-component PCH analysis was used. This indicated the presence of the receptor in clusters or higher oligomeric states [77, 79].

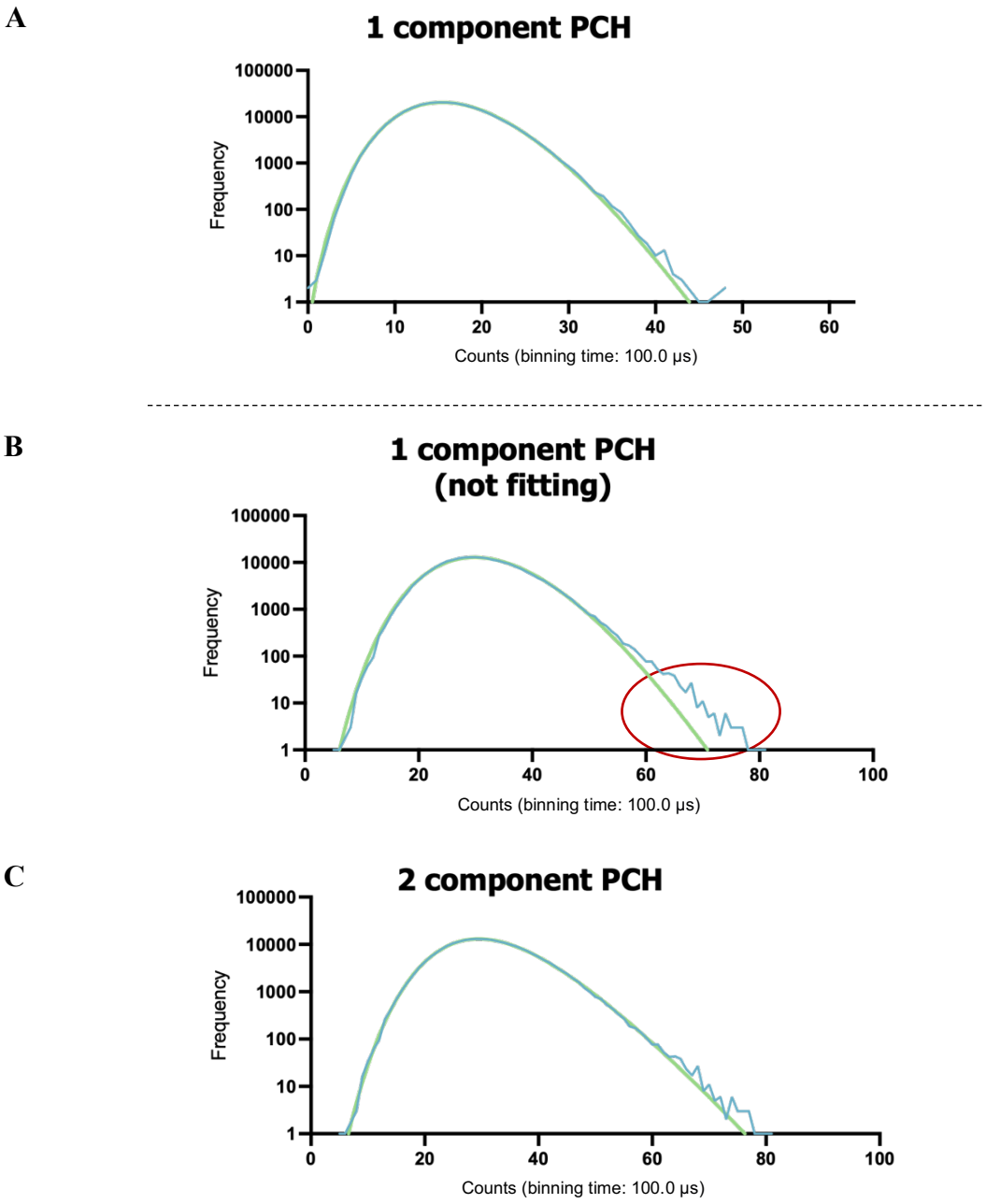

***Figure 2.7: PCH analysis**. **A:** One-component PCH fit of the representative data trace. The binning time was fitted to 100 µs. **B:** Representative data presented a significant deviation from the fit at high photons per bin (red circle), so a second component was added to the PCH fit **(C)**.*

2.5.3. FRAP Data Analysis

Data were analysed using the FRAP module in Zen Black software (Carl Zeiss, Germany). The fluorescence intensity of the bleached area was recorded over time (Figure 2.8/B). A non-cell background area of the same size was used for background correction (Figure 2.8/A right image, green circular area), and one of a non-bleached area in another cell in the field of view was used to correct for bleaching during scanning (Figure 2.8/A right image, blue circular area). An exponential recovery curve corrected for background and bleaching was fitted to provide information about the half time of recovery and mobility. The mobile fraction (MF) was determined as the percentage of the intensity of the recovery plateau compared to the pre-bleached intensity. The immobile fraction (IF) was calculated from the difference between the plateau intensity and the pre-bleached intensity. The half time of recovery ($\tau_{1/2}$) was obtained from the recovery curve. The *diffusion coefficient* (D_{FRAP}) was calculated via the following equation of

$$D = \omega^2 / (4 \cdot t_{1/2}) \qquad (9)$$

where $\tau_{1/2}$ (s) means the half-time recovery and ω (μm) is the radius of the bleached area.

A

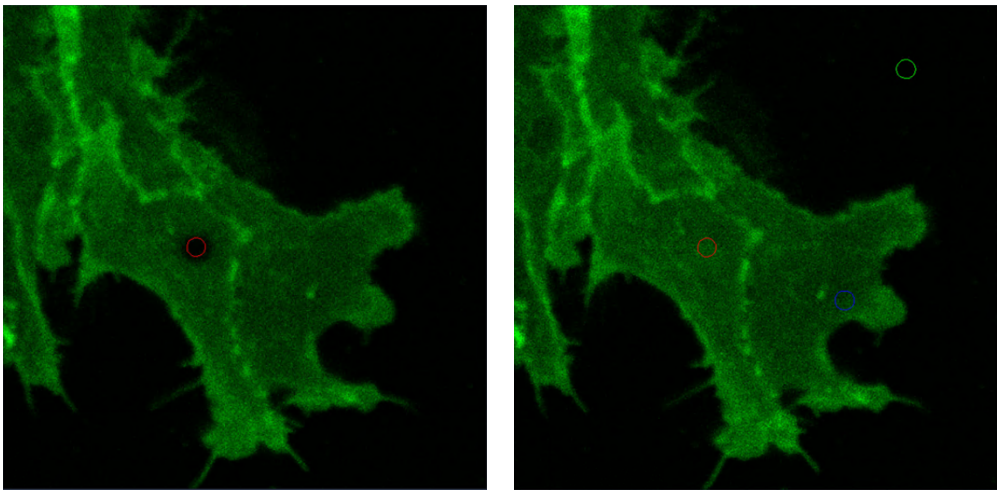

B

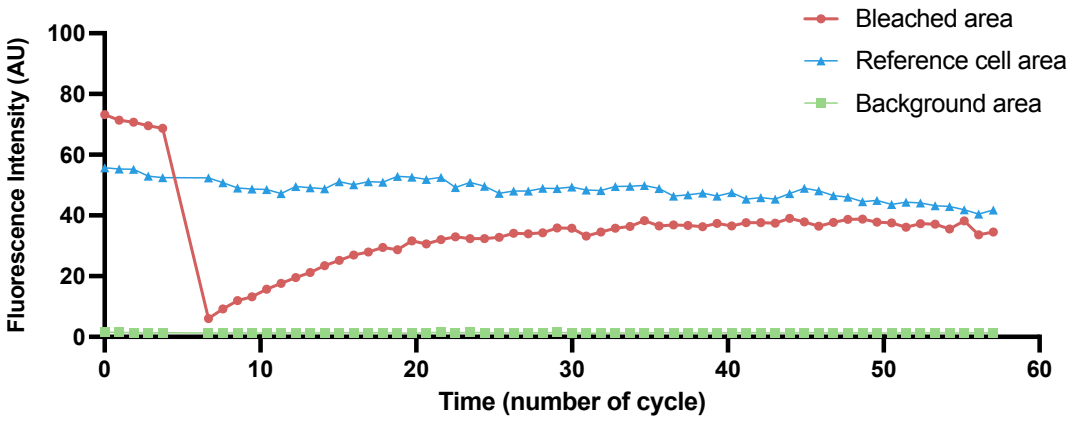

Figure 2.8: FRAP analysis. A: *Representative images of the basal membrane of the cell. The red area is the bleached area, the green circular area is the background area for correction and the blue circular area is the non-bleached reference cell area.* ***B:*** *Representative FRAP curve recording the fluorescence intensity change over time of the bleaching area (red curve). During analysis the background area fluorescence intensity (green curve) and the reference cell intensity (blue curve) are also considered.*

2.5.4. RICS Data Analysis

The RICS image series was analysed using the RICS module in Zen Black software (Carl Zeiss, Germany). Following calibration (*2.5.1.1. FCS Calibration Analysis*) and image acquisition, the RICS image series was visually inspected for z-axis movement, and the out-of-focus frames were excluded. A minimum of 50 continuous frames was set as a criterion for the analysis to keep the signal-noise ratio acceptable [99]. For background subtraction, the option of removing slowly moving structures was used and set to 5. The RICS image correlation model was set to a 2D diffusion model to yield information about the SNAP-tagged membrane-bound receptors. The geometric correction was set to 1, and the ω_0, lateral focus radius (mm) was set based on the calibration value of the individual experiment day. After the analysis set-up, the image autocorrelation was carried out, and the fit on the x and z-axis was checked (Figure 2.9). From the correlation, the diffusion coefficient (D_{RICS}) was calculated within the RICS analysis module [85].

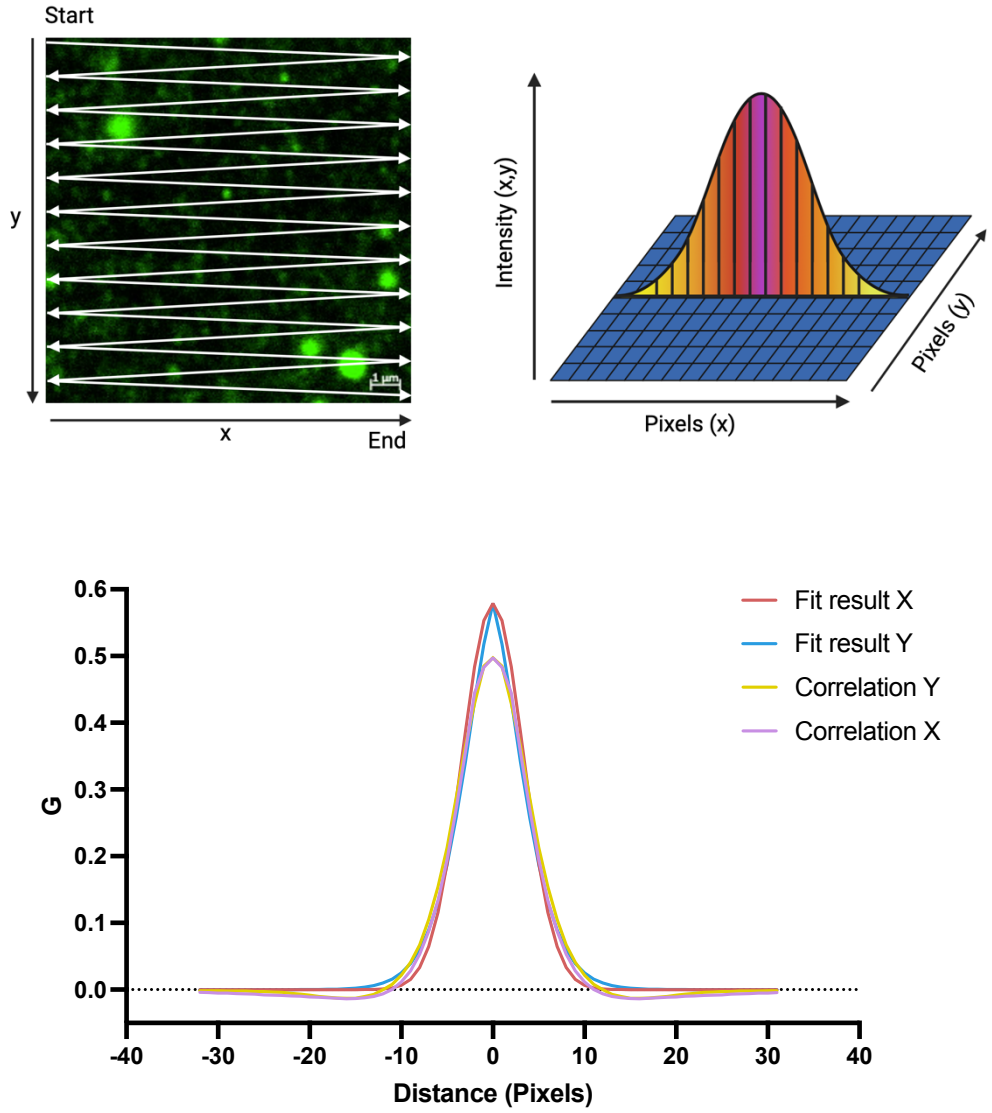

Figure 2.9: RICS image correlation curve. *Representative data with the image correlation fitting for the x- and y-axis of the raster image. The image demonstrates the raster scan across the image (white arrows) in the x-axis, while the y-axis represents the sequential lines (top left image). During analysis, the slowly moving components were removed, and a 2D reading can be extracted based on the distribution of pixel intensity to pixel position in the x- and y-axis (top right curve). For analysis, a 2D diffusion model can be fitted to the images, producing an autocorrelation curve for both the x- and y-axis. The figure was created with BioRender.com.*

2.5.5. Number and Brightness Analysis

The RICS image series data was also used for Number and Brightness (N&B) analysis. This alternative analysis was carried out in Zen Black software using the Number and Brightness (measured) module. After the image series was selected and the N&B module was applied, three separate images were created (see below Figure 2.10/A) for maximum intensity projection, number and brightness image channel. Three regions of interest (ROI) were selected with an area of ~12 μm^2 (Figure 2.10/B). Within the co-localisation section of the Zen Black software, the Number channel was chosen as the x-axis, and the Brightness Channel was chosen as the y-axis (Figure 2.10/C). The mean number of particles and the mean brightness were calculated by the module and fitted into GraphPad Prism for statistical analysis. The average number of brightness gives information about the oligomeric state of the receptors, compared against a monomeric control [100].

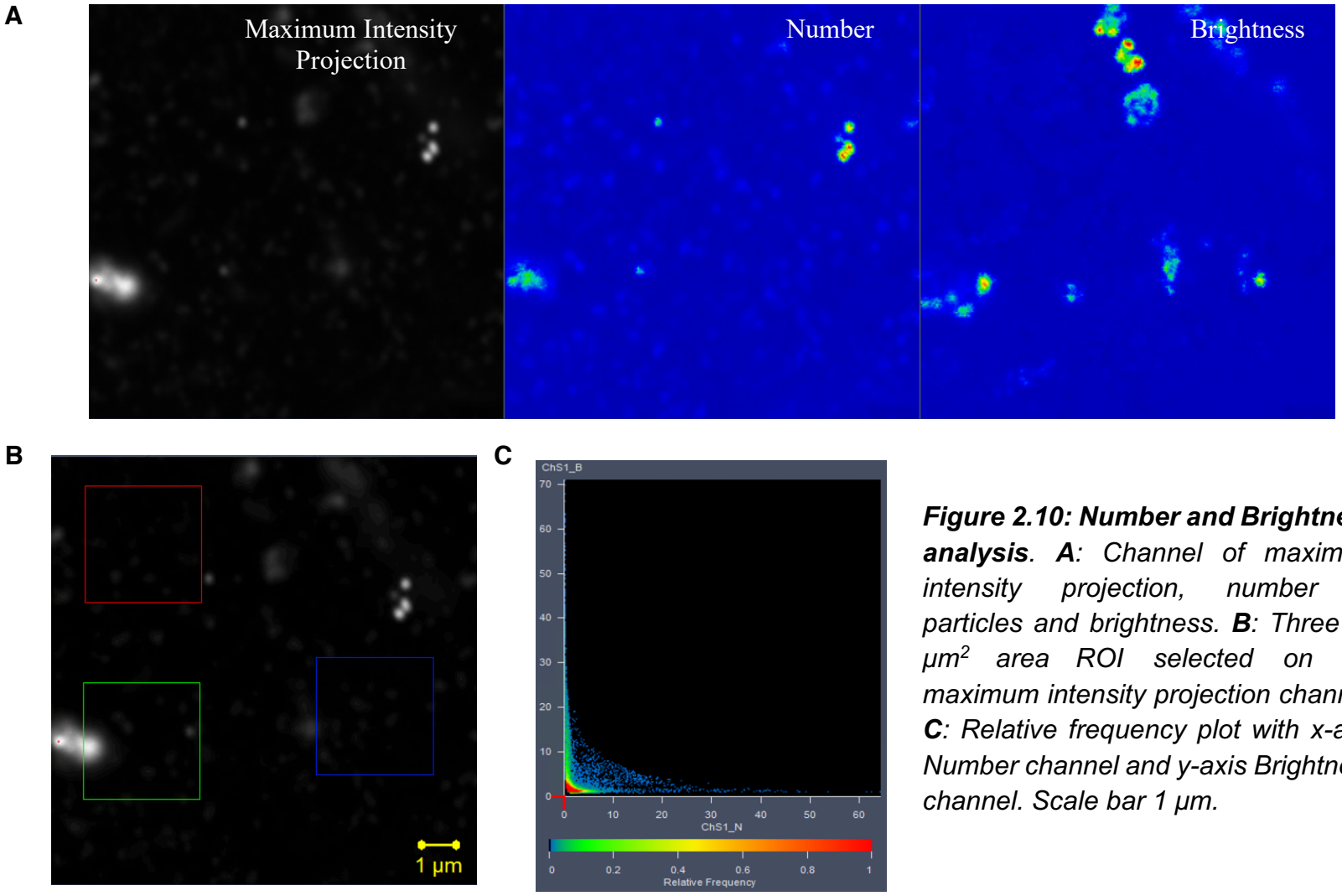

Figure 2.10: Number and Brightness analysis. ***A****: Channel of maximum intensity projection, number of particles and brightness.* ***B****: Three 12 µm² area ROI selected on the maximum intensity projection channel.* ***C****: Relative frequency plot with x-axis Number channel and y-axis Brightness channel. Scale bar 1 µm.*

2.5.6. Statistical Analysis of FCS, FRAP and RICS Data

The data above was exported to GraphPad Prism (GraphPad Software, San Diego, California, USA) to create figures and determine statistical significance where appropriate. The data represents 'n' individual cell data per condition and is presented with the mean $\pm$ SEM value with the number of individual experiments (minimum of 3 individual experiments per condition). The PCH data was illustrated with the % of cells required one or two-component fit. To compare multiple ligand-induced conditions (CXCL12 and IT1t) to vehicle conditions, one-way ANOVA followed by Tukey's multiple comparisons test was performed if $P < 0.05$ (statically significant). In the case of two conditions (vehicle and CXCL12), unpaired Student's t-test was used if $P < 0.05$ (statically significant). Significant changes with p values were noted on the graphs.

2.5.7. Early Endosomes Marker and LAMP-1 Marker Co-localisation Analysis Using Segmentation and Quantification of Subcellular Shapes (Squassh)

The segmentation and co-localisation analysis of the markers was carried out with the Squassh plug-in [101] in Image J software [102]. For the analysis, a minimum of 30 single focal plane images were collected from a minimum of 3 individual experiments per condition or cell line type. Firstly, these multi-channel images were exported from Zen Black software (Carl Zeiss, Germany) and converted to a Tag Image File Format (TIFF) file in Image J. After launching the Squassh plug-in, the converted TIFF image files were selected. Within the set-up, the Squassh plug-in parameters were defined as detailed in Table 2.1. The confocal setting of the microscope's *point-spread function* (PSF) helped improve the capacity of image segmentation. The set-up of the cell mask helped restrict the segmentation to certain regions of the image, such as the cells. The set-up values were kept the same across all studied images. Graphical output and statistical analysis were performed in R statistical software [103] as described in the SquasshAnalyst manual. The SquasshAnalyst was launched from R with the following script: *shiny::runGitHub("SquasshAnalyst", "a-rizk")*. Data input was then selected for the analysis, and the channels were named for their corresponding markers or labelling. Under the 'segmentation overview' tab, the segmentation quality was checked visually, and images with unsuccessful segmentation were excluded. In the 'Analysis' tab, the 'Colocalisation (signal)' was selected and matched with the appropriate channels. The SNAP-tagged receptor channel was selected for the 'Percentage of the channel', and the marker was selected for the "Colocalizing with" option. The analysed data was exported as .csv and fitted in GraphPad Prism (GraphPad Software, San Diego, California, USA). To statistically compare co-localisation between cell lines or conditions, one-way ANOVA followed by a two-sided Dunett's comparisons test was performed if $P < 0.05$ (statically significant).

***Table 2.1: Squassh plug-in settings**. List of the parameters within the plug-in and the chosen settings for the project, which were kept the same for all experiments.*

Squassh plug-in settings	
Parameter	*Chosen settings*
Background substraction	Kept default
Microscope's PSF	'Compute PSF for confocal microscopy'
Segmentation regulation	Set to 0.150
Minimal object intensity	0.05
Noise model	Set to the option for confocal microscopy: Poisson model
Cell mask	Set to the channel with the SNAP-labelled receptor
Output of segmentation	'Object outlines' and 'Colored objects'

2.5.8. Analysis of Average LAMP-1 and SNAP-tagged Receptor Intensity Per Cell

The imaging tiff data file used for Squassh analysis was further used to gain information about the average LAMP-1 fluorescence intensity per cell for each of the cell lines. The analysis was carried out in the Fiji (Image J) software [104]. First, the cells Hoechst33342 channel was separated and after thresholding, it was converted to a binary mask. Following that, the Hoechst33342 stained cells were counted using Particle analyses within the Fiji software. The images of the LAMP-1 and SNAP (receptor) channels were converted to 8-bit, and the threshold was set to 20-255. The total intensity of the LAMP-1 and SNAP-tagged receptor channels was extracted separately by selecting a rectangular ROI area covering the whole field of view. To retrieve the average LAMP-1 or SNAP-receptor intensity per cell, the total intensity of the LAMP-1/receptor channel was divided by the number of cells in the corresponding Hoechst33342 channel. The calculation was carried out in Microsoft Excel (Microsoft Corporation) and in GraphPad Prism (GraphPad Software, San Diego, California, USA). To statistically compare the average LAMP-1/ SNAP-tagged receptor intensity per cells between cell lines, one-way ANOVA followed by Tukey's multiple comparisons test was performed if $P < 0.05$ (statically significant).

2.5.9. Functional Assays Analysis

2.5.8.1. Bystander Arrestin Recruitment Assay (K-Ras)

The data was fitted in GraphPad Prism (GraphPad Software, San Diego, California USA) and was baseline-corrected to the corresponding vehicle condition. For the statistical analysis, grouped data from a minimum of 3 individual experiments were used. For each experiment, the fold change was calculated per group from the baseline-corrected average with the equation of,

Difference = Value (CXCL12 condition) / Baseline (basal condition). (10)

To compare fold change of the different cell lines and transfection condition (with or without GRK2), one-way ANOVA followed by Tukey's multiple comparisons test was performed if $P < 0.05$ (statically significant).

Chapter 3: Plasma Membrane Organisation and Dynamics of CXCR4

3.1. Introduction

The G protein-coupled receptors (GPCRs) are the focus of intense research investigating their pharmacological properties in order to harness them for drug development [105]. Through structural biology studies, insights into the mechanism of ligand binding has been elucidated, as well as information concerning receptor conformations and the mechanisms of receptor activation [106, 107]. In addition to the structural details, the discovery of compartmentalised signalling has provided a more complex and in-depth picture of GPCR signalling and regulation based on their sub-cellular location [36]. The compartmentalisation of the receptor-ligand complex within a specific subcellular location, along with other signalling proteins, has been determined to play a role in defining particular signalling pathways [108, 109]. Moreover, previous studies suggested that the organisation of receptors into dimers and oligomers could influence their function and trafficking [110-112]. For example, it has been shown that adenosine A_{2A} receptors are functional when in homodimer form, but not when organised in monomers at the cell surface [113]. Another study presented evidence that dimer formation for the adenosine A_3 receptors can alter ligand binding affinity [114]. Upon receptor activation, monomer, dimers and higher order oligomers can redistribute into clusters in clathrin-coated pits, which can change their dynamics at the cell surface [115].

As most GPCRs are located within the plasma membrane, elucidating their spatial organisation in specific membrane domains could provide valuable information about their local regulation and signalling [77, 116]. Advanced microscopy techniques such as stochastic optical reconstruction microscopy (STORM), fluorescence lifetime imaging microscopy (FLIM) and advanced spectroscopy techniques such as Fluorescence correlation spectroscopy (FCS) have been developed to gain a better understanding and higher spatial and temporal resolution of the dynamics of GPCRs within the plasma membrane [117, 118]. A study with the A_3 receptor showed two different receptor populations at the plasma membrane, suggesting that receptors can form heterogeneous populations with different dynamics and characteristics in

distinct membrane microdomains [119]. This also supports the importance of investigating the spatial and temporal dynamics of GPCRs within the plasma membrane.

Fluorescence correlation spectroscopy (FCS) is an advanced spectroscopy technique which can provide direct dynamic information about the movement of fluorescently labelled species within a defined, small detection region. The FCS technique (detailed in Chapter 1) is based on a laser-illuminated confocal detection volume and detecting the fluctuation in fluorescence intensity created by fluorescent molecules diffusing through it [76, 78]. FCS can detect a wide range of diffusion rates (diffusion coefficients (D) from ~0.02 to 200 $\mu m^2/s$), making it suitable for detecting the dynamics of membrane-bound receptors [77, 79, 80]. The detection volume of FCS is ~ 0.2 fl (~1x 0.3 μm), which makes it possible to locate it in specific cell compartments, such as the plasma membrane, and assess the receptor organisation in subcellular regions [77]. The FCS approach has been previously used to investigate subcellular ligand-receptor complexes [120] and to measure the ligand-induced changes in diffusion rate and organisation of different GPCRs, such as β2 adrenoreceptor [121], A1-adenosine receptor [80] and histamine H1 [122]. Another advantage of FCS is its single molecule sensitivity, which allows it to measure the dynamic properties of receptors when express at endogenous levels [79].

From fluorescence fluctuations traces, it is also possible to gain knowledge about the oligomeric status of receptors via Photon Counting Histogram (PCH) analysis which has been used to study several GPCRs [123]. PCH analysis estimates the molecular brightness of the species within the detection volume, which is proportional to the number of fluorescence particles. A change in the average brightness indicates a change in the mass and implicates a change in the oligomeric status of the measured receptor population [76]. PCH analysis has been used previously to show the dimerisation of many GPCRs, including 5HT2A serotonin receptor, M1 and M2 muscarinic acetylcholine receptors [123].

While FCS is a tool for assessing the receptor dynamics within the plasma membrane, one of the main limitations of this technique is that it is unable to detect immobile fluorescent species [124]. Thus, combining FCS measurements with the Fluorescence Recovery After Photobleaching (FRAP) technique can provide information about the immobile species of receptors [125] (a more detailed description of FRAP is in Chapter 1). FRAP measurements assess the mobility and diffusion of receptors over a larger membrane area than FCS, which gives insight and a more complete view of the receptor dynamics on both the nano and micro scale [76]. Many previous studies used the combination of FCS and FRAP techniques to investigate receptor dynamics and mobility. Gondin et al. previously used the combination of FCS and FRAP techniques to investigate different ligand effects on the membrane dynamics of the μ-opioid receptor, where they showed increased receptor clustering and receptor number at the plasma surface upon agonist DAMGO addition [84]. Another study with epidermal growth factor receptors (EGFRs) showed a decrease in the diffusion coefficient of the receptor and an increased immobile fraction upon ligand stimulation. They suggested that the changes in the dynamics are due to the activated EGFR attached to the cytoskeleton or other slow-moving structures therefore slowing down their diffusion within the plasma membrane [126].

The CXC chemokine receptor 4 (CXCR4) is a well-characterised class A GPCR known to canonically signal through a G protein-dependent pathway [64]. Due to its pro-oncogenic role and participation in viral and immune diseases, CXCR4 has become an important drug target [57, 127, 128]. Upon agonist (CXCL12) activation, CXCR4 is phosphorylated by G protein-coupled kinases (GRKs), which inoke the recruitment of β-arrestins [64, 129]. The binding of β-arrestins results in G protein uncoupling and leads to receptor endocytosis via a clathrin-dependent pathway [130, 131]. Following CXCR4 internalisation, the receptor mainly trafficks towards lysosomal degradation [74]. Previous studies showed that CXCR4 in the basal condition is located at the plasma membrane and organised mainly as monomers and dimers; however, CXCL12 binding resulted in a significantly reduced monomeric and dimeric state while presenting an increase in nanocluster numbers [132]. A

recent study from Işbilir. et al. used the agonist ligand CXCL12 and antagonist IT1t to assess the change in oligomerisation and dynamics of CXCR4. They found that CXCL12 increased clustering and receptor internalisation, which increased over time. Moreover, they highlighted that IT1t could distribute dimer formation and change the stoichiometry towards a monomer state of the receptor [133]. While these studies presented significant findings about CXCR4 oligomerisation, there are still some missing pieces about the spatial and temporal resolution of CXCR4 at the plasma membrane.

This chapter explores the dynamics and organisation of CXCR4 within the plasma membrane. Using confocal imaging, we collected information about the distribution of the CXCR4 receptor in basal and ligand-stimulated conditions. Moreover, we provided valuable insight into the receptor dynamics at a nano and micro scale using FCS and FRAP techniques. In addition to the basal dynamics of the receptor, we assessed the agonist- and antagonist-induced changes in the receptor organisation. Moreover, these experiments served as an important optimisation step to evaluate the dynamics of a related yet-uncharacterised chemokine receptor, ACKR3 (see Chapter 4).

3.2. Methods

3.2.1. Cell Culture

Human embryonic kidney 293 Glosensor™ (HEK293G) SNAP-CXCR4 stable cells were used. Passaging, freezing, thawing, and seeding the cells to 8-well coverslips have been described in Chapter 2.1 Cell Culture.

3.2.2. Confocal Microscopy

3.2.2.1. SNAP Labelling

The SNAP-tagged receptor was labelled with SNAP-Surface Alexa Flour 488 (New England BioLabs Ltd., UK) impermeable dye in 8-well chambers. The SNAP labelling protocol is further described in 2.3.2. SNAP labelling.

3.2.2.2. Ligand Addition

In the selected experiments, the cells were treated with either 10 nM CXCL12 (agonist) or 1 μM It1t (antagonist). The process of ligand addition is described in 2.3.3. Ligand addition.

3.2.2.3. Microscopy Set-up

Live cells were imaged on a Zeiss 880 LSM confocal microscope (Carl Zeiss, Germany) with a 40X c-Apochromat 1.2 NA water immersion objective using the 488 nm line of an argon laser with emission collected through a 508-691 nm BP filter. The Alexa 488 channel was selected, and time series and single focal plate images were taken with 2% laser power on Zoom 3x (described in detail in 2.3.1 and 2.3.4.).

3.2.3. Fluorescence Correlation Spectroscopy (FCS)

FCS was carried out are described in detail in the General Methods and Materials chapter under 2.4.4. Fluorescence Correlation Spectroscopy and 2.5.1 FCS data analysis. FCS reads were collected for basal condition and ligand-stimulated conditions (CXCL12 and It1t). Data from a minimum of 30

cells from at least 3 independent experiments was collected for each condition. Following FCS analysis, data were presented and statistically analysed in GraphPad Prism (described in 2.5.3.). To compare vehicle to ligand-induced effect, one-way ANOVA followed by Turkey's multiple comparisons test was performed ($P < 0.05$ statically significant). Photon Counting Histogram (PCH) analysis was also carried out (described in 2.5.2) on the same data. The PCH data was illustrated separately in each condition with the % of cells that required a two-component fit. The data were fitted in GraphPad Prism (described in 2.5.3.) and one-way ANOVA followed by Turkey's multiple comparisons test was performed ($P < 0.05$ statically significant) to compare the percentage of the second component fit between basal, CXCL12 and It1t condition.

3.2.4. Fluorescence Recovery After Photobleaching (FRAP)

3.2.4.1. Optimisation of FRAP Parameters

FRAP parameters were optimised before the final data measurement protocol described in 2.4.5 Fluorescence Recovery After Photobleaching (FRAP). During optimisation, the following parameters were altered; gain, pinhole size, number of bleaching cycles and number of total cycles. The bleaching area was set to a 20-pixel diameter circle throughout the optimisation process. The variations of set-ups for optimisation are detailed below.

1. Gain was set around ~600-700 and the pinhole was set at 1 AU. For bleaching, 100% laser power was used for 100 iterations after 5 scans for a total number of 120 scans.
2. Gain was increased to ~800 while the other parameters were kept the same.
3. Gain was kept at ~800, the pinhole was increased to 1.5AU and the bleaching and total cycle numbers were kept the same.
4. Gain (~800) and the pinhole (1.5AU) were kept the same while the number of bleaching cycles was reduced to 50 iterations and the total number of scans was reduced to 60 cycles.

For optimisation, a minimum of 3 cells/experiment day were recorded in at least 2 individual experiments. Following that, the optimal set-up was used to collect the final dataset. The analysis of FRAP data (detailed in 2.5.3.) and statistical analysis (detailed in 2.5.3.) in Prism are described in Chapter 2 General Methods.

3.2.4.2. FRAP Measurement of Different Diameter Bleaching Area

The relationship between the size of the bleaching area and diffusion was studied independently by introducing different diameter-size circular bleaching areas. The set-up parameters of FRAP were kept the same as described in 2.4.5. however, the size of the circular bleaching area was changed. A total number of 5 bleaching sizes was measured, including circular areas with diameters of 5-pixel (0.37 μm^2 area), 10-pixel (1.47 μm^2 area), 20-pixel (5.87 μm^2 area), 30-pixel (13.22 μm^2 area) and 40-pixel (23.49 μm^2 area). The data was collected in basal condition and ligand-induced condition with 10 nM CXCL12. The ligand addition was carried out as described in 2.3.3. Ligand addition.

3.3. Results

3.3.1. Organisation of CXCR4 Under Basal and Ligand-stimulated Conditions

To study the organisation and dynamics of CXCR4, we used HEK293G cells stably expressing N-terminal SNAP-tagged CXCR4, previously characterised and tested in Dekker et al. [94]. To assess the CXCR4 location and the impact of ligand addition on the receptor distribution, confocal images were taken of SNAP-CXCR4 cells. First, the cells were SNAP-labelled with membrane impermeable SNAP-Surface Alexa Fluor 488 dye. Of note, as this dye is impermeable, any labelled receptor detected intracellularly will have been actively internalised after SNAP labelling either constitutively or due to ligand addition. Cells were treated with either vehicle (HBSS), 10 nM CXCL12 (CXCR4 agonist) for 10 minutes at 37 °C or 1 μM IT1t (CXCR4 antagonist) for 30 minutes at 37 °C. The details of the ligand addition are described in 2.3.3. chapter.

The confocal images (Figure 3.1) show that under basal condition, SNAP-CXCR4 is predominantly localised on the plasma membrane. Upon CXCL12 stimulation, the SNAP-CXCR4 receptor is partially internalised, and it can be visualised in bright intracellular vesicles while maintaining a reduced presence on the membrane (Figure 3.1). In the presence of the antagonist IT1t, SNAP-CXCR4 demonstrated a predominantly membrane distribution, with no major changes compared to the basal condition (Figure 3.1).

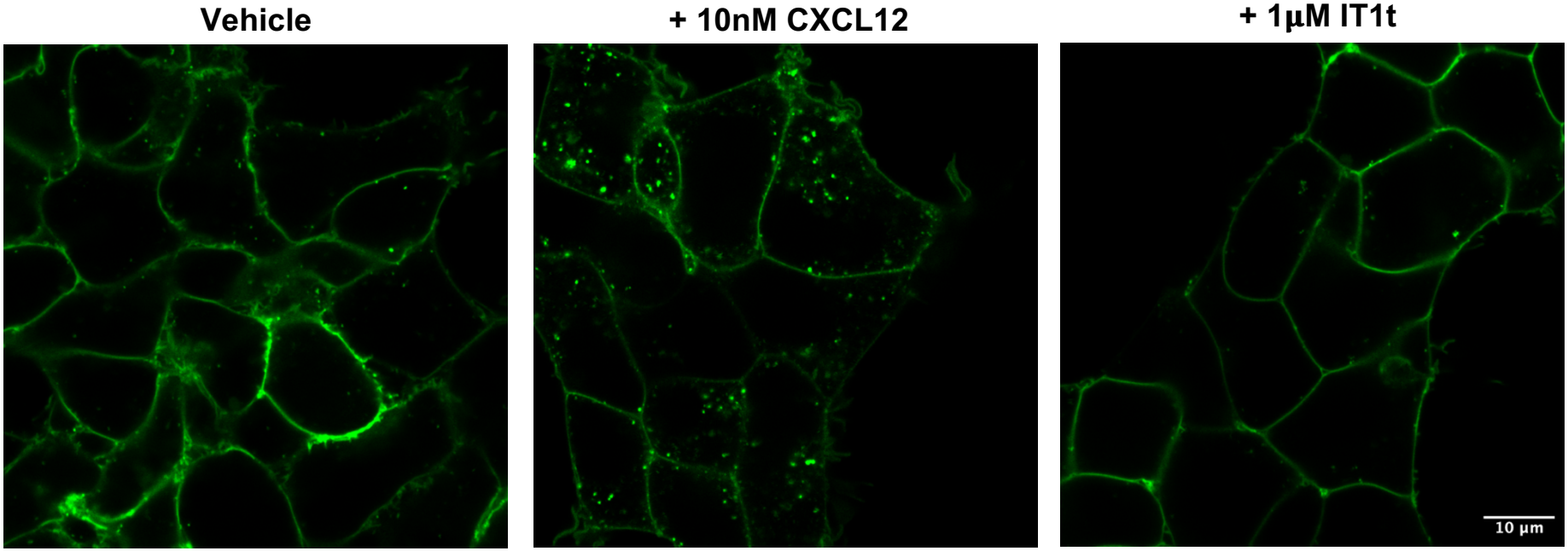

Figure 3.1: Localisation of labelled SNAP-CXCR4 under basal and ligand-stimulated conditions*. Cells were labelled with SNAP-Surface Alexa Flour 488 as indicated in Methods and imaged on Zeiss LSM 880 microscope using 40x c-Apochromat water immersion objective 1.2 NA on zoom 3x. Each image is a representative example from 3 independent experiments. Under basal condition, the majority of the SNAP-labelled CXCR4 receptor is on the plasma surface. The addition of 10 nM CXCL12 (agonist) increases the internalisation of CXCR4 receptors, while 1 µM IT1t (antagonist) presents predominantly membrane labelling. Scale bar = 10 µm.*

3.3.2. Plasma Membrane Organisation and Dynamics of CXCR4 – FCS Studies

To study the organisation and dynamics of CXCR4 at the plasma membrane, we used single point FCS data collected from an undefined area of the upper cell membrane. First, SNAP-labelled HEK293G SNAP-CXCR4 cells were imaged live on the confocal microscope (as described in section 2.4.4.2.) to find a suitable cell, and then the detection volume was positioned on the x-y axis over the cell cytosol. For the selected cell, the z-position was set on the upper membrane of the cell by moving the stage manually and carrying out a z-scan to detect the precise position of the membrane. Following positioning of the confocal volume to the membrane, the fluorescence fluctuations were recorded for 30 seconds. The FCS fluctuation trace (Figure 3.2/A) was fitted to a two-component model described in detail in the Methods section (2.5.1.2. FCS analysis of the cell measurement). The two-component model used in this study includes a 3D fast-moving component, representing the remaining free SNAP dye and the 2D model, indicating the slow-moving membrane-bound receptor. The fitted autocorrelation curve (Figure 3.2/B) was used to determine the average dwell times of the fluorescence species, which were represented by the mid-point of the sigmoid curve. The averaged diffusion coefficient (D_{FCS}) was calculated from the average dwell time of the receptor obtained from the AC curve (Equation 6 in the Method chapter). An offset (k) was introduced to accommodate the AC curve fitted with an asymptote of >1. This transposition in y can be due to the presence of global photobleaching caused by membrane movement or high immobile fraction [79]. The average offset was around 0.004 $\pm$ 0.002% of the amplitude, and if the value of the offset was > 5%, the reads were excluded. The particle number of the species was calculated by the fraction of the diffusion component multiplied by the total particle number, which is the inverse proportion of the intercept on the y-axis (G(0)). From the particle number (N) of the receptor the receptor density ($N/\mu m^2$) was calculated by Equation 7, described in the Method chapter in section 2.5.1.2.

FCS data were collected for basal, 1 μM It1t and 10 nM CXCL12 conditions with the same treatment protocol as described above for confocal imaging. In basal conditions, the diffusion coefficient of SNAP-CXCR4 was 0.287±0.011 $\mu m^2/s$, and receptor density was 230±10 $N/\mu m^2$ (n=37 cells from 10 individual experiments). The diffusion coefficient or receptor density did not significantly change upon addition of the agonist, CXCL12, compared to vehicle condition (253±15 $N/\mu m^2$; p=0.47 and 0.274±0.011 $\mu m^2/s$; p=0.73, respectively, n=31 cells from 6 individual experiments). Similarly, the addition of antagonist IT1t caused no significant changes compared to the basal condition with 260±18 $N/\mu m^2$ density (p=0.29) and 0.324±0.015 $\mu m^2/s$ (p=0.09) diffusion coefficient, n=31 cells from 6 individual experiments (Figure 3.2 /C and D).

The fluorescence fluctuations were further used for an alternative PCH analysis to gain information about the oligomeric state of the receptor. Through PCH analysis providing the average molecular brightness, it can be determined whether single (one-component) or several brightnesses (two-component) were present in the measured population [134]. In vehicle condition, 30 out of 31 cells (96.77%) fitted to a single-component PCH model, indicating one brightness species. However, 1 out of 31 cells (3.23%) required a second component due to deviation from the fit at the higher photon per bin end, implying the presence of a second brighter species (n=31 cells from 8 individual experiments). The single brightness (ε) component was 41.3 ± 3.5 kHz, and the brighter second component was 70.3 kHz (n=1). This indicates that under basal conditions, the SNAP-CXCR4 exist as a species of predominantly single brightness. In the case of the 1μM IT1t treatment (n=31 cells from 5 individual experiments), 2 cells out of 31 cells (6.45%) required two component PCH, which was similar to the vehicle condition. In the IT1t condition, the first component brightness was 39.3 ± 3.5 kHz (n=31) and the second component 72.7 ± 17.2 kHz (n=2). In contrast, following treatment with 10 nM CXCL12 for 10 minutes (n=32 cells from 6 individual experiments), the data showed an increased percentage of cells requiring a second component (11 cells out of 32 cells; 34.38%) compared to vehicle condition. The first component brightness in the CXCL12 condition was 33.1 ± 3.1 kHz (n=32), while the second PCH component was 164.0 ± 43.0 kHz (n=11), which was

not significantly brighter than the second component of the vehicle (Figure 3.2/E and F).

Table 3.1: Grouped data of FCS parameters for SNAP-CXCR4. *Membrane density (N), FCS diffusion coefficient (D_{FCS}), molecular brightness (ε) of component 1 (C1) and component 2 (C2) and the percentage of the cells clustering/have a second component based on PCH analysis. The condition of vehicle, 1 µM IT1t (30 mins) and 10 nM CXCL12 (10 mins) cells, n=31-38 cells from minimum of 6 individual experiments.*

Condition	FCS		PCH		
	D_{FCS} (µm²/s)	N (particles/µm²)	ε C1 (kHz)	ε C2 (kHz)	Second PCH component (% cells)
Vehicle	0.287±0.011	230±10	41.34±3.47	70.29	3.23
CXCL12	0.274±0.011	253±15	33.14±3.13	163.9±43.03	34.38
IT1t	0.324±0.015	260±18	39.26±3.53	72.67±17.23	6.45

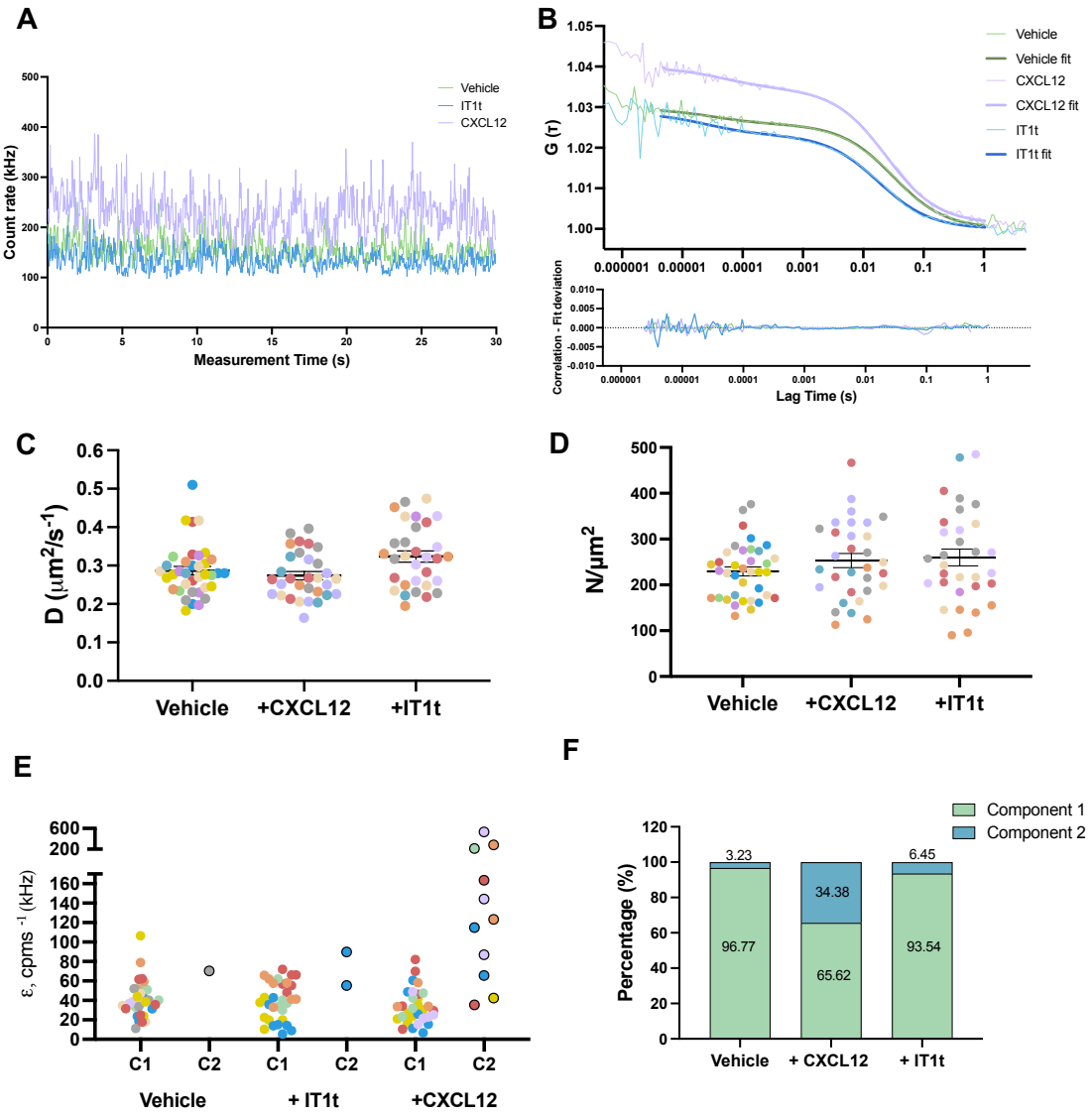

Figure 3.2: Dynamics and organisation of SNAP-CXCR4 within the plasma membrane measured by FCS. *HEK293G SNAP-CXCR4 cells were labelled with 100 nM SNAPsurface Alexa 488 and FCS measurements taken on the upper cell membrane following stimulation with vehicle, 1 μM It1t (30 mins, 37 °C) or 10 nM CXCL12 (10 mins, 37 °C) as in Methods.* ***A:*** *Representative raw fluorescence fluctuation traces for each condition.* ***B****: Representative autocorrelation curves and correlation-fit deviation in each condition.* ***C****: Diffusion coefficient of SNAP-CXCR4,* ***D:*** *Particle number of SNAP-CXCR4* ***E:*** *Molecular brightness of SNAP-CXCR4 for vehicle, CXCL12 and It1t condition. For all conditions, the brightness values show the first (1) and second (2) component fit, n=31-38 cells from minimum of 6 individual experiments.* ***E:*** *Percentage of the cells with first and second components. for n=31-38 cells from minimum of 6 individual experiments, one-way ANOVA followed by Dunnett's multiple comparisons test (non-significant). In C,D and E colours represents independent experimental repeats. Error bars = SEM.*

3.3.3. Optimisation of FRAP Parameters

To assess CXCR4 dynamics and organisation within the plasma membrane over a larger membrane area, Fluorescence Recovery After Photobleaching (FRAP) was used. FRAP measurements have been used previously to assess the dynamics and organisation of the μ-opioid receptor [84]; however, the parameters for FRAP measurement of CXCR4 required further optimisation before collecting the final data set. To do this, FRAP was performed on HEK G cells with stably expressed N-terminal SNAP-tagged CXCR4 receptors using a variety of imaging conditions. The SNAP-CXCR4 on the cell membrane was first labelled with SNAP Surface Alexa 488 (100 nM), a membrane impermeable SNAP dye. To record the FRAP data, the focus was placed on the basal membrane of the cells, and a 20-pixel diameter circular bleaching area was placed in a uniform area of fluorescence to measure the recovery of the fluorescence intensity over time.

The set-up used was one previously used by our lab [84] (Figure 3.3/A). The gain was set around 600, and the pinhole, whose purpose is to block out of focus light, was set to 1 Airy Unit (34 μm). The total measurement cycle was set to 120 cycles, including 5 cycles followed by 100 iterations of bleaching cycles of the circular bleaching area only (with 100% laser power). The representative fluorescent intensity data over time within the bleach area for these initial parameters with single-time images before bleach (first cycle) and after recovery (last cycle) are presented in Figure 3.3. The representative FRAP curve showed that upon bleaching, the fluorescence intensity dropped to around 0, which indicates correct bleaching parameters. However, after bleaching, the fluorescence intensity stayed lower than 15, which indicates the risk of a poor signal-to-noise ratio and lack of recovery. This might be caused by low initial intensity or movement. To correct this, the gain was increased to ~ 800 in the second set-up, which resulted in higher fluorescence intensity and better signal/noise ratio (Figure 3.3/B). However, the rapid increase in the intensity around 80 seconds (shown in the raw data curve red circle in Figure 3.3/B), suggests focal drift. In case of cell movement, the membrane can move out of the focal plane and potentially skew the FRAP recovery curve. To

overcome this, the pinhole was increased to 1.5 AU in the third set up, which allows some movement while keeping the membrane in the focal plane (Figure 3.3/C). As the representative FRAP curve shows, the recovery of fluorescence intensity presented a plateau with appropriate intensity; however, after ~80 seconds (marked with a red circle), this plateau decreased due to visible focal plane movement towards the cell cytosol (Figure 3.3/C image of last cycle). As the recovery plateau was present before ~80 seconds, the total cycle was decreased to 60 cycles with 50 bleaching cycles for the last set-up (Figure 3.3/D). This set up resulted in a FRAP curve with plateaued recovery in fluorescence recovery and minimal detected cell movement. For the final data set collection, the fourth set-up was used to assess the receptor dynamics and organisation.

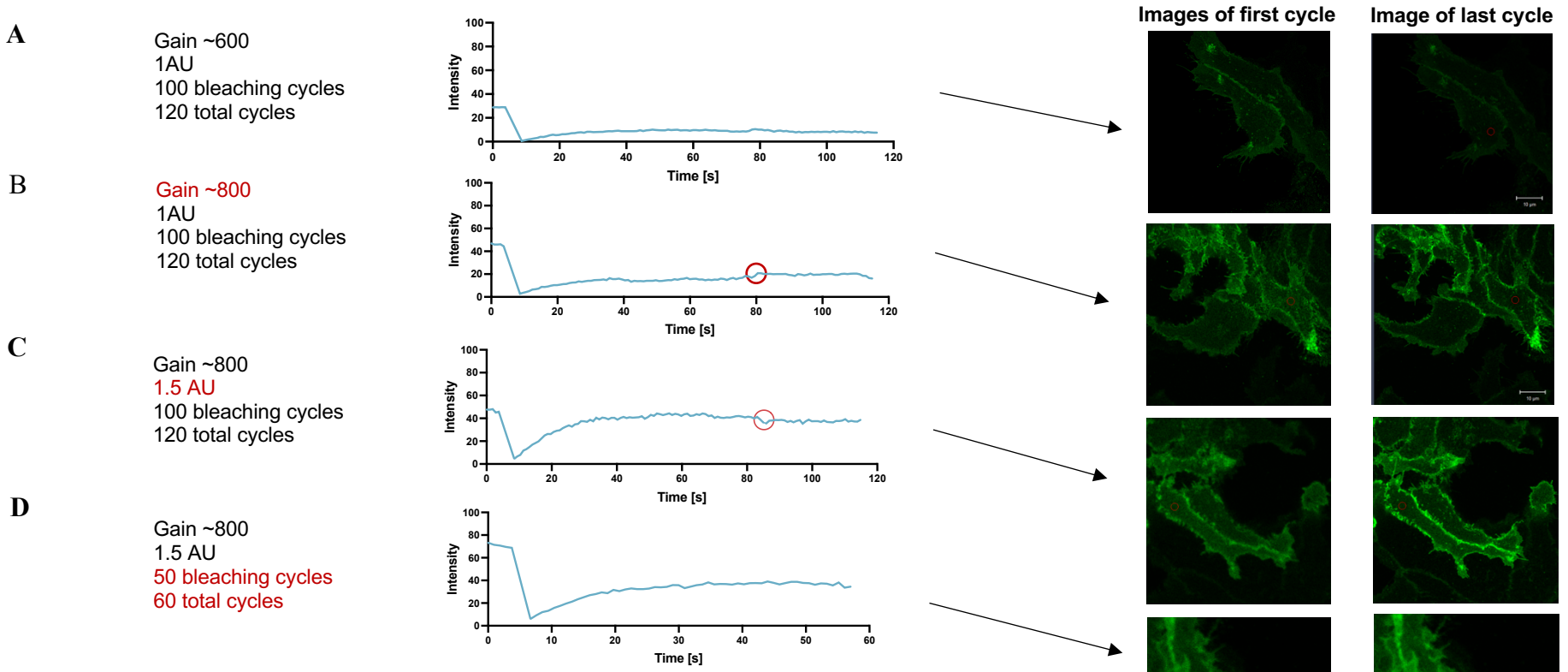

Figure 3.3: Optimisation of FRAP parameters in HEK293 G SNAP-CXCR4 cells. *Cells were labelled with SNAPSurface AlexaFluor488 as indicated in Methods and imaged on a Zess LSM880 microscope using a 40x c-Apochromat objective and a Zoom of 3x, as described, using a circular FRAP bleach area of 20 pixels. Each panel shows a FRAP recovery curve (left) and a confocal slice pre-bleach (centre) at the end of recovery (right).*
(A) Initial parameters using gain~600, 1AU pinhole, 100 bleaching cycles (B) gain increased ~ 800 (C) pinhole increased to 1.5AU (D) Bleaching cycles reduced to 50 with total cycles of 60. Data shown are representative examples from 3 independent experiments.

3.3.4. Plasma Membrane Organisation and Dynamics of CXCR4 – FRAP Studies

FRAP was used to provide data about the mobility of the CXCR4 receptor at the membrane over a larger scale than FCS. In addition, FRAP can provide information about the immobile fraction of the receptor, information which is missing from the FCS and PCH analysis. The 20-pixel diameter (5.89 μm^2) bleaching area was chosen, and this area was bleached after 5 scans and fluorescence recovery was measured over time (Figure 3.4/A). Following the measurement, a reference cell area and a background area were chosen for bleach correction, and the fluorescence recovery curve was fitted with a 2D model to determine the immobile fraction and half time of recovery. The diffusion coefficient (D_{FRAP}) of CXCR4, calculated from the half time recovery (described in 2.5.3) under basal condition was 0.054 ± 0.002 $\mu m^2/s$, which was slower that D_{FCS} of CXCR4 described earlier. The immobile proportion of the vehicle cells was 40.0 ± 1.6 % (n=38, 6 individual experiments).

As FCS measurements indicated no significant effect on receptor diffusion upon ligand addition, but an agonist mediated clustering, FRAP experiments were carried out under the same conditions to determine any effect on diffusion over larger scale or on immobile receptors, which would not be detected by FCS. The addition of CXCL12 and IT1t did not induce any significant difference in diffusion coefficients (D_{FRAP}) compared to the vehicle condition, with the value being 0.051 ± 0.002 $\mu m^2/s$ for CXCL12 (n=32, 5 individual experiments) and 0.060 ± 0.003 $\mu m^2/s$ for IT1t (n=32, 5 individual experiments) (Figure 3.4/B). Interestingly, significant changes were observed when monitoring the immobile fraction of receptors upon each condition (Figure 3.4/C). After IT1t treatment, the immobile fraction was significantly increased to 52.3 ± 2.2 % (n=32, 5 individual experiments). Activation of the receptors with agonist CXCL12 also showed a significant elevation of immobile fraction to 56.8 ± 2.2 % (n=32, 5 individual experiments).

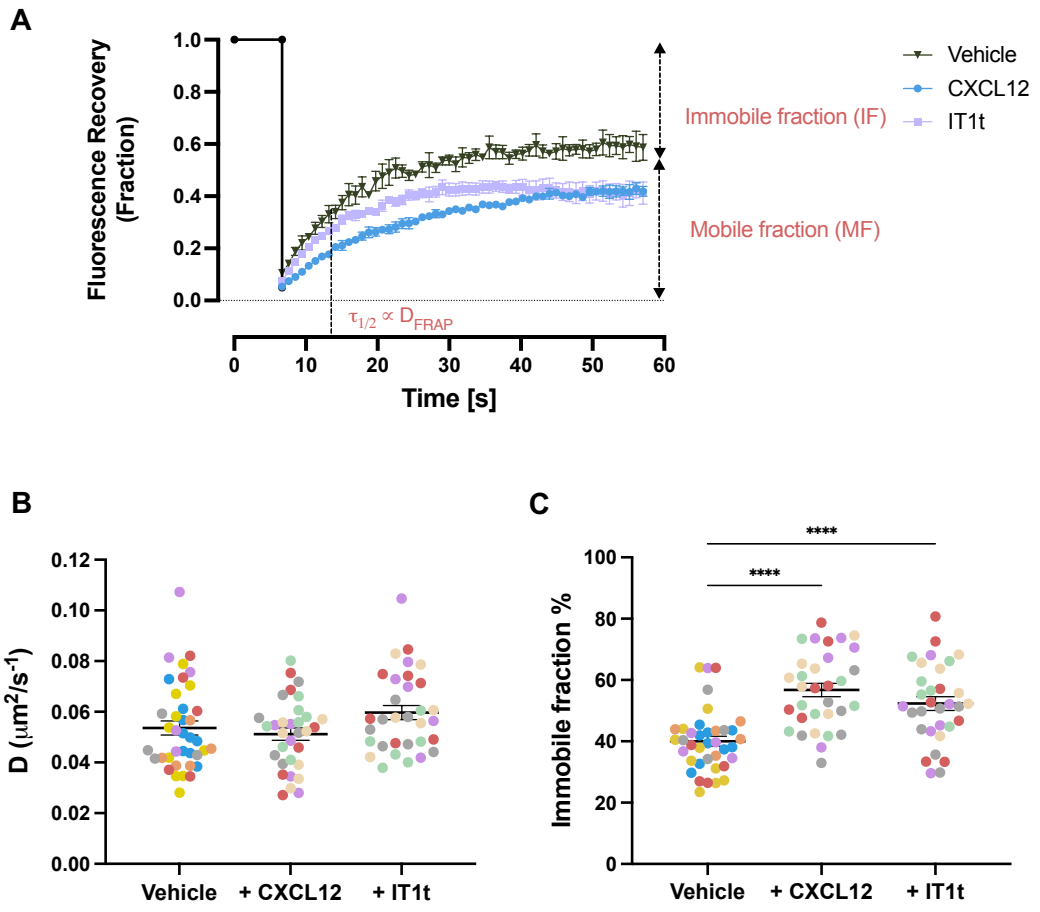

Figure 3.4: Dynamics and organisation of SNAP-CXCR4 within the plasma membrane measured with fluorescence recovery after photobleaching (FRAP). *HEK293G SNAP-CXCR4 cells were labelled with 100 nM SNAPsurface Alexa 488 and FCS measurements taken on the upper cell membrane following stimulation with vehicle, 1 μM It1t (30 mins, 37 °C) or 10 nM CXCL12 (10 mins, 37 °C) as in Methods* ***A:*** *Representative recovery curve over time using data from 3 cells per condition, providing the half recovery time and the mobile and immobile fraction for each conditions* ***B:*** *Diffusion coefficient (D_{FRAP}) of SNAP-CXCR4* ***C:*** *Immobile fraction of SNAP-CXCR4 significant increase ($p<0.0001$) in +10 nM CXCL12 and +1 μM It1t condition compared to vehicle (n=32-38 cells from a minimum of 6 individual experiments, one-way ANOVA followed by Dunnett's multiple comparisons test, ns, **** $p<0.0001$). In B and C, colours represent independent experimental repeats. Error bars = SEM.*

Table 3.2: Grouped data of FRAP parameters for SNAP-CXCR4. *FRAP diffusion coefficient (D_{FRAP}) and immobile fraction (IF). The condition of vehicle, 1 μM IT1t (30 mins) and 10 nM CXCL12 (10 mins) cells, n=32-38 from a minimum of 6 individual experiments (one-way ANOVA followed by Dunnett's multiple comparisons test, ns, **** p<0.0001).*

Condition	FRAP		
	D_{FRAP} (μm²/s)	Immobile fraction (%)	
Vehicle	0.054±0.003	40.0±1.6	
CXCL12	0.051±0.002	56.8±2.2	****
IT1t	0.060±0.003	52.3±2.2	****

3.3.5. Relationship Between Bleaching Area Size and FRAP Diffusion Coefficient

In the FRAP data presented above, we did not observe a significant change in CXCR4 diffusion upon ligand stimulation, but we showed an increased immobile fraction. We were curious whether modifying the diameter of the bleaching area towards a smaller or larger scale of detection would provide a different outcome. To investigate this, FRAP measurements were carried out using bleaching areas of different diameters. We hypothesised that changes in the size of the FRAP area could also provide information about the receptor membrane dynamics in a wider membrane surface range between the nano to micro range. The circular bleaching areas were between 5-40 pixel in diameter (0.37-23.49 μm^2). The basal diffusion coefficient presented an increase from 5 to 40-pixel diameter with 5-pixel diameter: 0.0095 ± 0.0007 $\mu m^2/s$; 10-pixel diameter: 0.024 ± 0.002 $\mu m^2/s$; 20-pixel diameter: 0.053 ± 0.003 $\mu m^2/s$; 30-pixel diameter: 0.102 ± 0.004 $\mu m^2/s$ and 40-pixel diameter: 0.147 ± 0.004 $\mu m^2/s$ (Figure 3.5/B). The immobile fraction was between 26-50% through the measured area with a 5-pixel diameter value of 26.2 ± 3.3%, 10-pixel diameter of 36.7 ± 3.2%, 20-pixel diameter of 38.5 ± 2.9%, 30-pixel diameter 43 ± 2.7%, 40-pixel diameter 49.6 ± 1.7% (n=19-23 cells from a minimum of 6 individual experiments; Figure 3.5/C). Compared to the basal dynamics the CXCL12 stimulation resulted in a similar diffusion coefficient in case of 5-,10-, and 20-pixel diameter areas (5x5: 0.0096 ± 0.0006 $\mu m^2/s$, 10x10: 0.020 ± 0.002 $\mu m^2/s$, 20x20: 0.051 ± 0.004 $\mu m^2/s$) but showed a significant increase at 30x30 (0.083 ± 0.005 $\mu m^2/s$), and 40-pixel diameter areas with the diffusion coefficient of 0.128 ± 0.007 $\mu m^2/s$ (n=13-16 from minimum of 5 individual experiments, one-way ANOVA followed by Sidak's multiple comparisons test). The immobile fraction presented a slight but not significant elevation in the 10x10 pixel condition (45.7 ± 5.7%), and the 40x40 pixel condition (56.8 ± 3.0%). The CXCL12 treatment resulted in a significant increase in immobile fraction for the 5-pixel diameter condition with 44.1 ± 3.6%, the 20-pixel diameter with 51.9 ± 3.3% and the 30-pixel diameter condition with 58.4 ± 4.0% (one-way ANOVA followed by Sidak's multiple comparisons test).

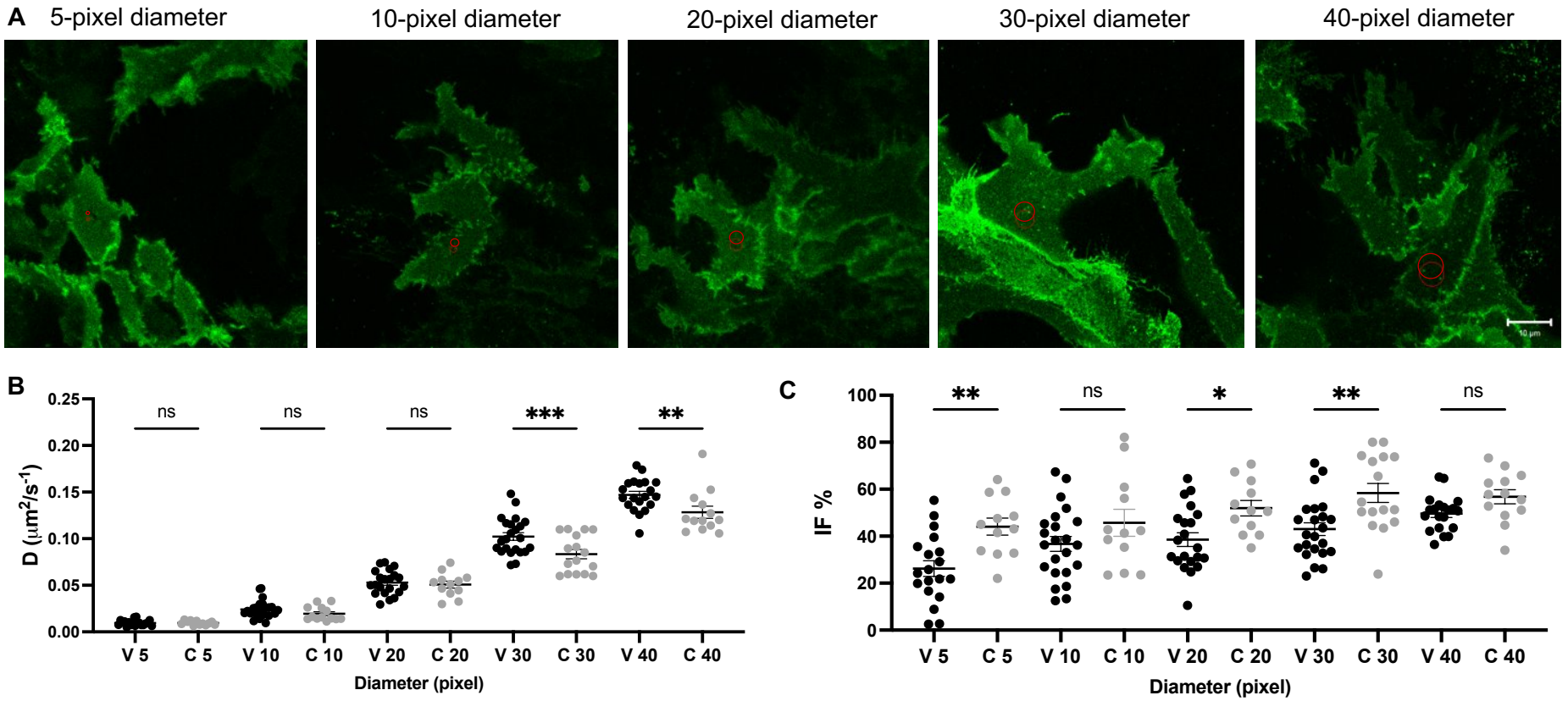

Figure 3.5: SNAP-CXCR4 FRAP dynamics with different diameter bleaching areas. *Bleach area diameters were changed between 5-40-pixels. Data was collected with basal and 10 nM CXCL12 conditions.* ***A:*** *The representative images are for each pixel diameter placed on the basal membrane of HEK G SNAP-CXCR4. Scale bar = 10 μm.* ***B:*** *Diffusion coefficient of SNAP-CXCR4* ***C:*** *Immobile fraction of SNAP-CXCR4, n=12-23 cells from minimum of 4 individual experiments, one-way ANOVA followed by Sidak's multiple comparisons test (ns (not significant),* p<0.05, **p<0.01, ***<0.001). On the graphs, V indicates vehicle condition, and C indicates CXCL12 condition. The numbers reference the diameter size of the bleaching area in pixels.*

3.4. Discussion

In this chapter, we collected information about the membrane organisation of the CXCR4 receptor and the impact of ligand stimulation on these membrane dynamics. We used confocal imaging, FCS and FRAP measurements with HEK G SNAP-CXCR4 cells in basal, CXCL12- and IT1t-stimulated conditions to assess the receptor dynamics at the membrane both on the nano and micro scale. Our data showed no significant change in the diffusion coefficient upon ligand stimulation; however, our results showed an increased immobile fraction of receptors upon incubation with CXCL12 and It1t.

To assess receptor distribution, the SNAP-CXCR4 receptor was labelled with SNAP Surface Alexa 488, an impermeable dye. This means that internalised fluorescent receptor that is detected will have been actively internalised post-labelling due to ligand stimulation or constitutive internalisation. Confocal images presented mainly membrane localisation of the CXCR4 receptor in a basal condition, which aligned with previous observations [132]. Upon activation with agonist CXCL12, a change in receptor localisation was detected. The receptor was partly internalised into bright vesicles while some proportion of the receptor remained membrane localised. The receptors remaining on the membrane are due to the short treatment time and the sub-maximal dose of CXCL12 [135], which is required for FCS membrane reads. Following the antagonist IT1t treatment, no internalisation was observed, and the receptor remained at the membrane. This finding is consistent with previous data from White and Caspar et al., where they found a concentration-dependent increase in luminescence upon IT1t addition in their CXCR4 internalisation assay, suggesting an increased cell surface expression of CXCR4 [135].

As mentioned before, previous studies described the importance of spatial dynamics and the oligomeric state of CXCR4 [107, 111], FCS and FRAP techniques were used to acquire further insight into the diffusion and stochiometric order of the CXCR4 receptor at the plasma membrane. Fluorescence correlation spectroscopy provided information about the

diffusion coefficient at the nanoscale, with the detection volume around 0.2 Fl and the area around 0.09 μm^2. With FCS, it is possible to assess fluorescently tagged receptor organisation and dynamics at the plasma membrane [77]. As described before, this approach has been used previously to study various GPCRs and the effect of their ligands [80, 122]. The detection of the cell membrane with the HEK G SNAP-CXCR4 was easy due to the location of the receptor, which is mainly at the cell membrane. The collected raw fluorescence fluctuation curves were fitted well to the two-component autocorrelation curve using a mix of a 3D and 2D diffusion model (Figure 3.2/B). The fast-moving 3D component represented the free SNAP Surface Alexa 488 dye, which was present in a small fraction, similar to findings with other SNAP-tagged GPCRs [79, 84]. The 2D model represented the membrane-bound CXCR4 receptor. Under basal conditions, the CXCR4 diffusion coefficient presented a slightly quicker diffusion value (0.287±0.011 $\mu m^2/s$) than it was observed in previous studies for other Class A GPCRs with FCS (NPY Y1, ~0.222 $\mu m^2/s$ [76]; A3AR, ~0.105 $\mu m^2/s$ [136]; β2AR, ~0.110 $\mu m^2/s$ [79]), however it is within the previously described GPCR diffusion speed range of 0.1 to 1 $\mu m^2/s$ [77]. This difference can come from the heterogenous structure of the local membrane as FCS is measured in a small membrane region, and interaction with the cytoskeleton or lipid raft can alter the diffusion of the measured receptor population [137]. The density of the receptor was 230±10 $N/\mu m^2$ in a basal condition, which is on the higher end of the physiological range for CXCR4 expression in blood cells [133]. This density is due to using a HEK G cell line that is stably overexpressing SNAP-CXCR4. The treatment conditions with 1 μM IT1t and 10 nM CXCL12 presented no significant changes in receptor diffusion (D_{FCS}). However, the CXCL12 showed a non-significant but slight slowing. The receptor density (N) of CXCL12 and IT1t compared to the vehicle showed no significant changes. All the FCS parameters suggested that there are no ligand-specific changes in membrane dynamics on the nano-scale level. Some previous studies with other GPCRs such as Neuropeptide Y receptor NPY2 [81] and adenosine receptor A3AR [136] also presented a lack of ligand effect on receptor diffusion at the plasma membrane.

The oligomeric state of the receptor was examined via PCH analysis. This alternative analysis of the fluctuation traces resolves the average molecular brightness of the receptor population. Upon potential clustering of the receptor, the PCH analysis requires the addition of a second component due to a skewed fit on the high photon bin end. In this case, the average molecular brightness is increased, representing a brighter second component. A previous study of 5-HT_{2C} serotonin receptor provided evidence using monomer and dimer controls, that the 5-HT_{2C} receptors are dimeric at the plasma membrane and can be fitted into a one component PCH model, indicating that the receptor species are only present in one oligomeric state [138]. Of note, while PCH analysis is able to detect 2-fold or greater brightness change [77], in the absence of monomer and dimer controls, we cannot establish the precise stoichiometry of the receptor, but since we observed the presence of single or two component receptor populations, this would suggest the presence of different oligomeric states. The brightness profile of the cells under basal conditions showed cells majorly (96.77%) fitting the one component fit, which indicates a single type of receptor species. Following the IT1t addition, a similar brightness profile was observed, with 93.54% of the cells having one component. Isbilir et al showed that IT1t disrupts CXCR4 dimer formation, resulting in monomeric stoichiometry [133]. This finding may explain why this CXCR4 population predominantly fitted in one component. In contrast, cells treated with CXCL12 presented an increased percentage of cells (34.38%) with the second, brighter component. Component 2, compared to component 1, is almost 5-fold brighter, suggesting a big mass change and the formation of large receptor clusters while a smaller oligomeric state still present. This would agree with the increased clustering over time shown in a previous publication by Isbilir et al. [133].

As FCS limited to detect only mobile fluorescence species [125], the FRAP approach was used to gain a more detailed view of the receptor dynamics by collecting information about the immobile receptor fraction. For FRAP optimisation, the gain was increased to improve the signal-to-noise ratio; the pinhole was increased to 1.5 AU to prevent the membrane from moving out of the focal plane. The measuring time and bleaching cycle were reduced to

minimise the chance of membrane movement over time while still reaching a plateau in fluorescence recovery. Following optimisation, the immobile proportion and the diffusion coefficient of CXCR4 over a larger membrane area were studied in basal, CXCL12- and IT1t-stimulated conditions. The FRAP diffusion data presented a much slower diffusion coefficient than FCS. This change in the diffusion coefficient was also described in previous publications for other GPCRs [84]. This can be due to measuring over a larger membrane area where the heterogeneity of the membrane, such as the cytoskeleton and lipid rafts would have a bigger limiting effect in free receptor diffusion and restrict movements [139]. The ligand addition presented no significant changes in diffusion coefficient (D_{FRAP}). In another study with SNAP-MOR, a similar lack of ligand effect was shown in macro diffusion measured by FRAP [84]. The immobile fraction in both treatment conditions of CXCL12 and IT1t was significantly elevated compared to the vehicle condition. The elevated immobile fraction with CXCL12 activation was also observed in previous studies, where CXCL12 stimulation resulted in increased nanocluster formation [25] and lower mobile, hence elevated immobile CXCR4 function [132, 140]. Moreover, it has been observed before that CXCL12 can modify the dynamics of CXCR4 at the plasma membrane, resulting in accumulation in lipid rafts [141]. In a previous study with other GPCRs, the NPY Y1 receptor showed a slower diffusion rate upon ligand stimulation, which was suggested to be due to interaction with clathrin-coated pits before internalisation [81]. A previous study measured μ-opioid receptor (MOR) dynamics at the plasma membrane using FRAP found reduced receptor mobility upon agonist (DAMGO) addition, however showed no significant changes in the ‘’macro’’ diffusion of the receptor [84]. Their results are similar to the change we observed in CXCR4 macro dynamics upon CXCL12 stimulation. Based on these results, these macro-scale changes in receptor mobility might be due to receptor clustering into clathrin-coated pits prior to endocytosis, leading to receptor immobilisation.

During an additional follow-up experiment with different FRAP area sizes (0.37-23.49 μm^2), the immobile fraction and the diffusion coefficients were observed in the vehicle and CXCL12 conditions. While the direction of the

changes matched with all the bleaching area sizes, the measurement with the two largest areas showed a significant slowing down following CXCL12 addition. This suggests that the selection of bleaching area size with FRAP needs to be chosen carefully and while the direction of the changes are constant, the data significance needs to be interpreted carefully as it might vary in relation to the size of the observation area. In the basal conditions, the increase in the bleaching area unexpectedly resulted in a faster diffusion coefficient. The correlation between the increasing detection area and the faster receptor diffusion may be due to the larger detection areas encompassing more heterogeneous membrane compartments, where restricted receptor mobility could result in a portion of the slower-moving receptor population being classified as immobile. This may shift the apparent diffusion coefficient toward the faster-moving population [142]. Additionally, the increased detection area could influence the signal-to-noise ratio, which may be affecting the calculated diffusion coefficient.

In our study, we observed CXCR4 receptor dynamics at the plasma membrane using FCS and FRAP techniques. While we did not see significant changes in receptor diffusion, both nano (D_{FCS}) and micro (D_{FRAP}) diffusion coefficients presented a slight slowdown upon CXCL12 activation, which might suggest the formation of clusters and their accumulation in distinct domains, preceding endocytosis, which can be picked up as an increase in immobile receptor proportion. One of the limitations of our study is that FCS only measures mobile fluorescence species within a small detection volume, which might not reflect the whole membrane dynamics of the receptor due to membrane heterogeneity. To overcome this, we can collect complimentary data about macro diffusion values and the oligomeric state of the receptor over a large membrane area using raster image correlation spectroscopy (RICS) and number and brightness analysis (N&B). RICS can provide information about diffusion and receptor density in a similar fashion as FCS over a ~70 μm^2 area [85]. N&B reanalyses a region of interest (~12 μm^2 area) of the raw RICS image stack and provides information about the oligomeric state of the receptor based on the average species brightness and number of particles [100]. Prior to this project, Dr. Joelle Goulding collected RICS and N&B data

from the HEK G SNAP-CXCR4 used here for FCS and FRAP measurement. This unpublished RICS data presented a slightly slower diffusion speed of SNAP-CXCR4 (0.20 ± 0.02 $\mu m^2/s$) as seen in FCS (0.287±0.011 $\mu m^2/s$) and, upon ligand addition, presented no significant changes. The N&B presented no significant change in brightness; however, upon CXCL12 addition, the CXCR4 population became highly heterogeneous with visible bright objects suggesting receptor clustering. In the future, it will be advantageous to observe the membrane dynamics of CXCR4 at an endogenous expression level to evaluate results in a more physiological environment.

The limitation of this study is the use of overexpressed SNAP-CXCR4 in HEK293 cells, which may not fully capture endogenous receptor dynamics or the complexity of the cancer microenvironment. The overexpression system may not represent the physiological levels of CXCR4 expression, and the HEK293 cell environment may fail to replicate the in vivo conditions in which CXCR4 operates. Additionally, while our focus on membrane receptor dynamics using FCS, FRAP, and RICS provided valuable insights, it could be extended to explore receptor dynamics in distinct cellular compartments such as cytosol. Future studies should prioritise investigating receptor behaviour in cancer cells with endogenous expression levels to better elucidate their roles under physiological conditions.

3.5 Conclusion

In conclusion, upon CXCL12 addition, internalisation of the CXCR4 receptor and formation of bright intracellular vesicles were observed with confocal imaging. There were no significant changes in the diffusion coefficient and the receptor density at the plasma membrane upon agonist CXCL12 and antagonist IT1t stimulation when assessed using FCS. However, the addition of CXCL12 presented a higher percentage of the second brightness component in PCH analysis, indicating cluster formation and change in the receptor oligomeric state. The assessment of the CXCR4 receptor over a larger membrane area using FRAP revealed no significant changes in the diffusion coefficient, which suggests no ligand-induced changes in the CXCR4 dynamics at the plasma membrane on a micro-scale. However, following CXCL12 and IT1t addition, the immobile fraction increased, suggesting ligand-induced changes in receptor mobility. These data show how complementary information obtained between spectroscopic and imaging methods can be used to investigate the dynamics of GPCRs within limited regions of the plasma membrane.

Chapter 4: Plasma Membrane Organisation and Dynamics of ACKR3

4.1 Introduction

Elucidating spatial and temporal dynamics of GPCRs at the plasma membrane, as highlighted for CXCR4 in the previous chapter, could provide valuable information about their local regulation, organisation and signalling [77, 116, 118]. In Chapter 3, we assessed CXCR4 dynamics at the membrane, and our data indicated that upon CXCL12 activation, the receptor diffusion characteristics do not change. However, PCH analysis of these fluorescence fluctuation data did show an increased percentage of brighter second components upon CXCL12 addition and an increased immobile fraction using FRAP, both of which suggest cluster formation. CXCR4 shares the physiological ligand CXCL12 with atypical chemokine receptor 3 (ACKR3) [143]. Both CXCR4 and ACKR3 showed increased expression in multiple tumour types and tumour microenvironments [144, 145] and the CXCR4/ACKR3/CXCL12 signalling axis has been suggested to play a role in tumour angiogenesis, metastasis and growth [64]. In addition, a previous study showed crosstalk between CXCR4/ACKR3 and epidermal growth factor receptor (EGFR) in breast cancer cells, resulting in the convergence of their signalling and suggesting a role in tumour progression [146]. Although CXCR4 and ACKR3 share the CXCL12 ligand, their organisation and signalling differ significantly. In contrast to CXCR4, ACKR3 is not able to activate G proteins [147], although following ligand activation, it can be phosphorylated by GRKs and recruit β-arrestin1/2 [73, 147]. Moreover, ACKR3 is believed to function as a scavenging receptor, preventing desensitisation and degradation of CXCR4 via internalisation of CXCL12 [148, 149]. ACKR3 cellular organisation also differs from CXCR4. It has been shown that ACKR3 constitutively internalises and recycles back to the plasma membrane [72, 150]. Upon CXCL12 binding, ACRK3 rapidly internalises to early endosomes and traffics to recycling endosomes, before recycling to the cell membrane [73].

Whilst there is a growing amount of information about ACKR3 trafficking, the spatial dynamics and organisation of ACKR3 at the plasma membrane are still unknown. Advanced spectroscopy techniques, fluorescence correlation spectroscopy (FCS) and fluorescence recovery after photobleaching (FRAP)

applied previously in the case of CXCR4 (Chapter 3) are suitable tools for studying the membrane dynamics of ACKR3. The addition of another complementary spectroscopy method, raster image correlation spectroscopy (RICS), can provide more insight into receptor dynamics over a large area of the membrane. RICS (detailed in 1.4.4.) uses raster scanning confocal microscopy to measure the fluorescence intensity per pixel within a membrane area along the line of the scan in the lateral direction (x-axis) and in the vertical direction (y-axis) to generate an image. Depending on the speed of the fluorescent species (receptor), they might move across adjacent pixels during the beam movement time. The intensity of the pixels over time can be coupled with the time between adjacent pixels horizontally or vertically for autocorrelation analysis to determine the dwell time of the fluorescent species and its diffusion characteristics [85, 99, 151, 152]. RICS has been previously used to measure and compare lateral diffusion of toll-like receptor 2 (TLR2) and cluster of differentiation 14 (CD14) within the plasma membrane [153]. Furthermore, RICS has been utilised in combination with FRAP in GPCR study to assess the lateral diffusion and mobility changes of thyrotropin-releasing hormone receptor (TRH-R) upon membrane integrity disruption through cholesterol depletion [154]. From RICS, smaller regions of interest can be reanalysed for Number and Brightness (N&B) analysis to provide information about the oligomeric state of the fluorescent species. N&B can measure apparent average brightness, and an average number of molecules to provide details about the fluorescent species oligomerisation state [155, 156]. Previous studies applied N&B analysis to determine GPCR and tyrosine kinase family oligomerisation based on their brightness analysis [157, 158].

This chapter explores the dynamics and organisation of ACKR3 within the plasma membrane. Using confocal imaging, we collected information about the distribution of the ACKR3 receptor in basal and CXCL12-stimulated conditions. Moreover, we show that, whilst the lack of membrane localisation of ACKR3 requires substantial methodological adjustment, FCS, FRAP, and RICS techniques can provide valuable insight into the receptor dynamics at nano, micro, and macro scales under both basal and agonist-stimulated conditions.

4.2. Methods

The experimental protocols used in this chapter are described in detail in Chapter 2, General Methods. Here, the approaches and techniques used were confocal microscopy to assess receptor localisation, fluorescence correlation spectroscopy (FCS), fluorescence recovery after photobleaching (FRAP) and raster image correlation spectroscopy (RICS). The changes in some of these experimental protocols and further optimisation are detailed below.

4.2.1. Cell Culture

Human embryonic kidney 293 (HEK293) SNAP-ACKR3 stable cells received from Kylie Pan at InterAx Biotech. Passaging, freezing, thawing, and seeding the cells to 8-well coverslips are described in Chapter 2.1 Cell Culture.

4.2.2. Confocal Imaging

Cells were imaged with a Zeiss LSM 880 confocal microscope, as described in Chapter 2, General Methods. However, the SNAP labelling protocol was modified as described below.

4.2.2.1. SNAP Labelling at Different Temperatures

For live cell imaging purposes, impermeant SNAP-dye, SNAP-Surface Alexa Flour 488 (New England BioLabs Ltd., UK) was used to label the membrane receptor in cells plated in 8-well chambers. The receptor was SNAP-labelled at three different temperatures with different incubation times to find the optimal conditions where ACKR3 constitutive cycling was reduced and the membrane localised receptor increased for the FCS/FRAP experiments with ACKR3. Prior to labelling, the media was removed from the cells and cells were washed with 200 µl/well Hank's HBSS containing 5mM glucose. Then SNAP-Surface Alexa Flour 488 at 500 nM final concentration was added to the cells in HBSS/glucose buffer and incubated for either (1) 30 minutes at 37 °C; (2) 30 minutes at room temperature (RT 22±2 °C) or (3) 1 hour at 4±2 °C. After incubation, the cells were washed with 200 µl/well HBSS/glucose three times.

4.2.2.2. Ligand Addition

For imaging of ligand-stimulated receptor, the cells in specific wells were treated with ACKR3 agonist, CXCL12 for 10 minutes at 10 nM final concentration or pre-treated with VUF16840 inverse agonist for 2 hours (at 100 nM or 1 μM final concentration) at RT. The detailed ligand addition protocol is detailed in 2.3.3. Ligand addition.

4.2.3. Fluorescence Spectroscopy

Experiments were performed on a Zeiss LSM 880 confocal microscope, as described in Chapter 2, General Methods. However, some steps were modified in SNAP labelling and cell-based FCS measurements as described below.

4.2.3.1. SNAP labelling

Following optimisation of SNAP labelling with cell membrane impermeant SNAP-Surface Alexa Flour 488 at different temperatures as described in 4.2.2.1, we decided to record the final dataset for FCS, FRAP and RICS experiments with 100 nM SNAP labelling for 30 minutes at RT.

4.2.3.2. Cell-based FCS measurements

Following calibration, cell localisation and gain set-up as described in 2.4.4.1., and 2.4.4.2, the detection volume was positioned on the x and y axis over the cell cytosol by moving the stage (Figure 4.1/A). Following that, the z-position was modified manually so that the upper membrane of the cell was in focus. A z-scan with 0.25 μm steps for ± 2 μm was performed to define the peak of the intensity. The initial detection volume was placed ~1.5 μm above the peak intensity, (Figure 4.1/B). The z-scan data and z-scan curve were saved for every cell measurement. A short fluorescence fluctuations trace was recorded (~5 seconds), at the initial detection volume position, using 488 excitation at 0.1% laser power. Following that, the detection volume was lowered in 0.25 μm steps, and the short FCS reads were repeated in every step until the first trace showed fluctuation traces typical of a membrane read (Figure 4.1/C). The

raw data read of the fluctuation traces were saved and fitted to the associated AC curves (Figure 4.1/D). The FCS data and PCH data analysis were carried out as described in Chapter 2 in 2.5.1. and 2.5.2.

Prior to the final FCS data set with basal and 10 nM CXCL12 conditions. FCS measurements were taken with the same approaches as described above, following the different temperature SNAP labelling in basal conditions. In each labelling condition, fluorescence fluctuation traces were taken from a minimum of 13 cells per condition from a minimum of 3 individual experiment days.

The values for diffusion coefficient and receptor density were compared with one-way ANOVA followed by Tukey's multiple comparisons test performed if $P < 0.05$ (statically significant).

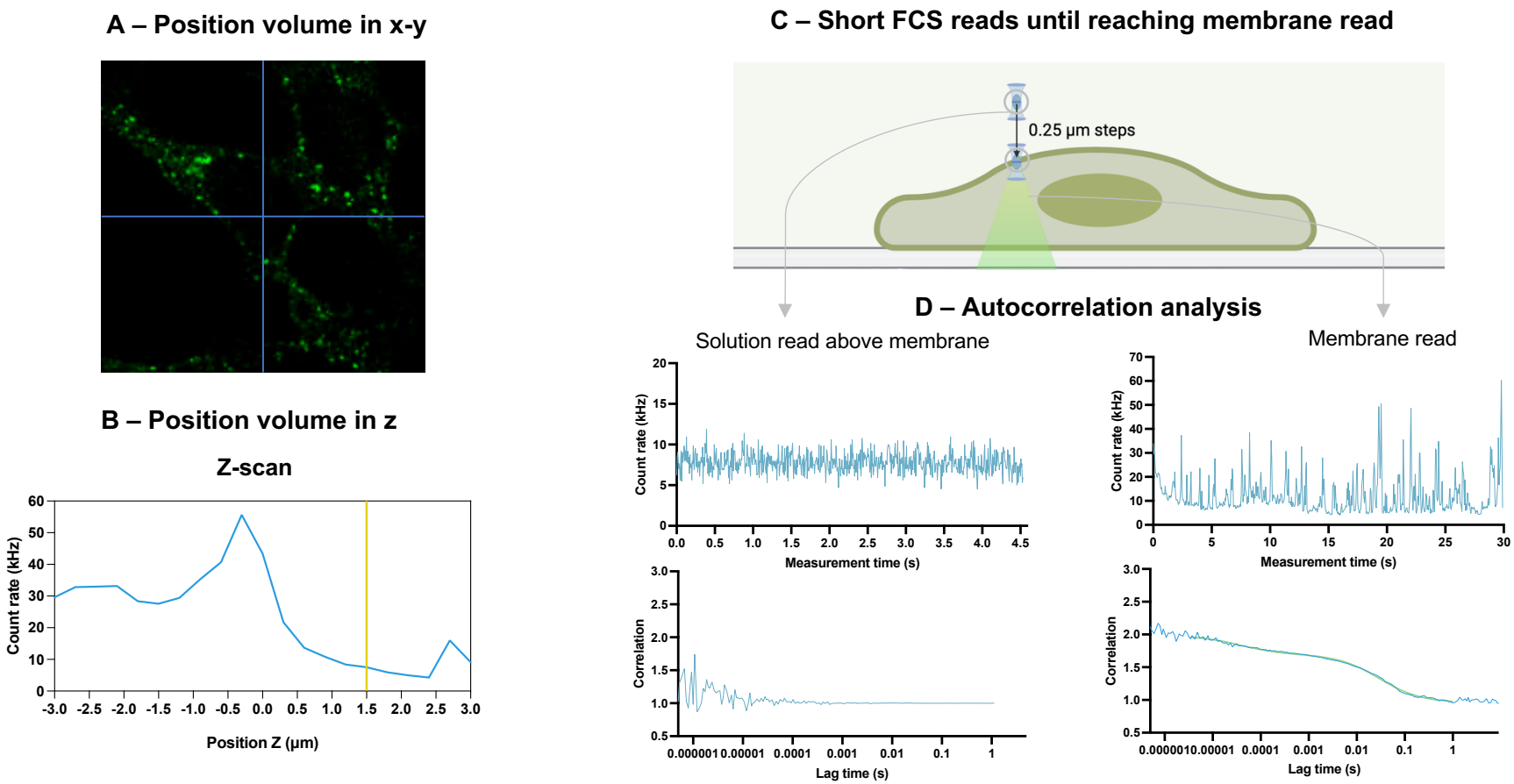

Figure 4.1: Cell-based FCS with HEK293 SNAP-ACKR3. A: *Position detection volume in x-y over cell cytosol.* ***B:*** *Position detection volume in z around 1.5 µm above the z-scan peak* ***C:*** *Taking short FCS reads and moving down the detection volume in the z-axis with 0.25 µm steps until reaching the membrane.* ***D:*** *Representative data for solution fluorescence fluctuation read and AC curve (left) and a membrane fluorescence fluctuation read and its AC fitting (right).*

4.3. Results

4.3.1. The Organisation of ACKR3 Upon Different SNAP Labelling Temperature

To study the organisation and dynamics of ACKR3, we used HEK293 cells stably expressing N-terminal SNAP-tagged ACKR3 (obtained from Kylie Pan at InterAx Biotech). ACKR3 is known to mostly localise in intracellular vesicles, posing a challenge to our spectroscopy approaches. However, unpublished data from InterAx Biotech lab using these HEK293 SNAP-ACKR3 cells presented an increased membrane location of ACKR3 after SNAP labelling at 4 °C. While this enhanced membrane labelling would be beneficial in measuring the dynamics of ACKR3 at the membrane, it is also important to ensure that the labelling process does not significantly affect the movement of ACKR3 within the cell surface. To determine the most optimal labelling condition for assessing the plasma membrane dynamics of ACKR3, we assessed ACKR3 location after SNAP labelling at different temperatures. For this optimisation step, the cells were SNAP-labelled with 100 nM membrane impermeable SNAP-Surface Alexa Flour 488 dye at three different temperatures and different incubation times (1 hour at 4 °C, 30 mins at RT and 30 mins at 37 °C). After the labelling steps, a 30-minute time series of the SNAP-ACKR3 cells were taken with a confocal microscope at 22±2 °C to determine receptor localisation and trafficking. Figure 4.2 shows ACKR3 localisation under basal conditions at the starting time point (0 minutes) and the end time point (30 minutes) for all three labelling conditions. Following the 4 °C SNAP labelling, the majority of the ACKR3 receptors were located on the plasma membrane. Over time however, the ACKR3 localisation changed and showed an increased intracellular location compared to time = 0s. After RT labelling, the SNAP-ACKR3 receptor is predominantly internalised in bright vesicles while still partially present at the plasma membrane. Following 37 °C SNAP labelling, ACKR3 localisation showed a similar, mainly intracellular, localisation, which is maintained over time. While 4 °C labelling presented the highest membrane location of ACKR3, to assess ACKR3 membrane dynamics

closer to physiological conditions but with a reduced risk of focal drift, we collected the final dataset following SNAP labelling at RT.

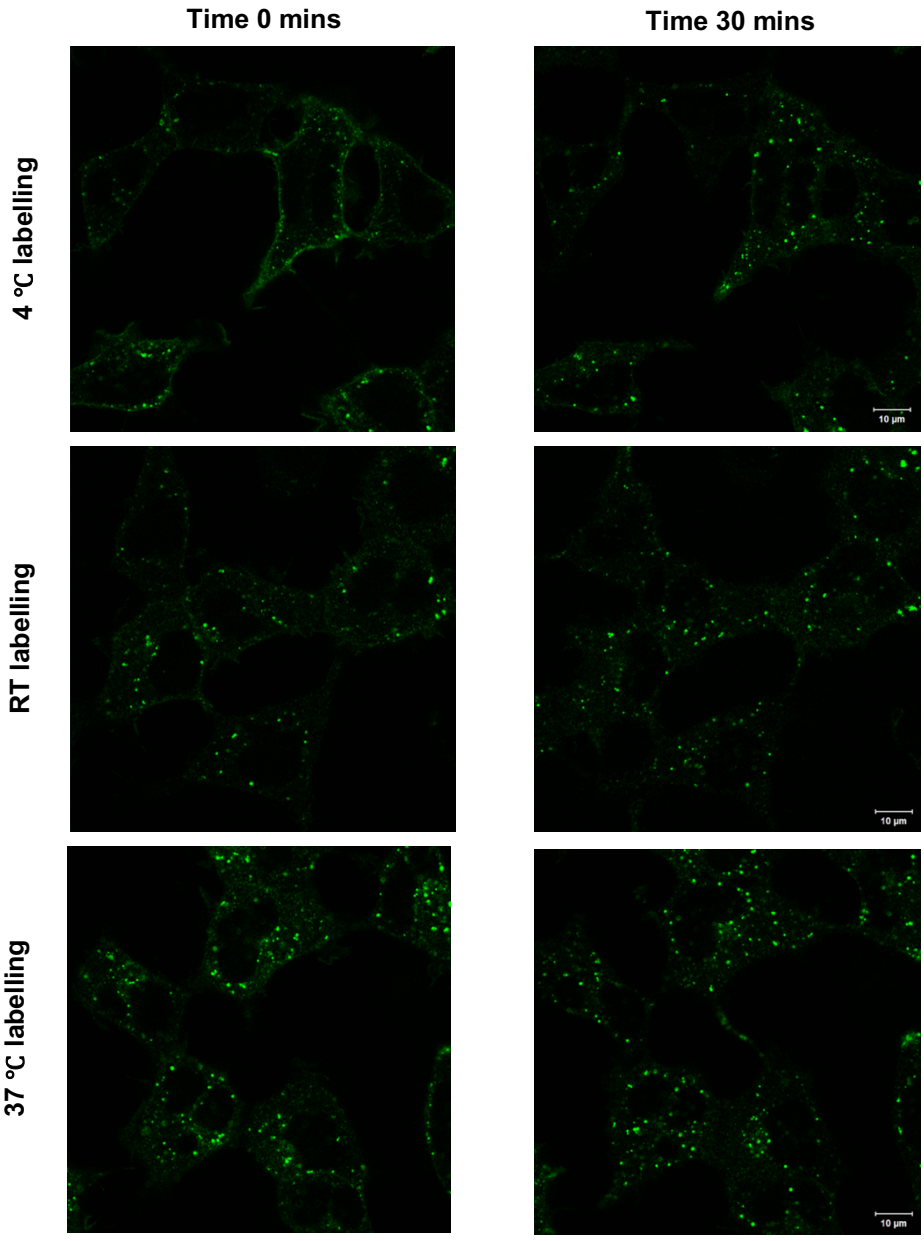

Figure 4.2: SNAP-ACKR3 localisation following different SNAP labelling temperatures. *Cells were labelled with SNAP-Surface Alexa Flour 488 in at three different temperatures as indicated in 4.2.2.1. and imaged on Zeiss LSM 880 microscope using 40x c-Apochromat water immersion objective 1.2 NA on zoom 3x. Each image was exported from time-course experiments at 0 and 30-minute time points. Scale bar = 10 µm.*

To determine the best conditions to study SNAP-ACKR3 dynamics at the plasma membrane without significantly altering ACKR3 dynamics, we used single-point FCS data collected from an undefined area of the upper cell

membrane. For the measurements, HEK293 SNAP-ACKR3 cells labelled at different temperatures were imaged live on the confocal microscope to find a suitable cell, then the detection volume was positioned over the cell cytosol on the x-y axis. For the selected cell, the z-position was set on the upper membrane by manually moving the stage. A z-scan was carried out to find the peak intensity which usually represents the upper membrane expressing the SNAP-labelled membrane-bound receptor. However, apart from membrane labelling, SNAP-ACKR3 presented an intracellular location in bright vesicles which can modify the peak intensity. For this reason, we introduced an additional step and placed the detection volume ~1.5 µm above the peak. Following that, the fluorescence fluctuation was recorded for a short amount of time (~4-8 seconds), and the detection volume was lowered in 0.25 µm steps until reaching the first trace showing fluctuations characteristic of a membrane read. After locating the membrane by short FCS reads, the fluorescence fluctuations were recorded for the usual 30 seconds (Figure 4.4/A) and were fitted to a two-component model representing the 3D fast-moving free SNAP dye and the 2D slow-moving membrane-bound receptor (described in the Methods section 2.5.1.2.). The fitted autocorrelation curve (Figure 4.4/B) determined the average dwell time of the fluorescence species and the number of particles. The average dwell time was used to calculate the diffusion coefficient (D_{FCS}) of the receptor. From the particle number (N), the receptor density (N/μm^2) was calculated using Equation 7 described in 2.5.1.2.

FCS data were collected following three different SNAP labelling conditions (1 hour at 4 °C, 30 mins at RT and 30 mins at 37 °C) under unstimulated conditions. Following 4 °C SNAP labelling, the diffusion coefficient of SNAP-ACKR3 was 0.251±0.022 $\mu m^2/s$ (n=13 cells from 3 individual experiments). The diffusion coefficient of SNAP-ACKR3 did not change significantly after RT labelling (0.235±0.019 $\mu m^2/s$, n=13 cells from 3 individual experiments) or 37 °C labelling (0.180±0.024 $\mu m^2/s$, n=14 cells from 3 individual experiments). The receptor density after 4 °C SNAP labelling was (33±6 N/μm^2). The RT labelling presented a similar density (48±14 N/μm^2) while it significantly increased after 37 °C labelling (95±25 N/μm^2, p=0.0375). However, the density of SNAP-ACKR3 measured after 37 °C labelling showed a much greater

variability between cells, which, combined with the observation of focal drift during confocal time series, indicates challenges to keep the movement of the membrane within the detection volume. Based on these observations, we decided that room temperature labelling was the most suitable SNAP labelling condition to study SNAP-ACKR3 dynamics and organisation at the plasma membrane. Moreover, we confirmed that the different labelling temperatures do not affect ACKR3 receptor diffusion parameters.

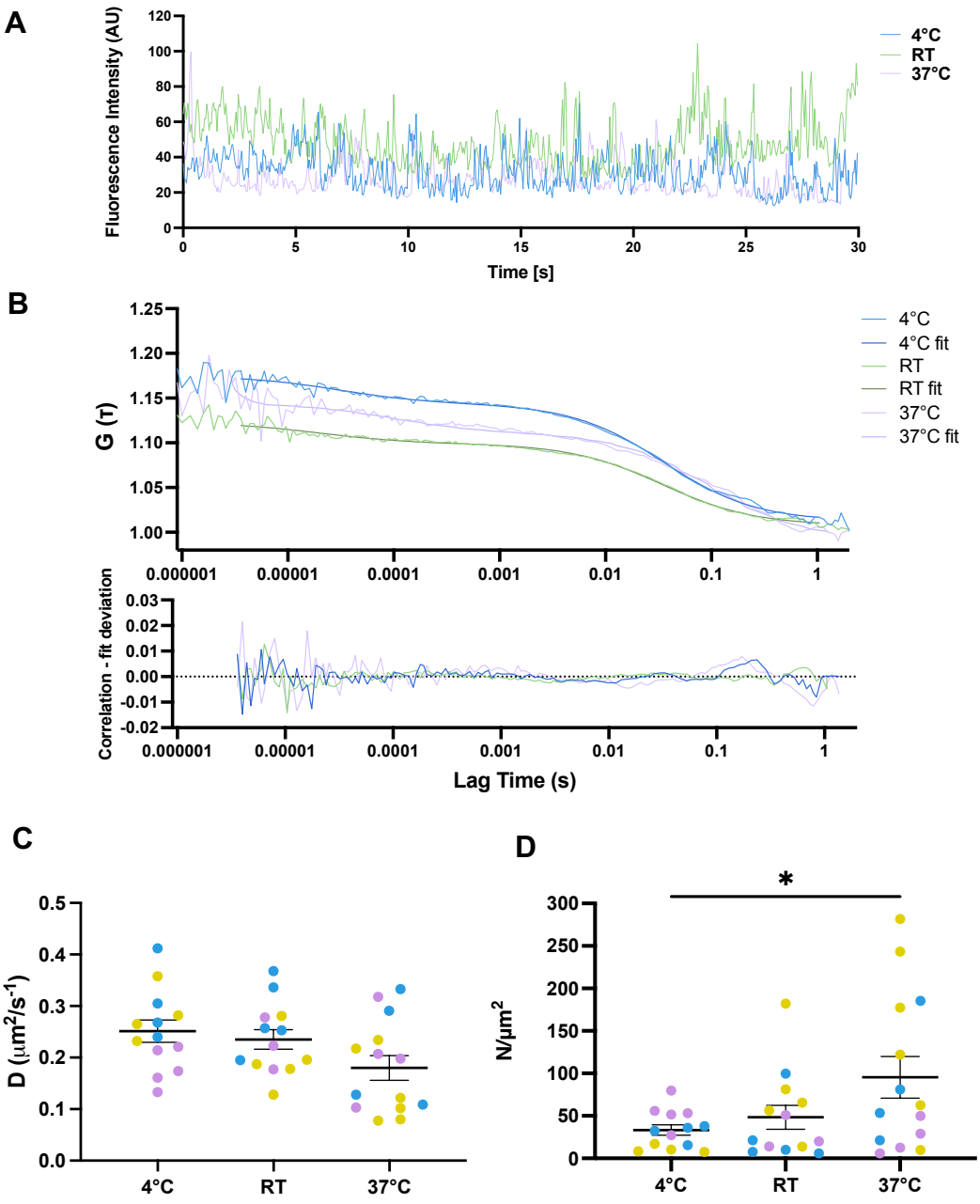

Figure 4.3: FCS measurements of SNAP-ACKR3 within the plasma membrane following SNAP labelling at different temperatures. *HEK293 SNAP-ACKR3 cells were labelled with 100 nM SNAPsurface Alexa 488 under different conditions (1 hour at 4 °C, 30 mins at RT and 30 mins at 37 °C) and FCS measurements were taken on the upper cell membrane as in Methods.* ***A:*** *Representative raw fluorescence fluctuation traces.* ***B****: Representative autocorrelation curves and correlation-fit deviation.* ***C****: Diffusion coefficient (D_{FCS}) of SNAP-ACKR3,* ***D:*** *Particle number of SNAP-ACKR3, n=13-14 cells from 3 individual experiments, one-way ANOVA followed by Turkey's multiple comparisons test (non-significant, *<0.05). In C and D, colours represent independent experimental repeats. Error bars = SEM.*

4.3.2. The Organisation of ACKR3 Under Basal and Stimulated Conditions

Following RT SNAP labelling detailed in the previous section, the cells were treated with either vehicle (HBSS) or 10 nM CXCL12 (ACKR3 agonist) for 10 minutes at RT and confocal images were taken to assess the ACKR3 location and the impact of CXCL12 stimulation on receptor distribution.

The left confocal image in Figure 4.3 shows that under basal conditions, SNAP-ACKR3 is predominantly localised intracellularly in bright vesicles, while a small portion of membrane-localised ACKR3 receptor is also detected. Following CXCL12 stimulation, the SNAP-ACKR3 receptor shows a similar distribution then the vehicle condition, with mainly intracellular localisation in bright vesicles. However, it is difficult to see whether the amount of membrane-localised receptor has changed.

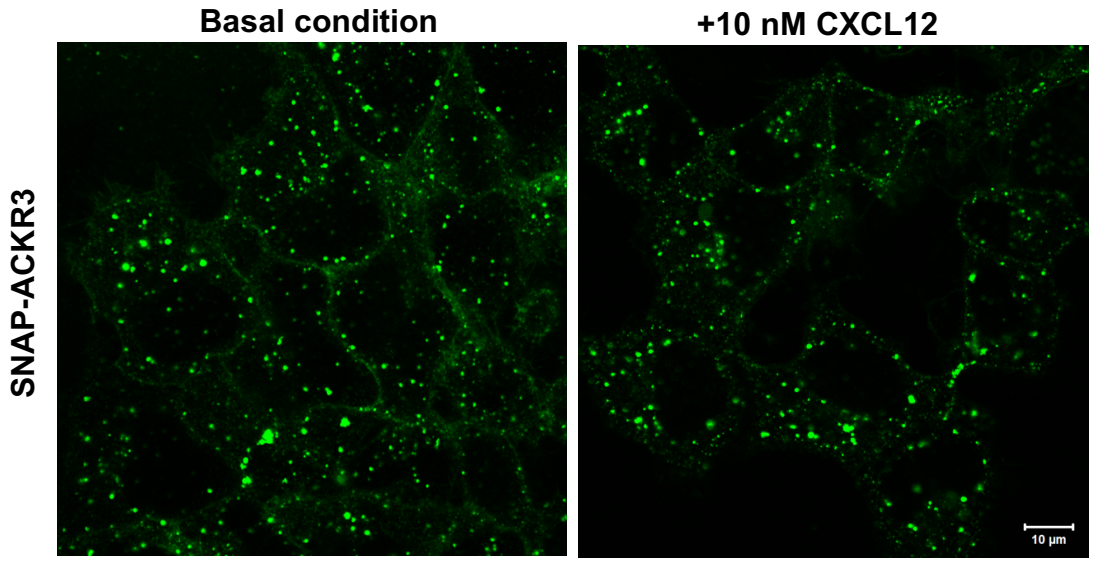

Figure 4.4: The localisation of SNAP-ACKR3 under basal and CXCL12-stimulated conditions. *Cells were labelled with SNAP-Surface Alexa Flour 488 as indicated in Chapter 4 Methods and imaged on Zeiss LSM 880 microscope using 40x c-Apochromat water immersion objective 1.2 NA on zoom 3x. Each image is a representative example from 3 independent experiments. Under basal conditions, the majority of the SNAP-labelled ACKR3 receptor localised intracellularly with a limited amount of receptor on the plasma surface. The addition of 10 nM CXCL12 (agonist) does not show changes in ACKR3 receptor distribution and localisation. Scale bar = 10 µm.*

4.3.3. Plasma Membrane Organisation and Dynamics of ACKR3 – FCS Studies

To study the effect of ligand CXCL12 on the dynamics and organisation of SNAP-ACKR3 within the plasma membrane, single point FCS was performed on an undefined area of the upper cell membrane. HEK293 SNAP-ACKR3 cells were SNAP labelled at RT for 30 minutes with 100 nM SNAP Surface Alexa 488. Following the labelling, FCS measurement was carried out as described above (4.2.3.2. Cell-based FCS measurements). An offset (k) was introduced when necessary to adjust the AC curve fit when the asymptote was >1. The average offset was around 0.090 ± 0.057% of the amplitude, and if the value of the offset was > 5%, the reads were excluded.

FCS data were collected for basal and 10 nM CXCL12 conditions with the same treatment protocol as described above for confocal imaging. In basal conditions, the diffusion coefficient of SNAP-ACKR3 was 0.200±0.011 $\mu m^2/s$, and receptor density was 124±20 $N/\mu m^2$ (n=32 cells from 8 individual experiments). Upon agonist CXCL12 stimulation, the diffusion of SNAP-ACKR3 showed a significant decrease compared to vehicle condition (0.126±0.012 $\mu m^2/s$; $p<0.001$). However, CXCL12 addition did not significantly affect receptor density compared to the basal condition (170±34 $N/\mu m^2$ ($p=0.29$) n=17 cells from 6 individual experiments) (Figure 4.5 /C and D).

The fluorescence fluctuations were reused for an alternative analysis using Photon Counting Histogram (PCH) to investigate the oligomeric state of the receptor. By applying PCH analysis to determine the average molecular brightness, it was possible to discern whether the measured population predominantly displayed a single (one-component) or multiple brightness states (two-component) [134]. In vehicle conditions, 19 out of 32 cells (59.38%) fitted to a single-component PCH model, indicating one brightness species. The remaining, 13 out of 32 cells (40.62%) required a second component due to deviation from the fit at higher photon per bin values, implying the presence of a second brighter species (n=32 cells from 8 individual experiments). The average single brightness (ε) component value was 13.4 ± 2.8 kHz, and the average brighter second component value was 32.3 ± 4.1 kHz. This suggests

that for just under half of the measured cells, a proportion of the ACKR3 receptors are in a higher oligomeric or clustered state in basal condition. The addition of 10 nM CXCL12 (n=17 cells from 6 individual experiments) did not significantly change the percentage of cells being in a higher oligomeric state, with 7 cells out of 17 cells requiring a second component (41.18%). The first component brightness in the CXCL12 condition was 6.1 ± 1.2 kHz, while the second PCH component was 43.4 ± 7.7 kHz. The brightness of this second component upon CXCL12 stimulation was not significantly brighter than the second component determined for the vehicle condition (Figure 4.5/E and F).

Table 4.1: Grouped data of FCS parameters for SNAP-ACKR3. *Membrane density (N), FCS diffusion coefficient (D_{FCS}), molecular brightness (ε) of component 1 (C1) and component 2 (C2) and the percentage of the cells clustering/have a second component based on PCH analysis. The condition of the vehicle and 10 nM CXCL12 (10 mins) cells, n=17-32 cells from a minimum of 6 individual experiments (Unpaired Student's t-test ,**** p<0.0001).*

Condition	FCS		PCH		
	D_{FCS} (μm²/s)	N (particles/μm²)	ε C1 (kHz)	ε C2 (kHz)	Second PCH component (% cells)
Vehicle	0.200±0.011	124±20	13.41±2.83	32.33±4.06	40.62
CXCL12	0.126±0.012 ****	170±34	6.08±1.22	43.41±7.71	41.18

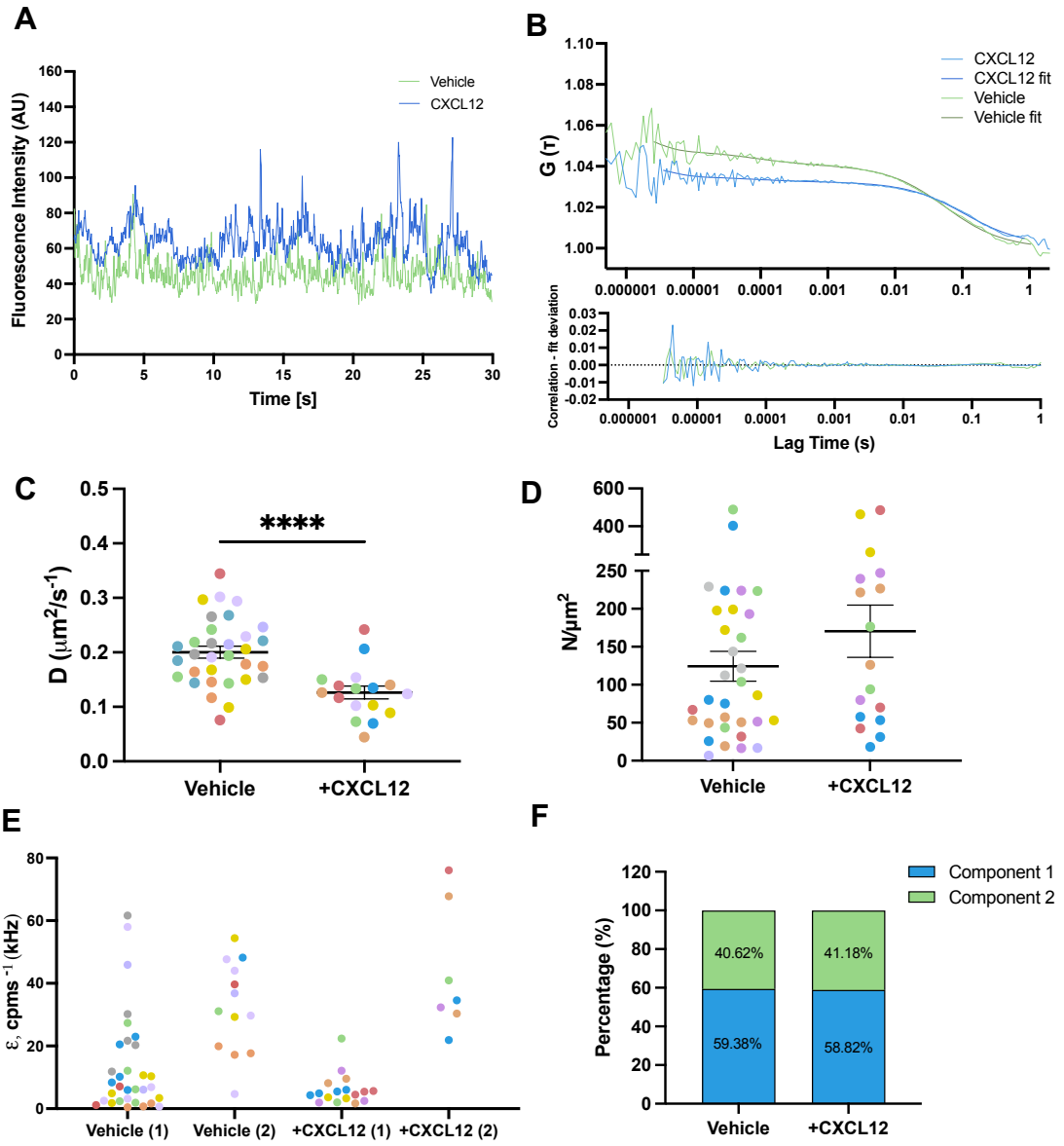

Figure 4.5: Dynamics and organisation of SNAP-ACKR3 within the plasma membrane measured by FCS. *HEK293 SNAP-ACKR3 cells were labelled with 100 nM SNAPsurface Alexa 488 and FCS measurements taken on the upper cell membrane following stimulation with vehicle or 10 nM CXCL12 (10 mins, RT) as in Methods.* ***A:*** *Representative raw fluorescence fluctuation traces for each condition.* ***B****: Representative autocorrelation curves and correlation-fit deviation in each condition.* ***C****: Diffusion coefficient of SNAP-ACKR3,* ***D:*** *Particle number of SNAP-ACKR3* ***E:*** *Molecular brightness of SNAP-ACKR3 for vehicle and CXCL12 condition. For all conditions, the brightness values show the first (1) and second (2) component fit, n=17-32 cells from minimum of 6 individual experiments.* ***E:*** *Percentage of the cells with first and second components. for n=17-32 cells from minimum of 6 individual experiments, unpaired Student's t-test (**** p<0.0001). In C, D and E colours represent independent experimental repeats. Error bars = SEM.*

4.3.4. Plasma Membrane Organisation and Dynamics of ACKR3 – FRAP Studies

To study ACKR3 dynamics and organisation within the plasma membrane over a larger membrane area, Fluorescence Recovery After Photobleaching (FRAP) was used. In addition to providing diffusion parameters over a larger area, FRAP, in contrast to FCS, is also able to provide information about the immobile fraction of the receptor. FRAP measurements have been optimised and used previously to assess the dynamics and organisation of the CXCR4 receptor in Chapter 3. As FRAP was recorded on the basal membrane, the membrane localisation was easier compared to FCS and did not require further optimisation for the assessment of ACKR3. Following SNAP labelling of HEK293 SNAP-ACKR3 cells with 100 nM SNAP Surface Alexa 488, FRAP measurements were recorded on the basal membrane of the cells, where a 20-pixel diameter circular bleaching area (5.89 μm^2) was set to record the recovery of fluorescence intensity over time after bleaching (Figure 4.6/A). For FRAP analysis, specific areas corresponding to a reference cell and background were chosen for bleaching correction. The fluorescence recovery curve was analysed using a 2D model to determine the immobile fraction and a half time of recovery which was then used to calculate the diffusion coefficient.

The diffusion coefficient (D_{FRAP}) of SNAP-ACKR3 under basal conditions was 0.060 ± 0.003 $\mu m^2/s$ (n=38 from 8 individual experiments), which was slower than D_{FCS} of ACKR3 described above. The immobile proportion of the ACKR3 was 46.5 ± 1.9 % (Figure 4.6/C). Following the diffusion change upon CXCL12 stimulation observed in FCS, FRAP data was collected under the same CXCL12 conditions (10 nM for 10 minutes incubation) to determine any effect of ligand in ACKR3 dynamics over a larger area and provide information on any changes in receptor mobility. Upon CXCL12 addition, the diffusion coefficient (D_{FRAP}) of ACKR3 was significantly reduced to 0.050±0.002 $\mu m^2/s$ ($p<0.01$; n=37 from 5 individual experiments; Figure 4.6/B). In addition, there was a significant increase in the immobile fraction of SNAP-ACKR3 upon

CXCL12 addition to 62.8 ± 1.8 % compared to basal conditions (p<0.0001; n=37, 5 individual experiments).

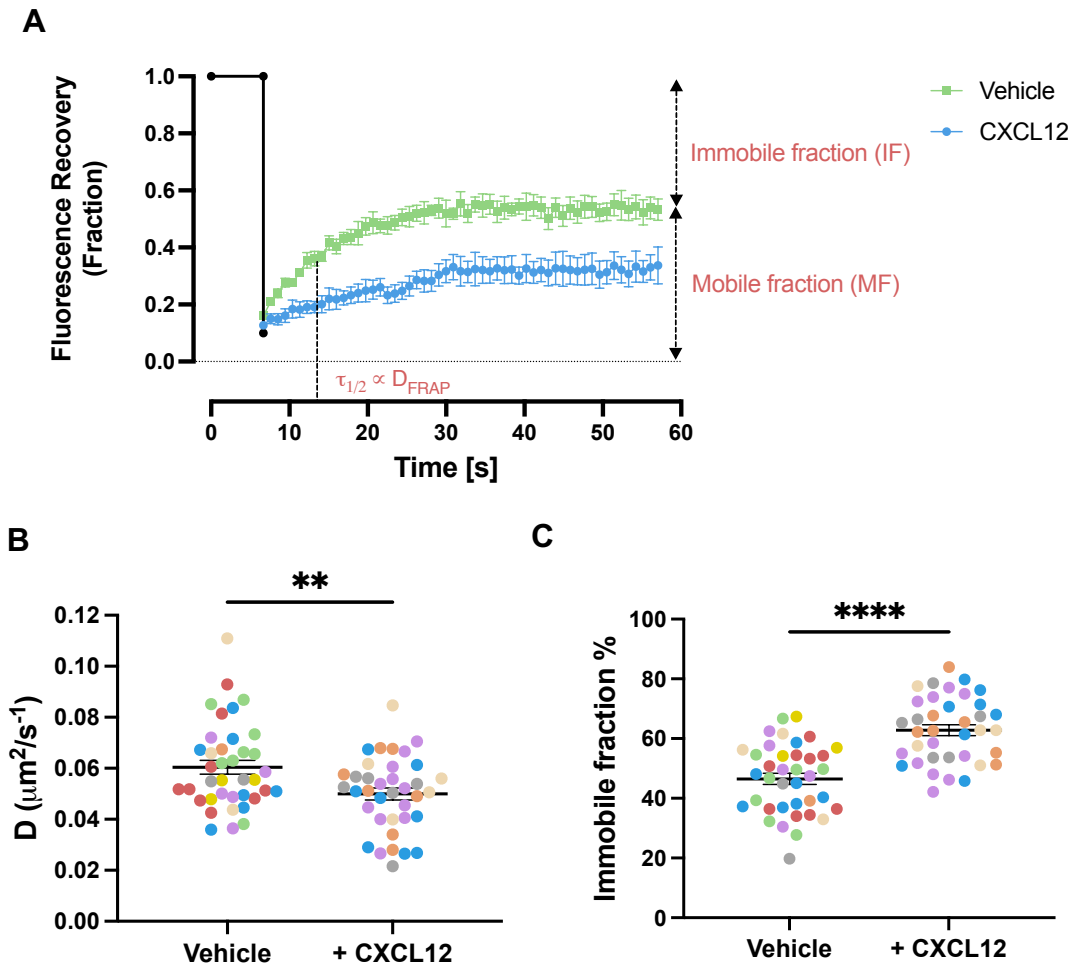

Figure 4.6: Dynamics and organisation of plasma membrane SNAP-ACKR3 measured with fluorescence recovery after photobleaching (FRAP). *HEK293 SNAP-ACKR3 cells were labelled with 100 nM SNAPsurface Alexa 488 and FRAP measurements taken on the basal cell membrane following stimulation with vehicle or 10 nM CXCL12 (10 mins, RT)* ***A:*** *Representative recovery curve over time using data from 3 cells per condition, providing the half recovery time and the mobile and immobile fraction* ***B:*** *Diffusion coefficient (D_{FRAP}) of SNAP-ACKR3 for Vehicle and 10 nM CXCL12* ***C:*** *Immobile fraction of SNAP-ACKR3 for Vehicle and 10 nM CXCL12. (n=37-38 cells from a minimum of 5 individual experiments, unpaired Student's t-test,** p<0.01, **** p<0.0001). In B and C, colours represent independent experimental repeats. Error bars = SEM.*

Table 4.2: Grouped data of FRAP parameters for SNAP-ACKR3. *FRAP diffusion coefficient (D_{FRAP}) and immobile fraction (IF) for cells treated with vehicle or 10 nM CXCL12 (10 mins) cells, n=37-38 from a minimum of 5 individual experiments, unpaired Student's t-test (** p<0.01, **** p<0.0001).*

Condition	FRAP	
	D_{FRAP} ($\mu m^2/s$)	Immobile fraction (%)
Vehicle	0.060±0.003	46.5±1.9
CXCL12	0.050±0.002 **	62.8±1.8 ****

4.3.5. Plasma Membrane Organisation and Dynamics of ACKR3 – RICS Studies

Raster image correlation spectroscopy (RICS) was used as an alternative approach to assess the SNAP-ACKR3 diffusion coefficient and receptor organisation over a large membrane area. RICS provides information about the dynamics of mobile fluorescent species, however, in contrast to FCS where we could use a two or multiple component diffusion model, RICS can only provide a single-component resolution and parameters. Following labelling of HEK293 SNAP-ACKR3 cells with 100 nM SNAP Surface Alexa 488 and calibration of the microscope (described in 2.4.4.1.), cells were localised, and the acquisition was switched to photon counting mode. Afterwards, the focus was manually set to the basal membrane (Figure 4.7/A left image), and the pixel size was set to 50 nm with the field of view being 256x256 pixels (164 μm^2) (Figure 4.7/A right image). A 100-scan cycle of this observation area was recorded in basal and CXCL12 (10 nM, 10 mins) conditions. Following this, autocorrelation curves were created to demonstrate correlated pixel-to-pixel movement along the direction of the raster (x-axis) and between raster lines (y-axis). These correlation curves were then fitted into a 2D single-component diffusion model to extract information about the SNAP-tagged membrane-bound receptor. The diffusion coefficient (D_{RICS}) was then calculated from this model. The overall diffusion coefficient of SNAP-ACKR3 in basal condition was 0.209 ± 0.017 $\mu m^2/s$ (n=30 from 10 individual experiments). Upon CXCL12 stimulation, the diffusion coefficient did not change significantly with a value of 0.195 ± 0.016 $\mu m^2/s$ (n=20 from 5 individual experiments, p=0.57, unpaired Student's t-test; Figure 4.7/B). The average amplitude of SNAP-ACKR3 which provides information about the number of particles and the receptor density, was 43±10 under basal condition (n=30 from 10 individual experiments) and was not significantly altered upon CXCL12 addition (25±4, p=0.12 with unpaired Student's t-test, n=20-30 from a minimum of 5 experiments). It is important to note that the average amplitude (N) in RICS cannot be directly compared to our FCS density data (N) as it is not converted to $N/\mu m^2$.

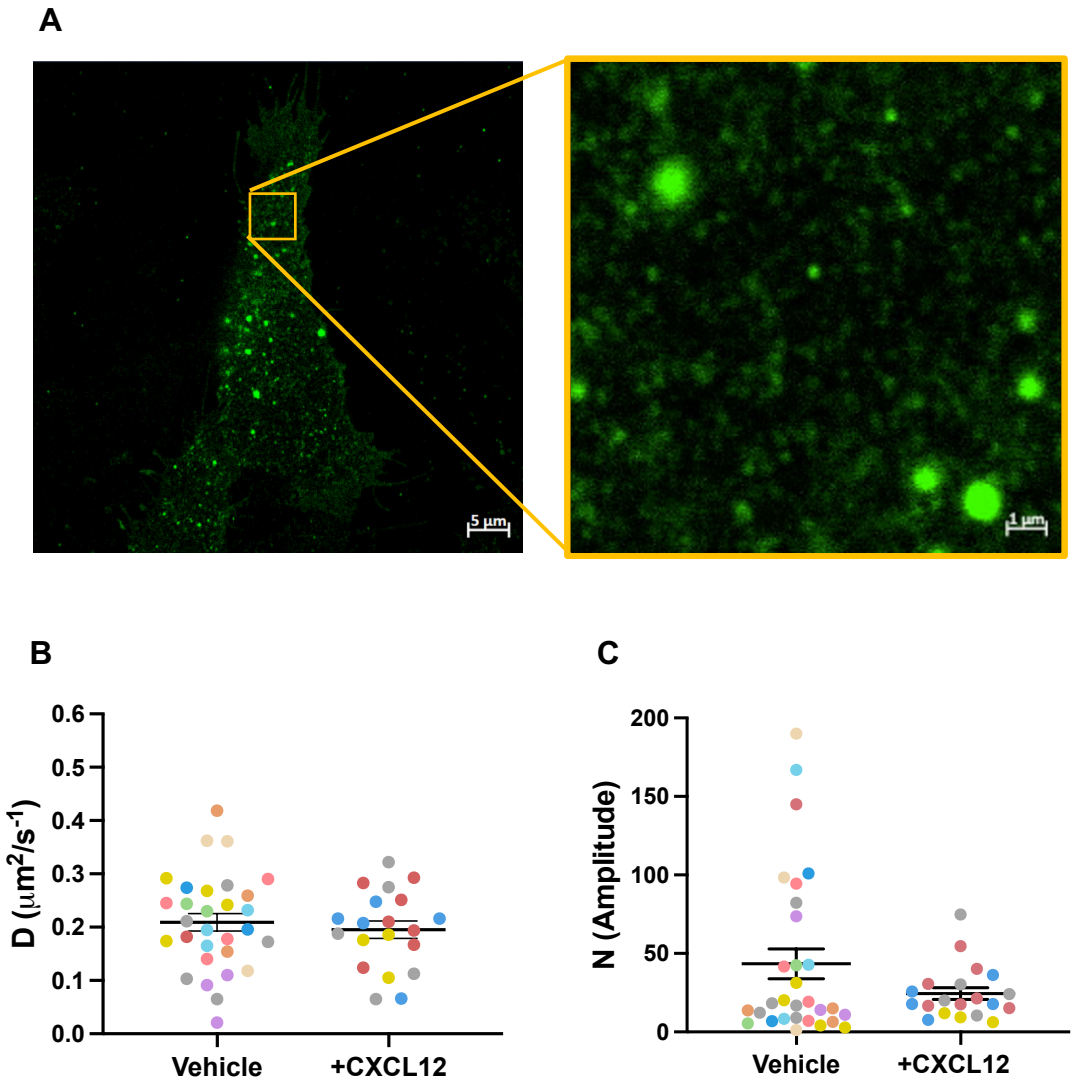

Figure 4.7: Dynamics and organisation of plasma membrane SNAP-ACKR3 measured with raster image correlation spectroscopy (RICS). *HEK293 SNAP-ACKR3 cells were labelled with 100 nM SNAPsurface Alexa 488 and RICS measurements were taken on the basal cell membrane following stimulation with vehicle or 10 nM CXCL12 (10 mins, RT)* ***A:*** *Representative image of basal membrane (left) and representative RICS data (right) from SNAP-ACKR3 basal condition (reused figure from Chapter 2)* ***B:*** *Diffusion coefficient (D_{RICS}) of SNAP-ACKR3 showed no significant change with 10 nM CXCL12* ***C:*** *Receptor density of SNAP-ACKR3 presented no significant difference upon CXCL12 addition (n=20-30 cells from a minimum of 4 individual experiments, unpaired Student's t-test (ns; p<0.05). Error bars = SEM; scale bar = 5 µm (left) and 1 µm (right).*

The collected raw data can also be used for Number and Brightness (N&B) analysis, which provides information about the average brightness of the receptor and the number of particles per pixel as an indication of the oligomerisation state of the receptor [100]. With N&B, in contrast to PCH analysis, only one species of brightness can be resolved. The application of N&B analysis created three image maps per raw image series. These represented the maximum intensity projection, apparent number image and the apparent brightness image (Figure 4.8/A). On these image maps, some bright or high-intensity areas were observed, suggesting cluster formation. Some of these bright vesicles are marked with a magenta arrow or circle in the representative images per conditions (Figure 4.8/A). To avoid skewing by saturated areas, three regions of interest (ROIs) were chosen with an area of ~12 μm^2 per image stack (Figure 4.8/B). To assess ACKR3 oligomerisation via N&B analysis, a monomeric control, β1-adrenergic receptor and a dimeric control, CD28 were used [133, 159].

The apparent number of particles per pixel (Figure 4.8/C) was 2.15±0.10 in the case of ACKR3 vehicle (coefficient of variation 42.1%, n=90 ROI/ 30 cells from 10 independent experiments). Following CXCL12 stimulation the apparent number was significantly lower (1.75±0.08, coefficient of variation 32.8%, n=57 ROI/ 19 cells from 5 independent experiments; unpaired Student's t-test; **$p<0.01$). Under basal conditions, SNAP-ACKR3 showed an apparent brightness of 1.94±0.11 with a 55.6% coefficient of variation (n=30 cells/ 90 ROIs from 10 independent experiments), indicating a heterogeneous organisation. Following CXCL12 stimulation, the apparent brightness did not change significantly (1.92±0.09; coefficient of variation 34.0%; n=19 cells/ 57 ROIs from 5 independent experiments). Joelle Goulding previously collected N&B data of monomeric β1 (apparent brightness 1.31±0.02; coefficient of variation 6.4%; n=32 cells) and dimeric CD28 (apparent brightness 1.41±0.02; coefficient of variation 8.6%; n=28 cells) receptors, using the same conditions. She generously provided this data for this study to use as monomer and dimer control. SNAP-ACKR3 apparent brightness in both basal and CXCL12 conditions presented significantly higher brightness values than observed in the controls with a much higher coefficient of variation, suggesting the

presence of clusters and higher oligomeric states of ACKR3 compared to the dimer control CD28.

Table 4.3: Grouped data of RICS parameters for SNAP-ACKR3. *RICS diffusion coefficient (D_{RICS}) and amplitude (N). Number and Brightness parameters including number of particles (Number) in the condition of the vehicle and 10 nM CXCL12 (10 mins) cells, n=20-30 cells from a minimum of 4 individual experiments (unpaired Student's t-test; **p<0.01).*

Condition	RICS		N&B
	D_{RICS} (μm²/s)	N (Amplitude)	Number
Vehicle	0.209±0.017	43±10	2.2±0.1
CXCL12	0.195±0.016	25±4	1.8±0.6 **

Table 4.4: Apparent brightness for ACKR3, B1 and CD28*. Apparent brightness data from Number and Brightness analysis in the condition of the ACKR3 vehicle, ACKR3 + 10 nM CXCL12 (10 mins), monomeric control B1 and dimeric control CD28 cells, n=20-32 cells from minimum 3 individual experiments (one-way ANOVA, Turkey's multiple comparison, *p<0.05, **p<0.01).*

Condition	N&B
	Brightness
ACKR3 Vehicle	1.94±0.11 (*vs CD28; ** vs B1)
ACKR3 + CXCL12	1.92±0.09 (*vs CD28; ** vs B1)
B1	1.31±0.01
CD28	1.41±0.02

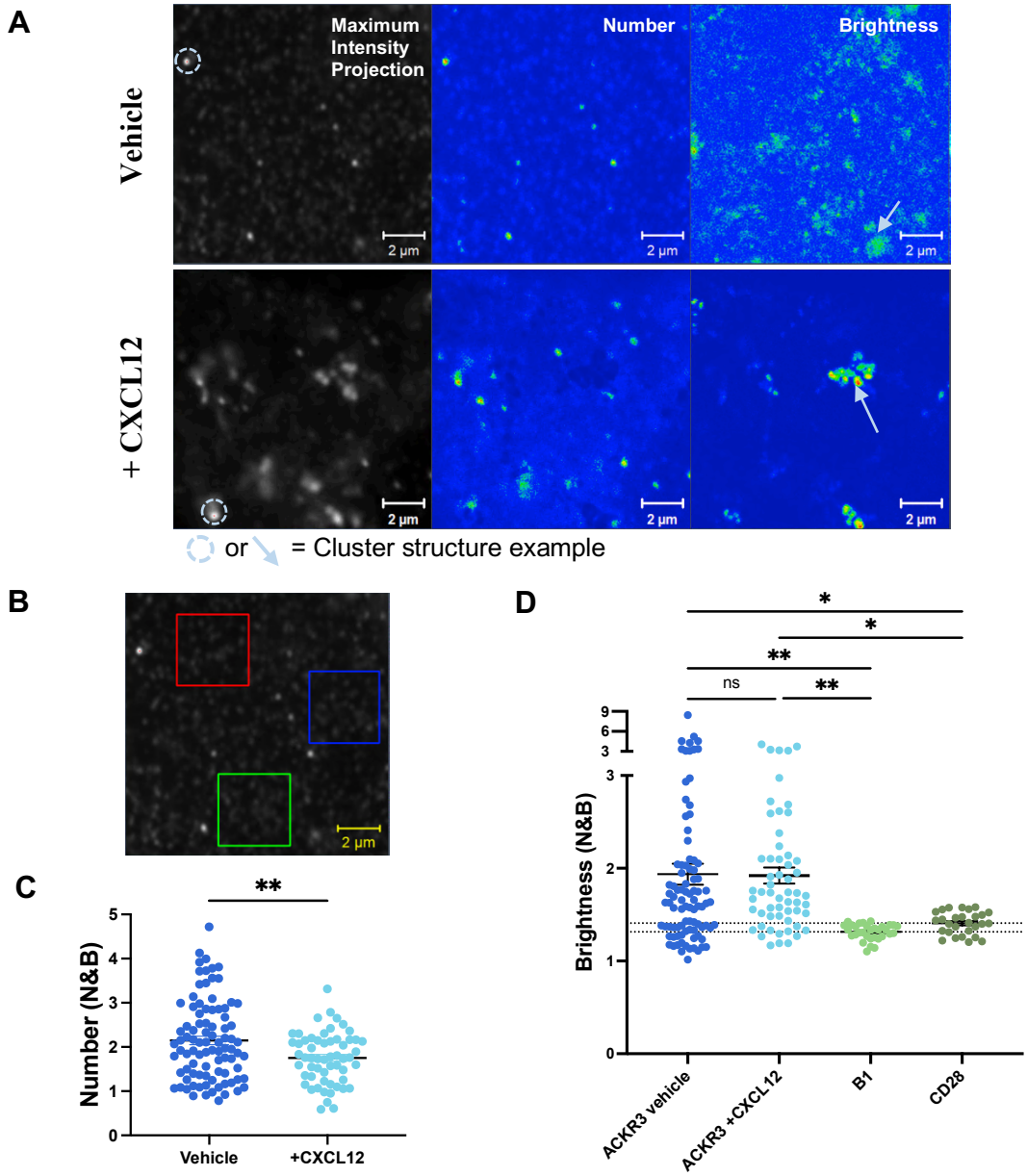

Figure 4.8: Number and Brightness analysis of SNAP-ACKR3. *RICS data of HEK293 SNAP-ACKR3 following stimulation with vehicle or 10 nM CXCL12 was used for N&B analysis.* ***A:*** *Representative Maximum intensity projection image, Number map and Brightness map of a 256x256 pixel field of view following treatment with vehicle and CXCL12* ***B:*** *Three 12 µm^2 regions of interest (rectangles) are selected to derive the average derived parameters.* ***C****: Derived apparent number of particles of SNAP-ACKR3 showed a significant decrease upon CXCL12 stimulation (unpaired Student's t-test; **p<0.01).* ***D:*** *Apparent brightness of SNAP-ACKR3 cells treated with CXCL12 showed non-significant change compared to vehicle (unpaired Student's t-test). Both vehicle and CXCL12 condition of SNAP-ACKR3 presented significantly increased brightness (one-way ANOVA, Turkey's multiple comparison, *p<0.05, **p<0.01) compared to B1 monomer and CD28 dimer control (measured by J. Goulding, n=28-32 from a minimum 3 individual experiments) Error bars=SEM. Scale bar = 2 µm.*

4.4. Discussion

This chapter investigated the dynamics and organisation of the ACKR3 receptor at the plasma membrane and the impact of CXCL12 stimulation on these membrane dynamics. Confocal imaging, FCS, FRAP and RICS measurements with HEK293 SNAP-ACKR3 cells were used to study the receptor dynamics within the membrane at nano, micro and macro scale, respectively. Our data showed a significant decrease in diffusion upon CXCL12 stimulation on the nano and micro scale and a change in receptor mobility. In contrast, there were no changes in ACKR3 mobility upon CXCL12 addition on the macro scale.

Table 4.5: Summary of the diffusion coefficient of ACKR3 measured at different scale. *FCS diffusion coefficient (D_{FCS}), FRAP diffusion coefficient (D_{FRAP}) and RICS diffusion coefficient (D_{RICS}) in the condition of the vehicle and 10 nM CXCL12 (10 mins) cells, n=20-38 cells from a minimum of 3 individual experiments (unpaired Student's t-test; ** p<0.01, **** p<0.0001).*

Condition	FCS	FRAP	RICS
	D_{FCS} ($\mu m^2/s$)	D_{FRAP} ($\mu m^2/s$)	D_{RICS} ($\mu m^2/s$)
Vehicle	0.200±0.011	0.060±0.003	0.209±0.017
CXCL12	0.126±0.012 ****	0.050±0.002 **	0.195±0.016

As previous studies indicated that ACKR3 can constitutively internalise and recycle to the plasma membrane [150], our first aim was to find the most suitable SNAP labelling conditions to measure receptor dynamics at the plasma membrane. For this optimisation step, the SNAP-ACKR3 receptor was labelled with membrane impermeable SNAP Surface Alexa 488 dye in three different conditions: 4 °C (for 1 hour), RT (for 30 mins) or 37 °C (for 30 mins). Using membrane impermeable dye means that detection of any fluorescently labelled receptor will indicate active internalisation after labelling due to constitutive internalisation or ligand stimulation, as labelling will only occur at the cell surface. Confocal time series images of SNAP-ACKR3 were recorded following the three different labelling conditions. While 4 °C SNAP labelling first showed mainly membrane localisation of ACKR3 receptors, it presented

increased intracellular location over time. Following RT labelling, the SNAP-ACKR3 receptor was predominantly localised intracellularly while still partially present at the plasma membrane, which was maintained over time. In the confocal time-series imaging videos, the movements of intracellular vesicles were observed. The 37 °C SNAP labelling presented similar receptor localisation as RT; however, we observed focal drift over time. Based on the confocal data, the RT labelling was chosen to be the most suitable to study ACKR3 membrane dynamics as the ACKR3 receptor was still partially present at the membrane and this condition was closer to physiological conditions and mobility than the 4 °C but with a limited risk of focal drift. Single-point FCS was used to confirm that the different labelling temperatures do not affect the ACKR3 receptor diffusion. The diffusion coefficient did not change significantly between the three SNAP labelling conditions, while the receptor density was significantly higher after 37 °C labelling compared to 4 °C labelling, however, 37 °C labelling presented highly variable values and challenges to keep the detection volume on the membrane due to focal drift. This data confirmed that RT labelling is the most suitable for studying SNAP-ACKR3 receptor dynamics at the plasma membrane.

Following optimisation of labelling conditions, the location and distribution of the SNAP-ACKR3 receptor were studied under basal and CXCL12 stimulation. As seen above, confocal images of SNAP-ACKR3 under basal conditions presented significant intracellular location with partly membrane labelling, aligning with the continuous constitutive internalisation and recycling observed in previous studies [150, 160]. Upon CXCL12 stimulation, ACKR3 showed similar mainly intracellular localisation. ACKR3 localisation under basal conditions greatly differs from SNAP-CXCR4 location (Chapter 3/Figure 3.1), which presented mainly membrane location. In addition, while CXCR4 showed partial internalisation upon CXCL12 addition, the CXCL12-activated ACKR3 displayed a similar intracellular distribution but a higher degree of receptor in bright vesicles.

To gain insight into the spatial dynamics of ACKR3 at the plasma membrane on different scales, FCS, FRAP and RICS techniques were used. In addition,

PCH and Number and Brightness analysis were used with FCS and RICS datasets, respectively, as alternative data analysis to gain information about the oligomeric state of ACKR3. FCS can provide information about the receptor dynamics on a nanoscale (detection area ~0.09 μm^2). We employed this approach successfully to study SNAP-CXCR4 dynamics at the plasma membrane. However, as ACKR3 localised in bright intracellular vesicles, this can skew and modify the z-scan peak, which is used as an indication of the membrane location. Thus, to address this challenge, we introduced an additional step in the protocol. This additional step was used in a previous study to measure β2-adrenoreceptor dynamics at the membrane in human embryonic stem (ES) cells where the peak differs from the membrane due to the non-uniform nature of these cells [79]. In the case of measuring ACKR3 dynamics, the detection volume was placed ~1.5 μm above the peak and was lowered in small steps taking short fluorescence fluctuation reads until reaching the first membrane trace. The raw fluorescence fluctuation curves were fitted to a two-component diffusion model, where the 3D faster component indicates the free SNAP dye and the 2D slower-moving component represents the membrane-bound receptor [84]. ACKR3, under basal conditions, presented a slower diffusion rate (0.200±0.011 $\mu m^2/s$) than we observed in the case of CXCR4 (0.287±0.011 $\mu m^2/s$), while it is within the range with other GPCRs measured previously [77, 81]. The slower diffusion of ACKR3 could suggest a higher oligomerisation state than CXCR4, or, alternatively, a more restricted movement of the receptor across the plasma membrane due to interactions with other proteins that restrict its movement. The density of ACKR3 was 124±20 $N/\mu m^2$ which is lower than we observed in the case of SNAP-CXCR4 cells. This could be due to the ACKR3 receptor continuously internalising; however, as we were using mixed (not single clone) population cell lines stably expressing the SNAP-tagged receptors, it is challenging to compare the receptor density or relate it to physiological levels of expression.

Upon CXCL12 stimulation, we observed a significant slowing down in SNAP-ACKR3 diffusion (0.126±0.012 $\mu m^2/s$). This suggests a ligand-induced change in receptor dynamics in the nanoscale. A ligand-induced change and

slowdown in diffusion was also observed previously with other GPCRs such as the μ-opioid receptor upon DAMGO stimulation and the neuropeptide Y (NYP) 1 receptor upon NPY addition. The studies suggested that the change in the diffusion might indicate receptor endocytosis and receptor movement to the clathrin pit prior to internalisation [81, 84]. This change in diffusion properties induced by CXCL12 was not observed for CXCR4, indicating different effects of the shared ligand on receptor dynamics at the nano scale. The density of ACKR3 did not change significantly upon CXCL12 addition. However, the data values are highly variable and, with almost no data lying around the mean ± SEM region, might suggest a bimodal distribution of heterogeneous receptor organisation of the receptor. As FCS data is collected from a small membrane region, this difference can come from the heterogeneity of the local membrane [137]. Collecting more data might give us an answer as to whether the density can be separated into two different organisation groups depending on the local membrane.

The fluorescence fluctuation trace was also used for alternative PCH analysis, which provides information about the oligomeric state of the receptor. PCH analyses the fluctuation trace in terms of amplitude by segmenting it into time bins and detailing the resulting frequency distribution of photon counts within these bins [161, 162]. As discussed in the previous chapter, PCH analysis can detect 2-fold changes in mass [77]. However, without monomer and dimer control, we cannot determine the precise stoichiometry of the receptor but can identify the presence of different oligomeric states. When two different receptor populations are present, the PCH analysis necessitates the inclusion of a second component due to a skewed fit on the high photon bin end. This results in an increased average molecular brightness, indicating a brighter second component. The brightness profile of SNAP-ACKR3 cells under basal conditions showed that 40.62% of the cells presented a second brighter component, suggesting that the ACKR3 might form clusters even in vehicle conditions and that the receptor population at the membrane is heterogeneous. This contrasts with our observation in the case of CXCR4, where the receptor population was predominantly represented by a single component, indicating a more homogenous oligomeric state at the plasma

membrane. Upon CXCL12 stimulation, a similar brightness profile was observed with 41.18% of cells with the second component. This indicates no significant ligand-induced change in ACKR3 receptor stoichiometry, which is also different from CXCR4, where cells presented an increased percentage of the second component, indicating receptor cluster formation upon CXCL12 stimulation. Overall, FCS data suggests no significant changes in ACKR3 clustering upon CXCL12 stimulation, while a reduction in diffusion coefficient was observed. This might be attributed to interaction with the clathrin pit or other cytoskeletal elements. Although the density of ACKR3 remained unchanged, the data indicates bimodal distribution. Furthermore, PCH data revealed a slightly increased brightness for the second component and a lower value for the first component. This might suggest that some fraction of the measured ACKR3 population forms larger clusters upon CXCL12 stimulation, while other subpopulations remain in lower oligomeric states. The collection of more FCS is required to strengthen this suggestion.

FRAP was used as a complimentary technique to assess the mobility of ACKR3 and its diffusion over a larger membrane area. FRAP, in contrast to FCS, can provide information about the immobile fraction of the receptor [82, 125]. FRAP diffusion data revealed a slower diffusion coefficient compared to FCS, a discrepancy that was also observed in our CXCR4 study. This difference can come from the restriction of membrane heterogeneity over a larger membrane area, applying a limiting effect on the free receptor diffusion [133]. FRAP data presented a significant decrease in the micro diffusion coefficient (D_{FRAP}) of ACKR3 upon CXCL12 addition. In previous studies, a similar effect was shown upon ligand stimulation of NPY Y1 receptor dynamics measured both with FCS and FRAP [81]. The immobile fraction of ACKR3 was significantly increased after CXCL12 stimulation compared to vehicle conditions. This agonist-induced increased immobile fraction was also observed in the case of the CXCR4 receptor (Chapter 3) and other GPCRs such as μ-opioid receptor (MOR) [84]. Based on these results, the observed micro-scale changes in ACKR3 receptor mobility and diffusion upon CXCL12 stimulation may be attributed to receptor clustering within clathrin-coated pits before internalisation, resulting in slower receptor speed and immobilisation.

The change in lateral mobility can also be caused by cytoskeletal barriers limiting movement between membrane microdomains [163].

Finally, a complementary method, RICS, was employed to obtain a more comprehensive view of ACKR3 dynamics at the membrane on a macro-scale. RICS provides information about diffusion and receptor density in a manner similar to FCS but with an additional spatial parameter and a detection area of ~70 μm^2 [85, 153]. RICS analysis excludes slow-moving and immobile components and uses a 2D diffusion model to determine the diffusion parameters of the mobile fluorescent species [151, 153]. The RICS data showed no significant difference in the macro diffusion coefficient (D_{RICS}) and amplitude of ACKR3 upon CXCL12 stimulation. In addition, the diffusion coefficient of ACKR3 under basal conditions was similar to the value measured with FCS. However, D_{RICS} of CXCL12-activated ACKR3 was faster than measured using FCS. While CXCL12-induced changes can be observed on nano and micro scales with FCS and FRAP techniques, this result suggests no ligand-induced effect on ACKR3 dynamics on a whole cell macro scale. While RICS has been previously used to study the lateral diffusion of different receptors [153, 164], a more recent study proposed that the background filtering of slow-moving and immobile components might cut off relevant data and form a crucial limitation in RICS approaches [165]. As FCS and FRAP showed a slowdown of ACKR3 upon CXCL12 stimulation, the moving-average filter in RICS might have a more relevant effect, excluding important diffusion information. In addition, ACKR3 membrane distribution presented to be heterogeneous; hence, applying RICS measurement on a smaller, more homogenous region might provide more accurate results. Additionally, using different background extractions, such as cross-correlation subtraction, would provide a more dynamic background filter. However, the limitations in temporal resolution by the filter would still be present to a certain level [165, 166]. RICS data can be used for alternative Number and Brightness (N&B) analysis. N&B analysis was carried out over three 12 μm^2 area regions of interest within the raw RICS image stack and it gave information about the average brightness of the receptor and the number of particles per pixel. Comparing the brightness to a monomer (B1) and dimer (CD28) can provide information about the

oligomeric state of the ACKR3 [100, 133]. ACKR3 under basal and CXCL12 conditions presented significantly higher apparent brightness values compared to monomer and dimer controls, indicating ACKR3 clustering. Of note, the coefficient of variation of ACKR3 data presented to be high (34-56%), showing great variability which might suggest the presence of ACKR3 in different oligomeric states. The brightness value of ACKR3 following CXCL12 addition was not changed compared to a basal condition, which aligns with our finding in PCH analysis, suggesting that the oligomeric state of ACKR3 may not change upon ligand stimulation. The number of particles per pixel was significantly lower in the case of CXCL12-stimulated ACKR3 compared to the basal condition. Based on this data, we can hypothesise that while the oligomeric state of ACKR3 does not show ligand-induced change, CXCL12 stimulation may result in the formation of larger clusters. Moreover, the internalisation of the ACKR3 receptor could also contribute to the decrease in the apparent number. Previous unpublished N&B data of CXCR4 by Joelle Goulding showed no significant difference in apparent brightness and apparent number upon agonist or antagonist stimulation of this receptor. In addition, basal CXCR4 brightness showed a similar value as a monomer control, demonstrating the difference in basal oligomeric state between CXCR4 and ACKR3. This observation using the Number and Brightness analysis also agrees with the PCH analysis data presented and detailed above.

This chapter demonstrated a decrease in ACKR3 lateral diffusion at the plasma membrane on the nano and micro scale accompanied by an increased immobile fraction measured with FRAP. These alterations potentially suggest cluster formation; however, PCH analysis indicates that nearly half of the ACKR3 population is already in a clustered state under basal conditions, without any significant difference in the oligomeric state of the receptor upon CXCL12 stimulation. This finding is supported by N&B analysis of the complimentary RICS data, suggesting that ACKR3 is clustered in both basal and CXCL12-activated conditions. These observations suggest a partial change in the ACKR3 population towards larger cluster formation or interaction with the clathrin pit before internalisation. In addition, the lack of change in density measured with FCS and RICS might be due to the continuous

internalisation and recycling of ACKR3. Although previous studies documented the internalisation and recycling of the ACKR3 receptor following CXCL12 activation, the duration of the event remains undetermined [73]. Our indication regarding of the formation of a larger cluster subpopulation and partial internalisation also aligns with the decrease in the number of particles observed by N&B analysis. Further data collection involving CXCL12 is necessary to evaluate the proposed changes thoroughly. Moreover, employing other advanced microscopy techniques, such as single molecule tracking, would provide a more in-depth view to understand the organisation of ACKR3 at the plasma membrane.

During the concluding phase of this project, Rob Leurs's laboratory (Vrije Universiteit Amsterdam) created a small-molecule compound, VUF16840, which is an inverse agonist of ACKR3 [66]. We carried out preliminary imaging experiments to observe the distribution of ACKR3 following 2 hours of preincubation with the inverse agonist, with the expectation to observe higher membrane retention upon inverse agonist incubation. Preliminary images (Figure 4.9) showed the expected increased membrane location of ACKR3. Given the promising nature of this result, it would be valuable to explore potential changes in the ACKR3 receptor dynamics upon VUF16840 stimulation.

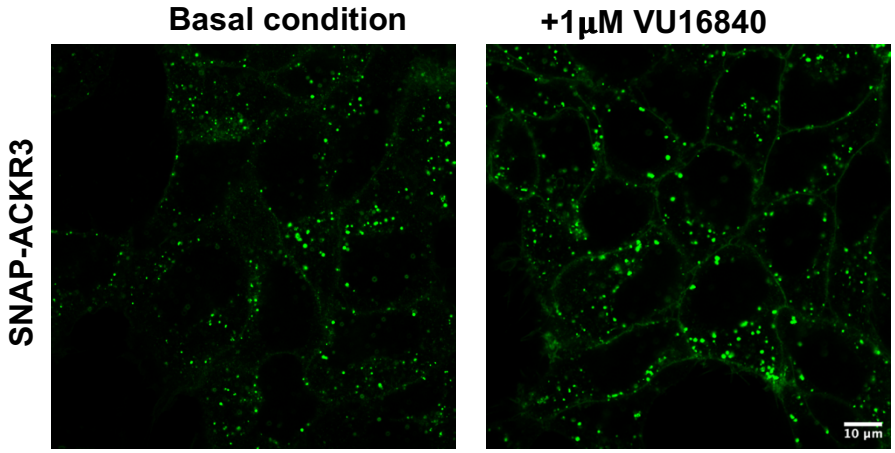

Figure 4.9: The localisation of SNAP-ACKR3 following preincubation with inverse agonist VUF16840*. Cells were labelled with SNAP-Surface Alexa Flour 488 as indicated in Chapter 4 Methods and imaged on Zeiss LSM 880 microscope using 40x c-Apochromat water immersion objective 1.2 NA on zoom 3x. The images are a representative example from 2 independent experiments. Scale bar = 10 μm.*

4.5. Conclusion

In conclusion, we observed an intracellular localisation of ACKR3 within bright vesicles, and the receptor localisation does not change significantly upon CXCL12 stimulation. We showed a significant decrease in ACKR3 diffusion speed upon CXCL12 stimulation when assessed using FCS. Both basal and CXCL12 conditions of ACKR3 showed a high percentage of second brightness component in PCH analysis, indicating cluster formation and a high oligomeric state of the ACKR3 receptor. The diffusion coefficient measured with FRAP over a larger membrane area presented a similar significant reduction upon CXCL12 addition and an increase in the immobile fraction of the receptor, suggesting agonist-induced changes in receptor mobility. Assessing the dynamics on the macro scale with RICS revealed no significant change in ACKR3 diffusion following CXCL12 stimulation. Number and Brightness analysis detected a significant decrease in apparent number value upon CXCL12 addition, which might indicate increased aggregation or internalisation of the receptor. The apparent brightness was similar in basal and CXCL12 conditions of ACKR3, while these values were significantly higher compared to monomeric B1 and dimeric CD28 control, suggesting cluster formation and heterogenous organisation of ACKR3 at the cell surface. These data show how complementary information obtained with different spectroscopic methods assessing different membrane sizes can be used to start delineating the dynamics and organisation of the ACKR3 receptor. Future experiments determining oligomer/cluster sizes will be of value to understand the signalling and functions of this atypical chemokine receptor 3.

Chapter 5: Effect of GRK Depletion on ACRK3 Receptor Localisation

5.1 Introduction

The regulation of GPCR signalling and function is primarily influenced by receptor desensitisation, internalisation and trafficking [167]. GPCR endocytosis is a complex process that retrieves receptors from the membrane upon ligand stimulation, mainly through recruitment to clathrin-coated pits (CCPs). This process can be through clathrin-dependent β-arrestin-independent or β-arrestin-dependent pathways.

The β-arrestin-dependent endocytosis is the most common mechanism of GPCR endocytosis. Following the phosphorylation of the ligand-activated receptors by G protein-coupled receptor kinases (GRKs), β-arrestins bind to the activated and phosphorylated receptors [168]. The activated, receptor-bound β-arrestin interacts with AP-2 and is recruited to the clathrin-coated pits for endocytosis [169, 170]. GRK-mediated phosphorylation seems to be essential for the β-arrestin-dependent internalisation of most GPCRs, although other kinases and phosphorylation-independent β-arrestin interactions have also been described [171, 172]. A recent study assessing the role of different GRK isoforms (GRK2,3,5,6) on the regulation of Angiotensin II type 1A receptors showed that GRK2/3 pre-dominantly mediate arrestin-dependent endocytosis while GRK5/6 mainly participate in signal regulation suggesting that different GRK isoforms can have diverse functional role for the same GPCR [173]. Moreover, in the case of some receptors, like formylpeptide receptor 1 (FPR1) and BLT1, leukotriene receptor, research showed that receptor endocytosis can be GRK phosphorylation-dependent and β-arrestin-independent [174, 175].

Another route for GPCR internalisation is through clathrin-dependent endocytosis, where the activated receptors can directly interact with adaptor proteins such as adaptor protein-2 (AP-2) and epsins in a β-arrestin-independent way. The receptors get recruited to clathrin-coated pits, which later form into clathrin-coated endosomal vesicles [176, 177]. This process is mediated by the large GTPase dynamin, clathrin, and adaptor proteins [178, 179].

In addition to agonist-induced receptor endocytosis, GPCRs can also constitutively internalise in the absence of ligand stimulation. Studies with various GPCRs, such as β2-adrenergic or muscarinic M3 receptors, suggest a distinct endocytosis process for the constitutively internalised receptors compared to the ligand-induced internalisation [180]. A study with CXCR4 also revealed distinct pathways of constitutive internalisation, different to the CXCL12-induced endocytosis pathway. While the activated receptor internalises through the arrestin-dependent route, the constitutive internalisation does not require arrestin and only depends on protein kinase C (PKC) and dynamin [181, 182]. Following receptor internalisation, the receptor can either dephosphorylate and recycle back to the plasma surface or continue its trafficking to lysosomes, leading to receptor degradation [183, 184]. Caballero et al. showed a role for GRK6 in CXCR4 lysosomal degradation [74], which might suggest a role of GRKs further downstream in receptor trafficking and in influencing receptor fate upon internalisation. While there are extensive studies focused on CXCR4 endocytosis, there is limited knowledge about the mechanism of ACKR3 internalisation, which shares the ligand CXCL12 with CXCR4. As described in Chapter 1 and presented in Chapter 4, ACRK3 is constitutively internalised, recycles to the plasma membrane, and upon activation, it can recruit β-arrestin1 and 2 [147, 150]. Previous studies have shown agonist-induced β-arrestin-mediated internalisation of ACKR3 [72], while more recent studies reported that receptor internalisation can occur in the absence of β-arrestins [73, 185]. Although there is controversy about the involvement of β-arrestin, various research has shown the involvement of GRKs in agonist-induced ACKR3 internalisation. Using various phosphorylation site ACKR3 mutant including a full ST/A mutant and Rab5a sensors, Zarca et al. showed that ACKR3 C-tail phosphorylation seems to be essential for endocytosis, and that internalisation is GRK2/3 dependent [73]. Another study using an ACKR3-ST/A mutant also indicated that the CXCL12-induced endocytosis of ACKR3 is phosphorylation-dependent and supports that the involvement of GRKs is required for ligand-induced internalisation [186].

Despite the above studies suggesting the involvement of GRKs in ligand-dependent ACKR3 internalisation, the role and precise mechanism underlying GRKs participation in the constitutive internalisation of ACKR3 are still unknown and require further investigation. In this context, Drube et al. have recently created a platform to study the role of individual and combinations of GRKs in GPCR signalling trafficking by generating a collection of CRISPR/Cas-9 GRK KO HEK293 cell lines. These cells were validated using Western blot and functionality with several assays involving multiple GPCRs [95]. These unique cell lines were used throughout this chapter to investigate the possible involvement of GRKs in ACKR3 internalisation and trafficking.

As presented in Chapter 4, ACKR3 is continuously internalised and recycled back to the plasma membrane. In basal, unstimulated, conditions ACKR3 is predominantly located in intracellular vesicles, which makes the assessment of receptor dynamics at the plasma membrane challenging. We hypothesised that blockade of potential GRK-mediated internalisation in GRK knock-out cell lines would retain ACKR3 at the plasma membrane, which would be advantageous for FCS studies. Unexpectedly, instead of receptor accumulation at the plasma membrane, we observed a distinct intracellular redistribution of ACKR3 upon GRK depletion. Thus, in this chapter we aimed to investigate further the role of GRKs in ACKR3 distribution and function with confocal imaging and co-localisation studies with intracellular compartment markers.

5.2 Methods

To study the effect of GRK depletion, CRISPR/Cas-9 GRK-knockout HEK293 cell lines were received from Carsten Hoffmann's lab [95], and used for the creation of mixed population cell lines stably expressing either SNAP-ACKR3 or SNAP-CXCR4. The following cell lines were created: HEK293 ΔqGRK SNAP-ACKR3 and HEK293 ΔqGRK SNAP-CXCR4 (where GRKs 2,3,5 and 6 were deleted), HEK293 ΔGRK2/3 SNAP-ACKR3 (where GRKs 2 and 3 were deleted) and HEK293 ΔGRK5/6 SNAP-ACKR3 (where GRKs 5 and 6 were deleted). For comparison, HEK293 SNAP-ACKR3 and HEK293 G SNAP-CXCR4 were used.

For the arrestin recruitment assay (K-Ras BRET), the HEK293 control cell line (obtained from Carsten's lab) was used as a control. The different cell culture protocols are detailed in Chapter 2 (2.1 Cell Culture).

The experimental protocols used in this chapter are described in detail in Chapter 2, General Methods. Here, the approaches and techniques used were bystander arrestin recruitment assays (K-Ras BRET) and confocal microscopy to assess receptor co-localisation with Early Endosome (EEA) and lysosomal-associated membrane protein 1 (LAMP-1) lysosome markers. In addition to co-localisation analysis with the lysosome marker the the average LAMP-1 and SNAP-tagged receptor intensity per cell were analysed for each cell line as detailed in General Methods.

5.3 Results

5.3.1 Effect of GRK Depletion on ACKR3 Location and Function

In the previous chapters, the distribution of SNAP-ACKR3 and SNAP-CXCR4 in HEK293 and HEKG cells, respectively, was assessed following 30 minutes of labelling with SNAP Surface Alexa 488 (1μM). These experiments showed that, in contrast to the clear cell surface localisation of CXCR4, constitutive internalisation of ACKR3 prevented its accumulation at the plasma membrane. Thus, we hypothesised that preventing such internalisation would retain the receptor at the plasma membrane, allowing FCS experiments of this receptor to be made more easily. As GRKs have been suggested to participate in ACKR3 trafficking, we reasoned that inhibition or absence of GRKs, would have such effect.

We used the CRISPR/Cas-9 quadruple knock-out (ΔQGRK) HEK293 cells from the Hoffmann lab (Jena, Germany), which lack the GRK isoforms 2,3,5 and 6 and generated HEK293 ΔQGRK SNAP-ACKR3 and HEK293 ΔQGRK SNAP-CXCR4 mixed population stable cell lines.

To determine and compare the function of SNAP-ACKR3 in WT and ΔQGRK cells, we used a bystander K-Ras β-arrestin2 recruitment BRET-assay. HEK293 control, SNAP-ACKR3 and ΔQGRK SNAP-ACKR3 cells were transfected with K-Ras Venus and β-arrestin2 Nluc, as well as GKR2 (where stated) to investigate the effect of reintroducing GRK. In this bystander BRET assay, receptor activation with the agonist, CXCL12, results in β-arrestin2 Nluc (donor) recruitment to the plasma membrane and which brings it in close proximity to the membrane-bound K-Ras Venus (acceptor), resulting in energy transfer and increased BRET signal (Figure 5.1/A). In WT cells, activation of ACKR3 with 10 nM CXCL12 lead to β-arrestin2 recruitment which resulted in 1.037±0.006 fold change (n=5), which was significantly reduced in ΔQGRK SNAP-ACKR3 cells, where there was no detectable recruitment of β-arrestin2 (fold change = 0.999±0.006, n=5, p = 0.001). Upon the overexpression of GRK2 in the ΔQGRK SNAP-ACKR3 cells, β-arrestin2 recruitment was

rescued, achieving a fold change (1.035±0.003, n=5, ns, p=0.966 vs WT and p=0.0015 vs ΔQGRK) similar to WT SNAP-ACKR3 cells (Figure 5.1/B). HEK293 control cells without the receptor and with or without GRK2 were used as a negative control to confirm that the β-arrestin2 recruitment was caused by the ACKR3 receptor. The CXCL12 stimulation in HEK293 control cells without the ACKR3 caused no significant change without (0.990±0.01) and with (0.994±0.004) the reintroduction of GRK2 (n=3, ns, p=0.916 HEK control vs HEK control+GRK2; Figure 5.1/C), which confirms that the observed recruitment is ACKR3-mediated.

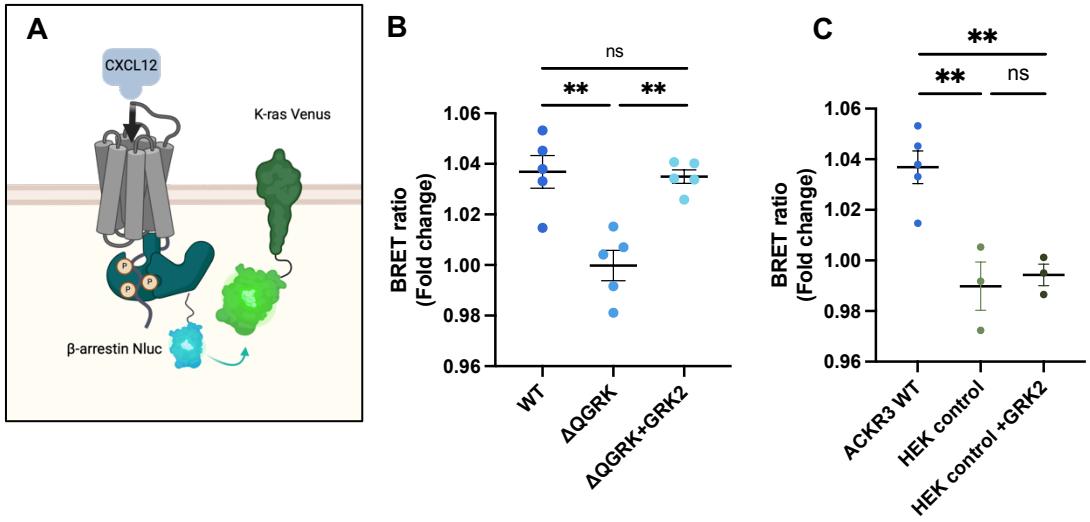

Figure 5.1: K-Ras arrestin recruitment assay upon CXCL12 stimulation. ***A:*** *Schematic representation of β-arrestin recruitment upon receptor activation by CXCL12. Receptor activation induces β-arrestin Nluc (donor) recruitment and brings it in close proximity to the membrane-bound K-Ras Venus marker (acceptor), resulting in energy transfer and increased BRET signal.* ***B:*** *Fold change in BRET signal from basal condition upon CXCL12 activation compared in WT, ΔQGRK and ΔQGRK + GRK2 cells expressing SNAP-ACKR3. Fold change was calculated from the BRET ratio (CXCL12) divided by the correspondence vehicle BRET ratio. (n=5, one-way ANOVA followed by Tukey's multiple comparisons test ** p < 0.01; ns > 0.05).* ***C:*** *Negative control with HEK control cells without ACKR3 with and without overexpression of GRK2 compared to WT cells expressing SNAP-ACKR3 (minimum n=3 individual experiment, one-way ANOVA followed by Tukey's multiple comparisons test ** p < 0.01; ns > 0.05). The data points represent individual experiments. Error bar =SEM.*

Following the confirmation that the ΔQGRK SNAP-ACKR3 cells were unable to recruit β-arrestin2 in response to CXCL12, the location of the ACKR3 receptor within these cells was assessed through confocal imaging and its distribution was compared to the wild-type. Additionally, the distribution of SNAP-CXCR4 in ΔQGRK was also examined.

After SNAP labelling with membrane impermeable SNAP Surface Alexa 488, the ΔQGRK SNAP-CXCR4 cells exhibited membrane labelling similar to the 'wide type' SNAP-CXCR4 cell line (Figure 5.2 bottom panels). Unexpectedly, quadruple GRK depletion did not result in increased ACKR3 localisation at the plasma membrane but instead presented a distinct intracellular distribution, different to that observed for SNAP-ACKR3 in WT cells (Figure 5.2 top images). In ΔQGRK SNAP-ACKR3 cells, the bright intracellular receptor vesicles suggested some sort of intracellular accumulation and crowding of the receptor. Since a membrane-impermeable SNAP dye was used, the fluorescent ACKR3 receptors must have originated at the cell surface and subsequently underwent internalisation following SNAP labelling. Based on these results we decided to investigate further the role of GRKs in ACKR3 location and function.

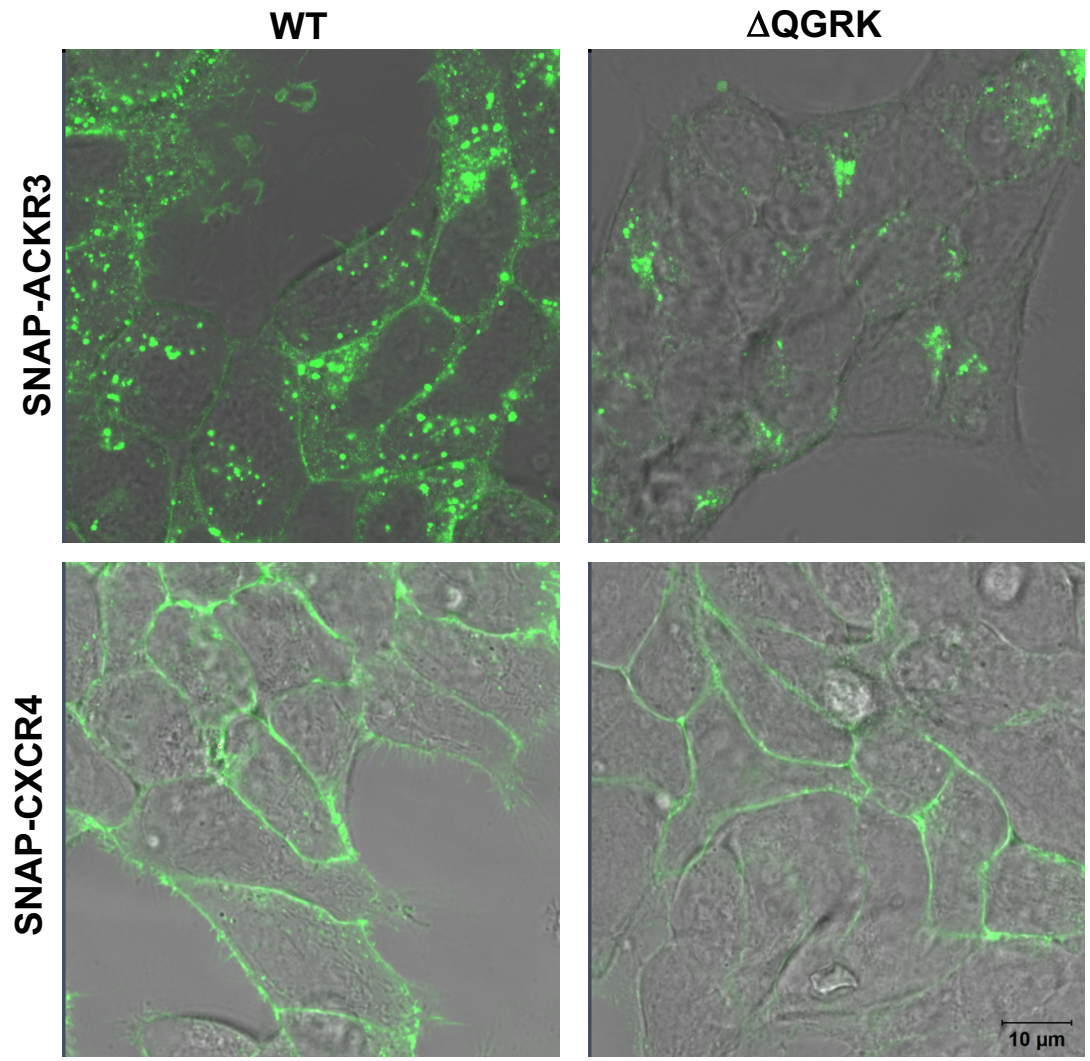

Figure 5.2: Distribution of SNAP-CXCR4 and SNAP-ACKR3 receptor upon GRK depletion. *The SNAP-tagged receptors were labelled with 1 µM SNAP Surface Alexa 488 for 30 minutes at RT. Representative images are shown fluorescence 488 channel overlayed on brightfield from 3 independent experiments. Images were captured with 40x water objective, 3x zoom on Zeiss LSM 880 confocal microscope. Scale bar = 10 µm.*

5.3.2. Assessment of CXCR4 and ACKR3 Co-localisation with Early Endosome Markers

In order to identify the compartment in which the ACKR3 was trafficked to in the ΔQGRK cells, we used confocal microscopy with a series of fluorescently tagged compartment markers. Initially, to evaluate whether ACKR3 had translocated to early endosomes upon deletion of GRKs, we assessed co-localisation of the SNAP-labelled receptor with an RFP-tagged early endosomal marker using confocal microscopy (Figure 5.3/A). To establish the assay pipeline and as a positive control, we used HEKG SNAP-CXCR4 cells incubated with vehicle or 10 nM CXCL12, as CXCR4 has been previously shown to internalise upon CXCL12 stimulation to early endosomes [130]. The representative images in Figure 5.3 show the SNAP-Surface Alexa 488 labelled CXCR4 receptor in yellow, the early endosome marker in magenta, with co-localisation shown in white. Images were segmented via the Squassh plug-in in Image J, and co-localisation (signal) of the receptor with the early endosomes was quantified and the fold change in response to CXCL12 was calculated. Stimulation with 10 nM CXCL12 for 10 minutes at 37℃ resulted in a 3.97 ± 1.01-fold increase (n=20 cells from 3 individual experiments, p=0.009) in CXCR4 associated with early endosome (EE) compared to vehicle (Figure 5.3/B). This confirmed the suitability of this imaging protocol to measure the localisation of proteins within early endosomes.

Following that, ACKR3 co-localisation with early endosomes was assessed in the HEK293 SNAP-ACKR3 and HEK293 ΔQGRK SNAP-ACKR3 cell lines under basal, unstimulated, conditions to investigate the change of localisation of the receptor upon GRK depletion. The representative images in Figure 5.4/A show the SNAP-Surface Alexa 488 labelled ACKR3 receptor in yellow, the early endosome marker in magenta and the co-localisation is shown in white spots. Both the ‘wide type’ and quadruple GRK KO cells show partial co-localisation with the endosomal marker. Co-localisation was quantified by using the Squassh plug-in as above. The ΔQGRK SNAP-ACKR3 cells showed 19.5 $\pm$ 2.5 % of receptor co-localisation with the early endosome marker (n=38 cells from 4 individual experiments), which was not significantly different from

the WT SNAP-ACKR3 cells (23.9 ± 2.0 %, n=36 cells from 3 individual experiments, p=0.177). These data suggest that ACKR3 localisation within early endosomes does not change upon depletion of GRKs.

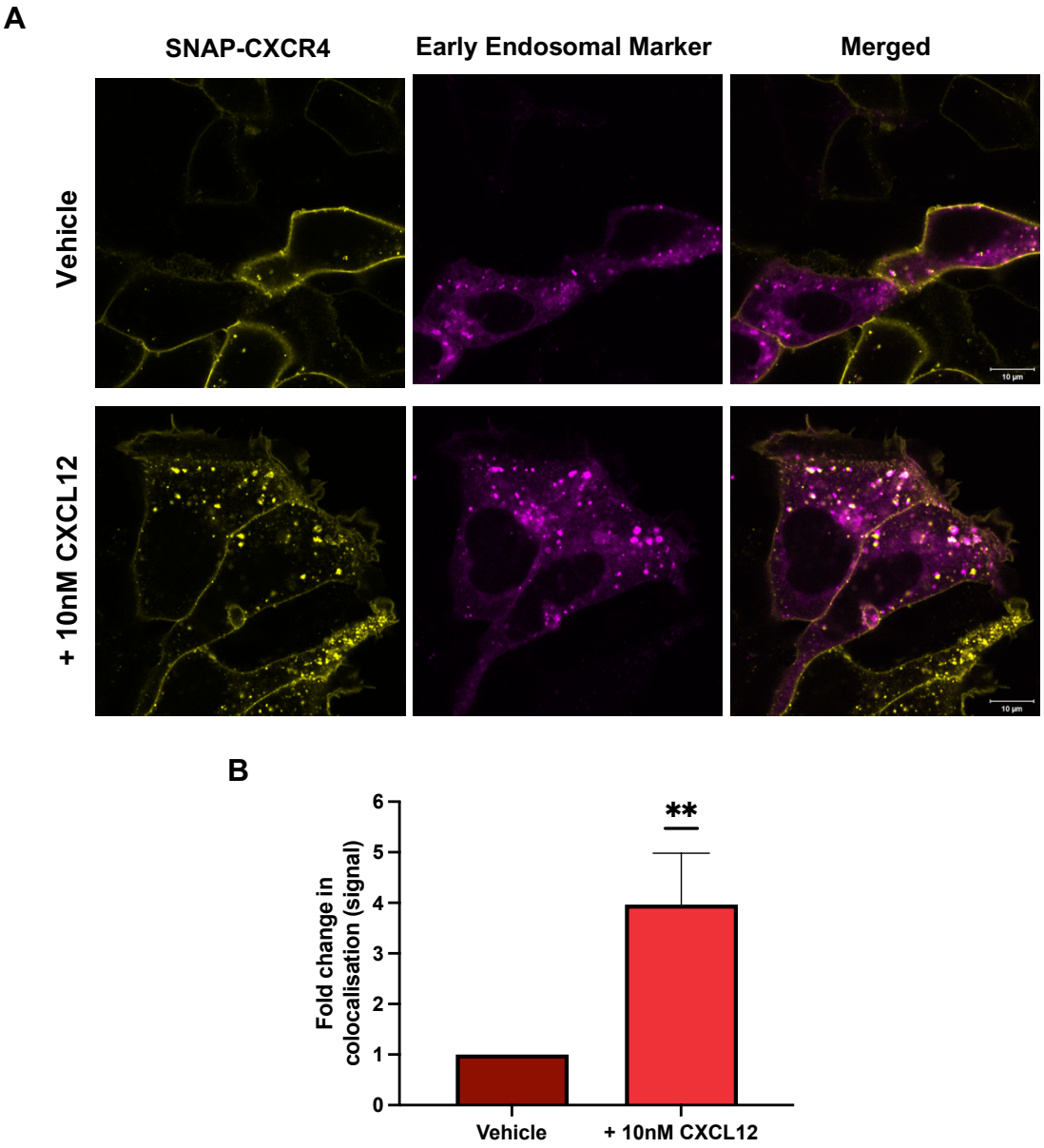

Figure 5.3: CXCR4 co-localisation with early endosomal marker upon stimulation with CXCL12. A: *Representative images of SNAP-CXCR4 in HEKG cells treated with vehicle or 10 nM CXCL12. SNAP-CXCR4 was labelled with 500 nM SNAP Surface Alexa 488 (yellow), and early endosomes were stained with CellLight™ Early Endosomal Marker (magenta). Images were taken 3x zoom, 40x water objective on Zeiss LSM 880 confocal microscope. Scale bar = 10 µm.* ***B:*** *Fold change in co-localisation signal of CXCR4 with early endosomes, n=20 cells from 3 individual experiments (One sample t-test, **p<0.01, error bars =SEM). Co-localisation signal analysed in Squassh plug in (Image J).*

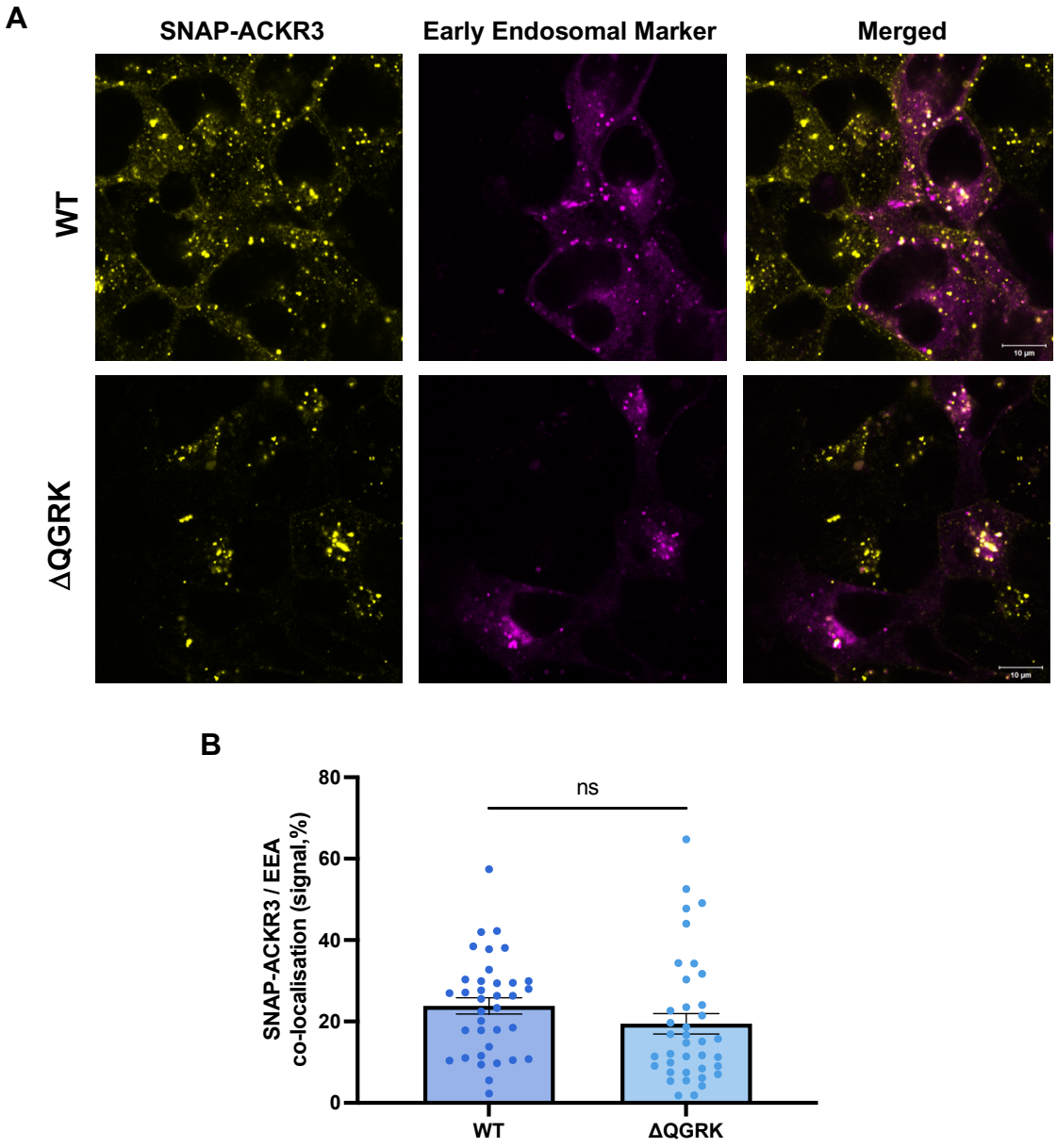

Figure 5.4: ACKR3 co-localisation with early endosomal marker. A: *Representative images of SNAP-ACKR3 in WT and ΔQGRK SNAP-ACKR3 cells in basal conditions. SNAP-ACKR3 was labelled with 500 nM SNAP Surface Alexa 488 (yellow), and early endosomes were stained with CellLight™ Early Endosomal Marker (magenta). Images were taken with 3x zoom and 40x water objective on a Zeiss LSM 880 confocal microscope. Scale bar=10 μm.* ***B:*** *Co-localisation (signal) of SNAP-ACKR3 in with early endosomal marker WT or ΔQGRK cells n=36-38 cells from a minimum of 3 individual experiments, Error bar =SEM. Student's unpaired t-test). Co-localisation signal analysed in Squassh plug in (Image J).*

5.3.3. ACKR3 Co-localisation with Lysosomes Upon GRK Depletion

To further assess the effect of quadruple GRK KO on SNAP-ACKR3 distribution, similar co-localisation experiments were performed in WT and ΔQGRK cells using an antibody against the lysosome marker, LAMP-1, confocal microscopy and Squassh analysis. The SNAP-ACKR3 receptor was labelled with SNAP Surface Alexa 549 (Figure 5.5/A, magenta), and lysosomes were detected using LAMP-1 SNAP Alexa 488 antibody (Figure 5.5/A, yellow). Additionally, the cell nucleus was stained using 1 μM Hoechst33342 (Figure 5.5/A, blue). In WT cells, co-localisation of ACKR3 pixels with the LAMP-1 marker was 10.5 ± 1.3 %, while the depletion of all four GRK isoforms resulted in a significant increase of such co-localisation, with 46.3 ± 2.8 % co-localisation in ΔQGRK cells (n=36-40 cells from a minimum of 3 individual experiments, $p<0.0001$; Figure 5.5/B) suggesting a greater ACKR3 localisation in lysosomal vesicles in the absence of GRKs. These data reveal a possible role for GRKs in ACKR3 fate post-internalisation.

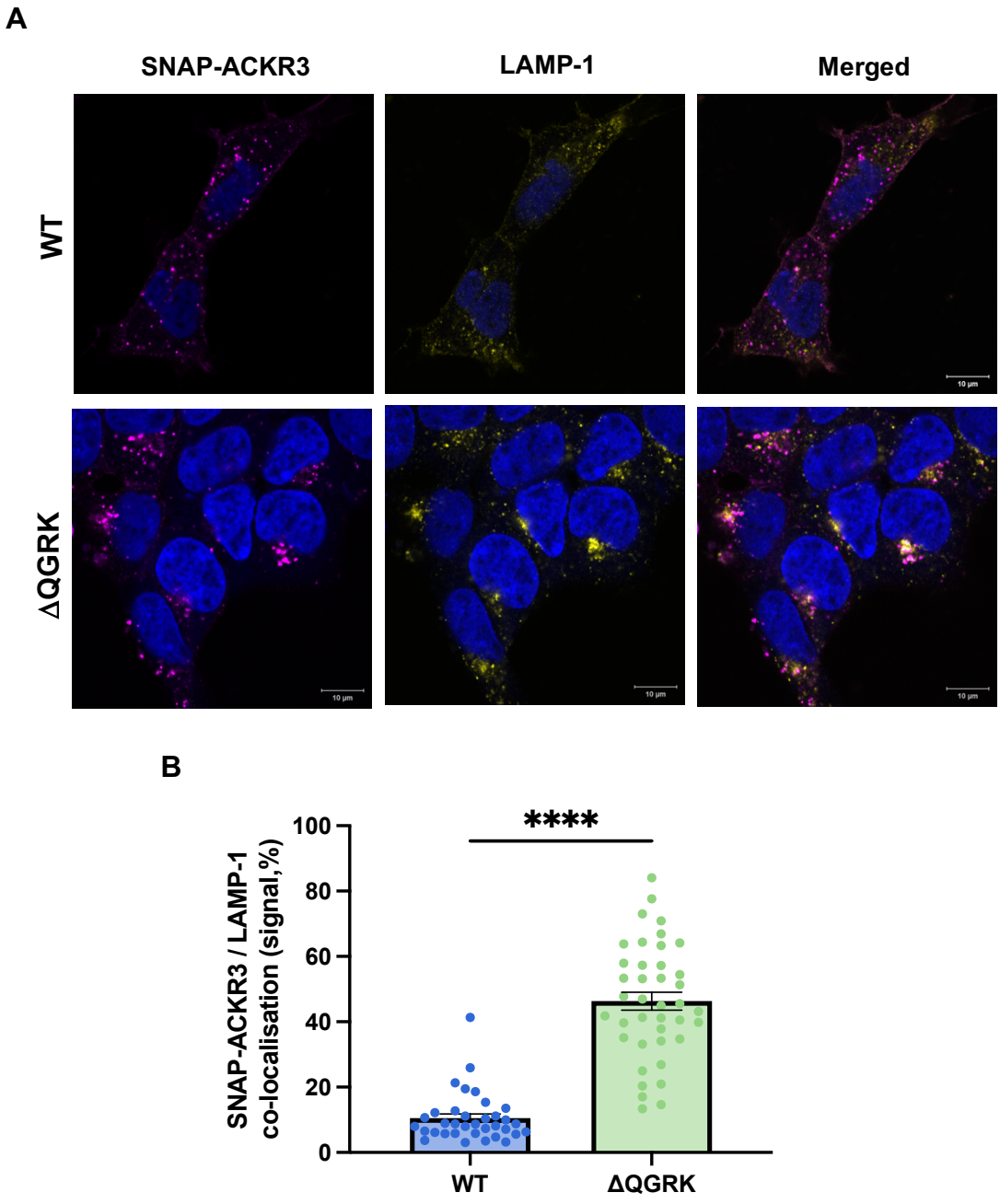

Figure 5.5: ACKR3 co-localisation with lysosome marker LAMP-1. A: *Representative images of SNAP-ACKR3 in WT or and ΔQGRK cells. SNAP-ACKR3 was labelled with 500 nM SNAP Surface Alexa 549 (magenta), and lysosomes were detected using LAMP-1 Alexa Flour™ 488 antibody (yellow). Images were taken with 3x zoom and 40x water objective on a Zeiss LSM 880 confocal microscope. Scale bar = 10 µm* ***B:*** *Quantification of Co-localisation (signal) of SNAP-ACKR3 with lysosomes LAMP-1 (n=36-40 cells from a minimum of 3 individual experiments; Student's unpaired t-test ****P < 0.0001). The co-localisation signal was analysed in Squassh plug-in (Image J). Error bar = SEM.*

5.3.4. ACKR3 Distribution Upon GRK2/3 or GRK5/6 Depletion

Following the observation that ACKR3 co-localisation with lysosomes increased upon full GRK isoform depletion, based on GRK subfamilies, double GRK KO cells were created to get a more in-depth understanding of the contribution of different GRK isoforms in ACKR3 distribution after internalisation. Mixed-population stable cell lines were created with SNAP-ACKR3 in a HEK293 ΔGRK2/3 and HEK293 ΔGRK5/6 background. ACKR3 expression and distribution in these cell lines in basal, unstimulated, conditions were assessed using 500 nM SNAP Surface Alexa 549 and confocal imaging (Figure 5.6).

In the HEK293 ΔGRK2/3 SNAP-ACKR3 cell line, SNAP-labelled ACKR3 showed intracellular localisation with a minimal amount of receptor on the plasma membrane, although the receptor appears to be distributed diversely in smaller punctate, as opposed to the ΔQGRK SNAP-ACKR3 cells, where the intracellular vesicles demonstrated a more localised distribution n larger punctate. Interestingly, in the ΔGRK5/6 SNAP-ACKR3 cells, the receptor showed partial membrane localisation; however, there were still a significant amount of intracellular bright vesicles containing receptors. These images suggest more receptor localisation at the plasma membrane upon GRK5/6 depletion, while GRK2/3 depletion resulted in pre-dominantly intracellular ACKR3 localisation. This might indicate a partial role of GRK5 and GRK6 in constitutive ACKR3 receptor internalisation while absence of GRK2 and GRK3 doesn’t seem to affect receptor distribution.

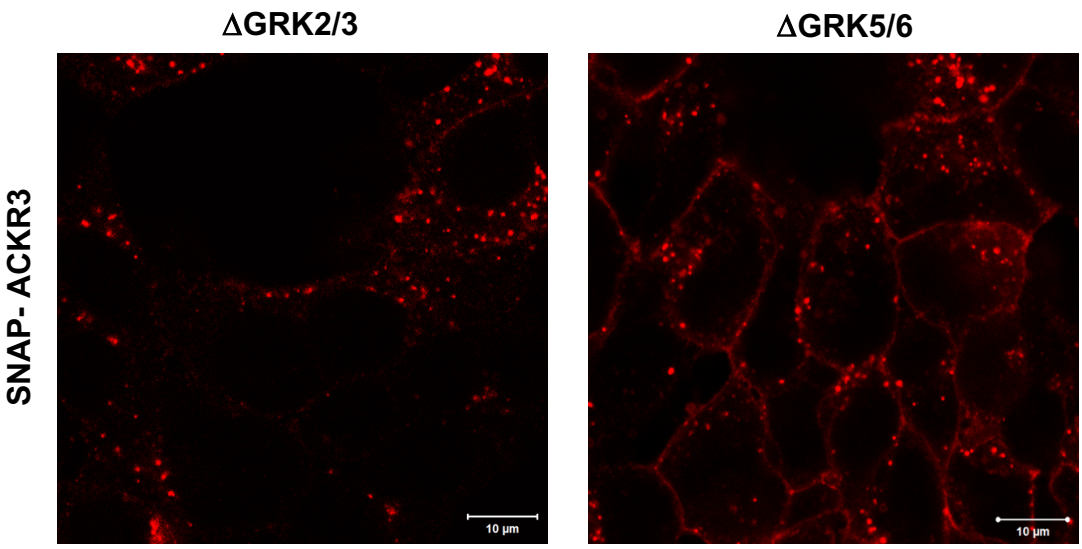

Figure 5.6: Distribution and localisation of SNAP-ACKR3 upon GRK 2/3 or GRK 5/6 depletion. *The HEK 293 ΔGRK2/3 SNAP-ACKR3 and HEK 293 ΔGRK5/6 SNAP-ACKR3 cells were labelled with 500 nM SNAP Surface Alexa 549 (30 minutes). Scale bar = 10 µm. Representative images (n=6 images per cell line from 3 independent experiments) were captured with Zoom 3x, 40x water objective on a Zeiss LSM 880 confocal microscope.*

To further assess the different effects of the GRK2/3 and GRK5/6 pairs on ACKR3 localisation, we assessed the co-localisation of SNAP-ACKR3 with the lysosome marker LAMP-1 in these cell lines in basal, unstimulated conditions (Figure 5.7). The double GRK KO data was also compared to the co-localisation data from WT and ΔQGRK cell lines obtained above.

Quantification of the SNAP-ACKR3 co-localisation with LAMP-1 is shown in Figure 5.8. Both, ΔGRK2/3 and ΔGRK5/6 cells showed significantly increased ACKR3 co-localisation with LAMP-1 compared to 'WT' cells (20.9 ± 2.1 %, n=32 cells from 4 individual experiments for ΔGRK2/3; 18.9619.0 ± 1.9%, n=29 cells from 3 individual experiments for ΔGRK5/6 and 10.5±1.3 %, n=33 cells from 3 individual experiments for WT); (one-way ANOVA multiple comparison to ACKR3 (WT), two-sided Dunett's test, ΔGRK2/3 vs WT p=0.0099, ΔGRK5/6 vs WT p=0.0385). Thus, the dual GRK KO cells, expressing only one family of GRKs, showed around half the co-localisation with LAMP-1 compared to the quadruple GRK KO cell line. These data suggest that both GRK families, GRK2/3 and GRK5/6, are partially involved in the increased lysosome localisation of ACKR3.

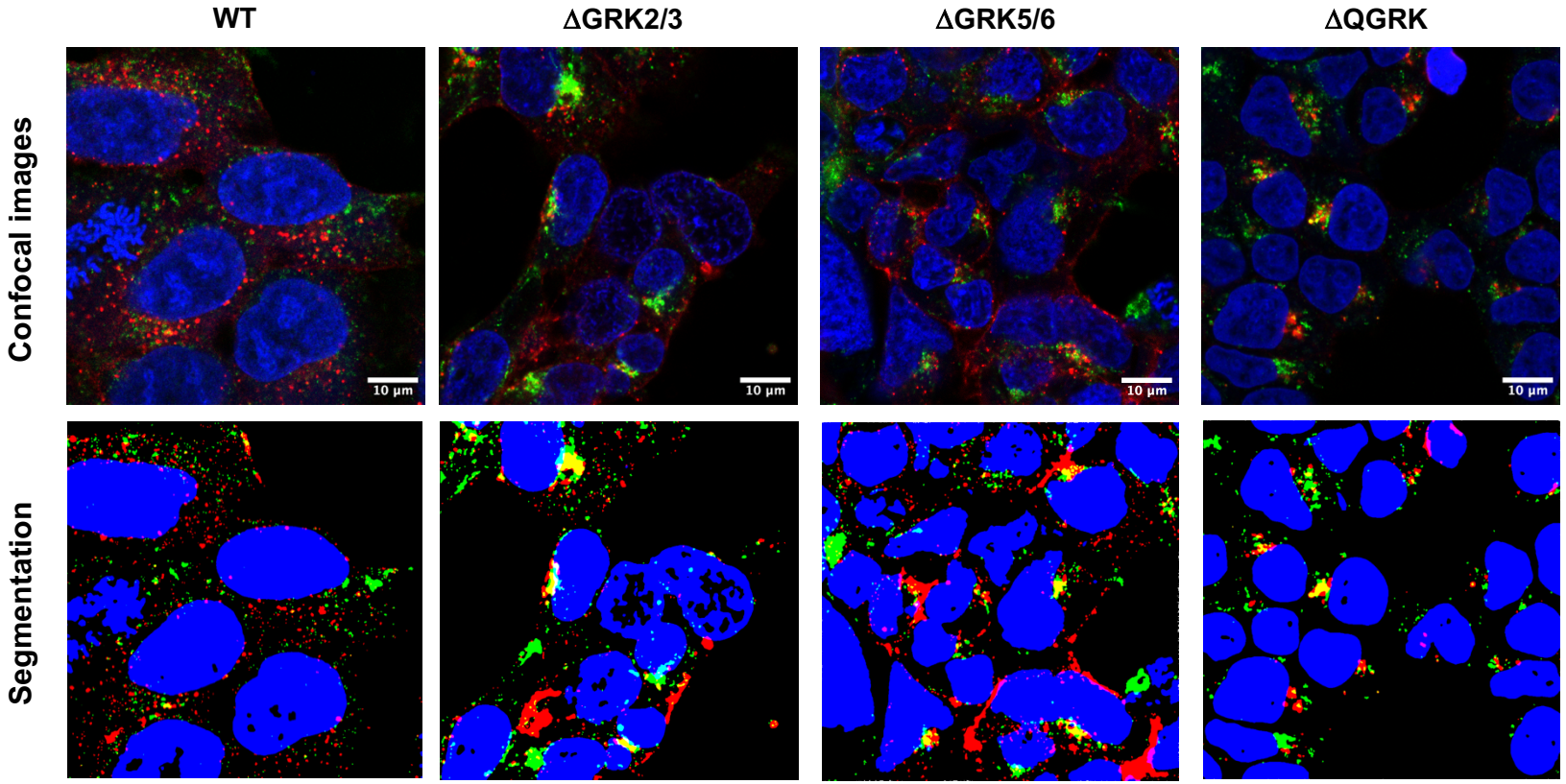

Figure 5.7: Effect of family GRK knock-out on ACKR3 co-localisation with lysosomal marker LAMP-1. *Representative confocal images (left) and their segmentation by Image J Squassh plug-in (right) for HEK293 SNAP-ACKR3, ΔGRK2/3 SNAP-ACKR3, ΔGRK5/6 SNAP-ACKR3 and ΔQGRK SNAP-ACKR3 cell lines in basal, unstimulated, conditions. The receptor was labelled with 500 nM SNAP Surface Alexa 549 (red), and lysosomes were detected with LAMP-1 Alexa Fluor™ 488 antibody (green). ACKR3 co-localisation with the lysosome marker is shown in yellow. Images were taken with 3x zoom and 40x water objective on a Zeiss LSM 880 confocal microscope. Scale bar = 10 µm.*

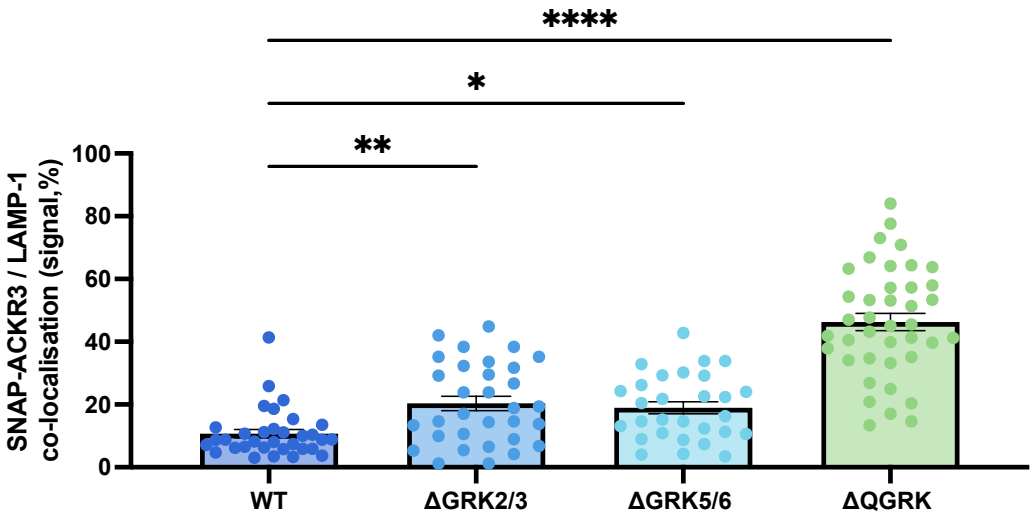

Figure 5.8: Effect of family GRK knock-out on ACKR3 co-localisation with lysosomal marker LAMP-1. *Co-localisation (signal) of the receptor with LAMP-1 marker. n=29-40 cells from a minimum of 3 individual experiments; one-way ANOVA followed by two-sided Dunett's comparisons test was performed if P < 0.05 significant; *P < 0.05, **P < 0.01, ****P <0.0001). Error bar = SEM.*

To ensure that the increased SNAP-ACKR3/LAMP-1 co-localisation signal in the GRK KO cells was not due to increased expression of SNAP-ACKR3 or LAMP-1, an alternative analysis of the data was carried out, and the average LAMP-1 and SNAP-ACKR3 fluorescence intensity per cell was calculated. The cell count number per image was obtained from the Hoechst33342 stained cells (Figure 5.9/A). The average intensity per cell was calculated by taking the intensity of the whole field of view (Figure 5.9/B) divided by the cell count from the corresponding image. The average LAMP-1 intensity per cell showed no difference between the WT (1.55 ± 0.15) and the double GRK KO cells: ΔGRK2/3 (1.19 ± 0.26), ΔGRK5/6 (1.37 ± 0.21) and ΔQGRK (1.06 ± 0.09) (Figure 5.9/C).

The average SNAP-ACKR3 intensity per cell was significantly lower in ΔGRK2/3 cells (1.04 ± 0.25) and ΔQGRK (0.24 ± 0.02) cells compared to WT (1.97 ± 0.27), while it was not statistically different for ΔGRK5/6 cells (1.62 ± 0.22) (Figure 5.10). This data supports that the changes in the co-localisation signal arise from the redistribution of ACKR3, not a change in the expression of the receptor or the marker upon GRK deletion.

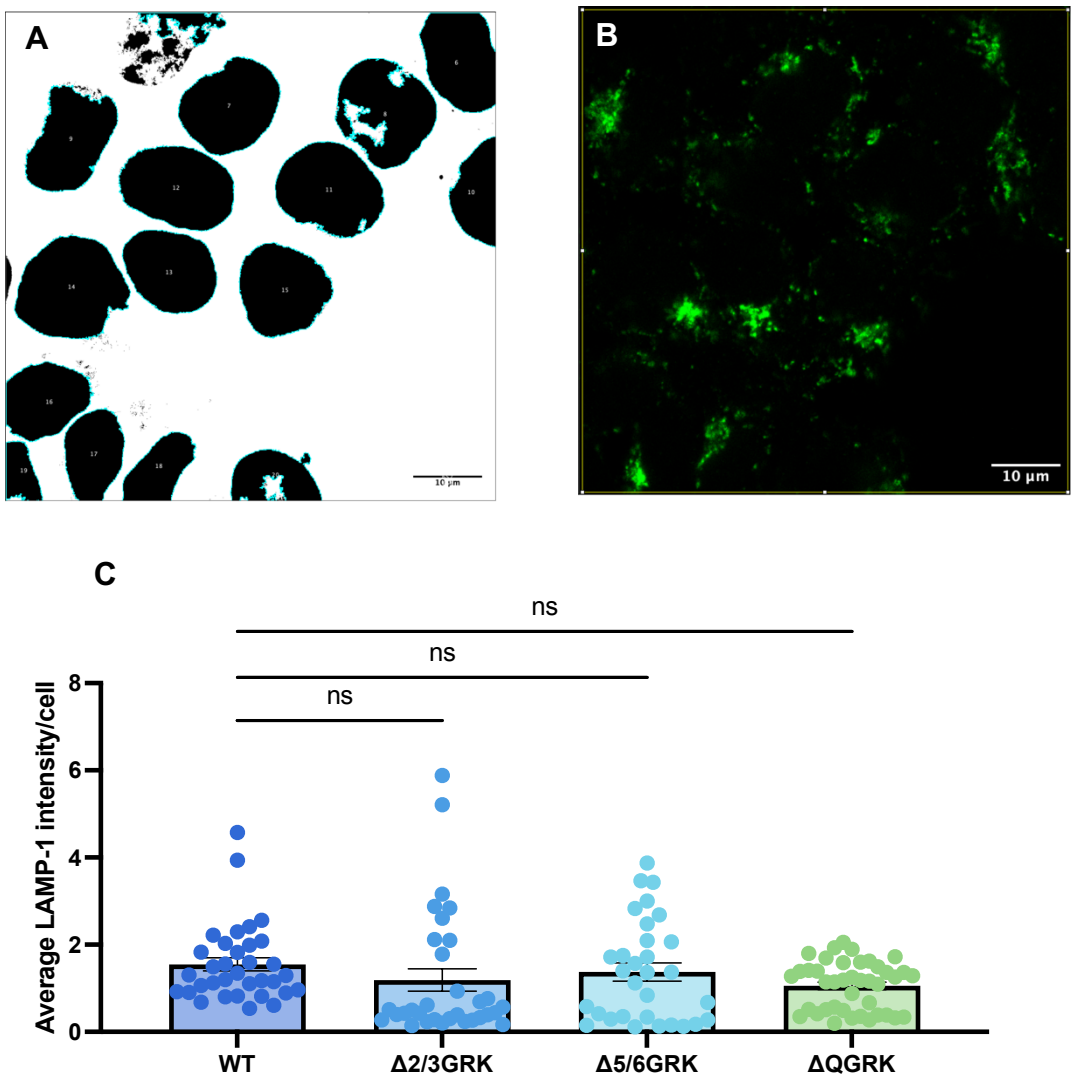

Figure 5.9: LAMP-1 marker intensity per cell upon GRK depletion. *The average LAMP-1 intensity per cell was calculated in Fiji.* ***A:*** *A binary mask of the Hoechst33342 stained cells was used for cell count.* ***B:*** *The average intensity of the LAMP-1 channel was measured by selecting the whole field of view rectangle ROI. Scale bar = 10 µm.* ***C:*** *Average LAMP-1 intensity/cell upon GRK depletion compared to WT, n=29-40 cells from a minimum of 3 experiments (one-way ANOVA followed by two-side Dunett's comparisons test; P < 0.05 significant). Error bar = SEM.*

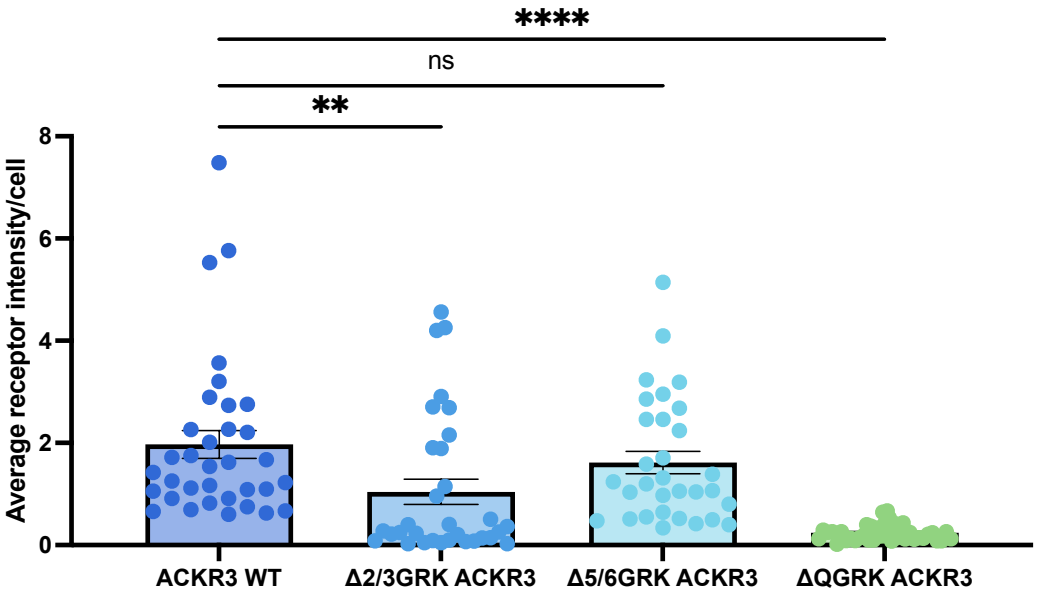

Figure 5.10: SNAP-AlexaFluor 594 intensity per cell upon GRK depletion. *The average receptor intensity per cell was calculated in Fiji. Average receptor intensity/cell upon GRK depletion compared to WT, n=29-40 cells from a minimum of 3 experiments (one-way ANOVA followed by two-sided Dunett's comparisons test was performed if P<0.05 significant; **p<0.01, ****p<0.0001). Error bar = SEM.*

5.4 Discussion

In this chapter, we show that the ACKR3 receptor was still constitutively internalised in the absence of all GRK isoforms. We observed different intracellular distributions of ACKR3 receptors in the ΔQGRK SNAP-ACKR3 compared to wild-type receptors. Additionally, we further investigated the intracellular localisation of ACKR3 upon GRK depletion using a co-localisation imaging assay with early endosomal and lysosomal markers. Our data shows that ACKR3 co-localisation is affected by the absence of GRKs and exhibits increased lysosomal localisation.

Our initial CXCR4 data show that under basal conditions, CXCR4 is found primarily at the plasma membrane in both WT and quadruple GRK KO cells. These CXCR4 images align with previous studies that show that the limited constitutive internalisation of CXCR4 may not require GRKs and arrestin [181, 182]. In contrast, ACKR3 showed continuous recycling and no difference in internalisation with a predominantly intracellular location in both WT and quadruple GRK KO cells. It is important to mention that the SNAP-tagged receptor was labelled with membrane-impermeable SNAP dye, allowing visualisation of only the receptors originating at the cell surface and subsequently internalised. Consequently, it might be possible that some proportion of the intracellular ACKR3 receptor remained unobservable.

Our findings are consistent with a recently published study from Schafer et al., which observed no difference in ACKR3 internalisation in wide type versus ΔGRK2/3/5/6 cells measured by an anti-ACKR3 antibody 'prelabelled' flow cytometry experiment. They used a fluorescence secondary stain to measure the fluorescence intensity obtained from surface labelling at 37℃ and compared it to the 4℃ condition. This same study also showed that mutation of the distal, proximal and terminal phosphorylation sites of ACKR3 with the triple cluster phosphorylation mutation (ΔPDT) had no effect on such constitutive endocytosis [187]. Similarly, another study has also observed constitutive internalisation of an HA-ACKR3 ST/A mutant (in which the serine/threonine residues of all the potential C-terminal phosphorylation sites

were mutated to alanine), which further agrees with the fact that the ACKR3 constitutive endocytosis is likely to be phosphorylation independent [186].

As mentioned in the introduction above, studies with other GPCRs have suggested a distinct endocytic pathway for constitutive vs ligand-induced internalisation [180]. In the case of the orphan adhesion receptor ADGRA3, constitutive internalisation is not affected by the absence of β-arrestin1/2; however, it is clathrin-dependent [188]. Similarly, constitutive internalisation of the protease-activated receptor 1 (PAR1) occurs independently of β-arrestin, through a clathrin and dynamin-dependent way [189]. Based on this, we also made a preliminary assessment of ACKR3 localisation upon the addition of the dynamin inhibitor Dyngo (1 μM) (Thermo Fisher Scientific), to investigate the dependence of ACKR3 constitutive internalisation on dynamin-mediated processes. The preliminary data (Figure 5.11), showed that the ACKR3 is mainly located at the plasma membrane upon the addition of the dynamin inhibition, suggesting that ACKR3 constitutive endocytosis is dynamin-dependent; however, further repeats and validation are required, including the use of other clathrin and dynamin inhibitors such as Pitstop2 [190].

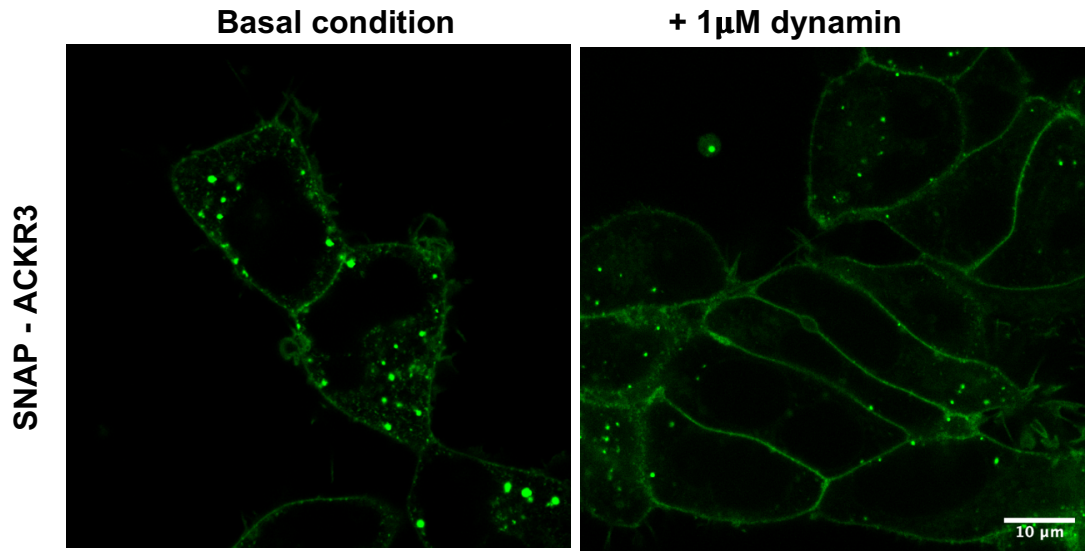

Figure 5.11: ACKR3 distribution upon dynamin inhibition. *HEK293 SNAP-ACKR3 cells were treated with 1μM dynamin inhibitor (30 minutes prior and during SNAP labelling with 1μM SNAP Surface Alexa 488 for 30 minutes). Scale bar = 10 μm. Images were taken with an LSM 880 confocal microscope, 40x water objective, and zoom 3x. Preliminary data of n=1 experiment.*

Following the generation of HEK293 ΔQGRK SNAP-ACKR3 cells, the ability of ACKR3 to recruit β-arrestin recruitment was assessed using a (K-ras) BRET assay. The data showed that in the absence of all GRK isoforms, ACKR3, following activation with CXCL12, is unable to recruit β-arrestin2. However, this effect was rescued upon the reintroduction of GRK2. This indicated that the β-arrestin recruitment of ACKR3 requires the presence of GRK. Drube et al. have shown similar results with other GPCRs, where they observed a significant reduction in β-arrestin1/2 recruitment upon quadruple GRK KO and a rescue of this effect upon overexpression of GRKs, regardless of the specific isoform transfected [95]. A preprint publication from the same group suggests that ACKR3 is GRK 5/6 regulated [191], although it can be modulated by other GRKs, upon overexpression in transfected systems. Based on these findings, β-arrestin recruitment rescued by GRK2 might be a result of the increased availability of GRK2 due to its overexpression. While it cannot be definitively concluded which GRK isoform regulates ACKR3, nevertheless, the data does demonstrate that β-arrestin recruitment of activated ACKR3 requires GRKs. It would be beneficial to create single or triple GRK knock-out cell lines which stably express ACKR3 to investigate the effect of individual GRK isoforms on the recruitment of β-arrestin2 to ACKR3.

While the depletion of GRKs did not inhibit the ACKR3 constitutive internalisation, the receptor displayed a distinct intracellular localisation in the ΔQGRK cell line. The ΔQGRK SNAP-ACKR3 cells displayed larger intracellular vesicles with a more localized and uneven distribution, in contrast to the wild-type ACKR3, which demonstrated a more dispersed distribution within smaller-sized vesicles. Based on these, we wanted to further investigate this atypical intracellular distribution and the effect of GRKs on ACKR3 intracellular localisation with co-localisation imaging assays.

The ability of this imaging and co-localisation assay to detect receptors in early endosomes was confirmed by imaging CXCR4 in unstimulated versus CXCL12 stimulated conditions, showing that upon CXCL12 activation, CXCR4 internalises into early endosomes as previously described [130, 192]. As

previous evidence suggested that upon CXCL12 activation, ACKR3 quickly relocalises to the early endosomes [73] we aimed to assess co-localisation of ACKR3 with early endosomes in basal condition and any alterations resulting from GRK depletion. Our results show no significant changes in ACKR3 co-localisation with early endosomes in the absence of GRKs. These data suggest that GRKs have no role in ACKR3 internalisation and trafficking to early endosomal vesicles from the cell surface. These results align with previously mentioned phosphomutant studies where there was no effect in constitutive endocytosis compared to WT [186, 187].

We conducted further investigation into the modified subcellular location of ACKR3 upon GRKs and the potential involvement of GRKs in ACKR3 trafficking following early endosomes. Since GRKs are suggested to play a role in GPCR desensitisation and degradation [37, 74, 193], we aimed to determine whether GRKs are relevant to ACKR3 trafficking towards the lysosomal pathway. We then assessed the receptor co-localisation with lysosomes was altered using LAMP-1 lysosomal marker. We examined whether there is any alteration in receptor co-localisation with lysosomes in the absenve of GRKs using the LAMP-1 lysosomal marker. The data indicated a significant increase of ACKR3 co-localisation with lysosomes in the ΔQGRK cell line compared to WT cells, with the double KO cell lines showing a significant but partial increase in co-localisation. These data suggest that in the absence of any GRK isoform pairs, ACKR3 is trafficked more towards the lysosomes. This indicated that GRKs may either redirect the receptor away from lysosomes or promote its recycling from early endosomes via recycling compartments. This result proposes a potential role of GRKs in the continuous recycling of ACKR3 to the plasma membrane, which leads to increased degradation when GRKs are depleted. While there is no previous observation of the GRK effect in ACKR3 degradation and recycling in basal conditions, previous studies with CXCL12-activated ACKR3 described the importance of C-tail phosphorylation for receptor recycling instead of degradation [194]. While previous studies have identified the involvement of GRK, specifically GRK6, in the degradation of CXCR4, these results suggest that CXCR4 degradation is reduced in the absence of GRKs; hence it is essential for

lysosomal degradation [74]. These findings suggest a potential role for GRK in intracellular trafficking for both CXCR4 and ACKR3. However, they suggest a distinct effect: GRKs might promote ACKR3 recycling, while some GRK isoforms are suggested to promote degradation in CXCR4.

The work presented above, while interesting, requires further experimentation. For example, it would be valuable to further investigate the role of GRKs in ACKR3 constitutive trafficking post-internalisation. Assessing the SNAP-tagged ACKR3 co-localisation with the recycling endosome marker Rab 11 [195] would provide information about potential differences in receptor recycling upon GRK depletion. More in-depth investigation of receptor co-localisation with other markers, such as late endosomal markers and other lysosomal markers [196], would also give the opportunity to get a more detailed picture of the GRK involvement in ACKR3 trafficking. Additionally, the work presented in this chapter has evaluated the localisation of ACKR3 in basal conditions, the distinct endocytosis and trafficking of the CXCL12-activated ACKR3 remain to be assessed. While a recent study suggested that the ligand-induced internalisation of ACKR3 requires GRKs, our preliminary data imaging ΔQGRK SNAP-ACKR3 cells in the presence of CXCL12 suggested differently (Figure 5.12). The activated ACKR3 is localised mainly in intracellular compartments in the absence of GRKs. However, the distribution seems to be different than the basal condition. Further assessment with markers and using different variants of GRK KO cell lines could provide valuable information about the CXCL12-induced trafficking of ACKR3.

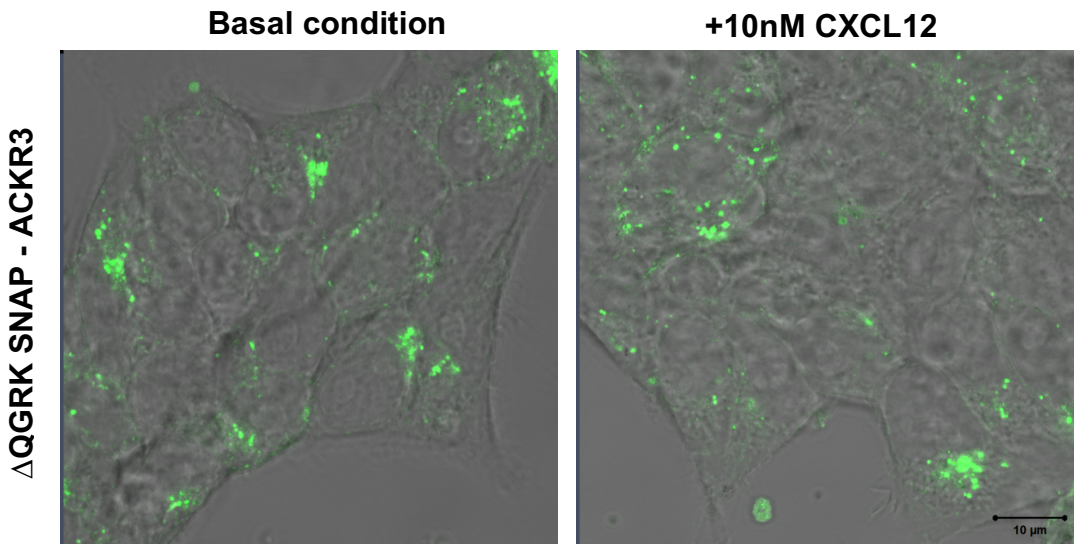

Figure 5.12: Distribution of ACKR3 upon GRK depletion in basal and CXCL12-activated conditions. *Cells were labelled with SNAP Surface Alexa 488 and some wells were treated with 10 nM CXCL12. Scale bar = 10 µm. Images were taken on LSM 880 confocal microscope, 40x water objective with Zoom 3x. Preliminary data of n=2 individual experiment.*

In various tumours, such as breast and brain tumours, ACKR3 is overexpressed and plays a role in tumour angiogenesis and tumour cell proliferation [197]. Numerous previous studies also described changes in the expression of GRKs in cancer [198]. A study showed a connection between GRK2 activity and expression level and breast cancer progression [199]. GRK3 involvement was also shown in breast cancer and indicated that it might regulate CXCR4 activation and chemotaxis [200]. GRK6 also presented various roles in different tumour types. In medulloblastoma cells, GRK6 activity showed increased cell migration via promoting activation of CXCR4 [201], while in lung cancer, GRK6 depletion resulted in increased tumour metastasis [202]. Based on our results proposing GRK involvement in the post-internalisation trafficking of ACKR3 and previous findings showing an ACKR3 role and GRK role in multiple cancer types, investigation of the effect of GRKs on ACKR3 in the tumour environment would provide crucial information about their potential involvement in cancer progression.

The discovery of extracellular vesicles (EV) added another layer to GPCR trafficking and signalling [203]. Bebelman et al. also described the increased secretion of extracellular vesicles (EV) in cancer cells, suggesting that these

altered EVs might have a role in cancer progression, such as angiogenesis and metastasis [204]. As ACKR3 is presented to have a role in cancer progression, it might raise the question of whether ACKR3 is secreted in EVs and the possible involvement of GRK in the EV trafficking of ACKR3. A collaborator, Caitrin Crudden (Vrije Universiteit Amsterdam), whose research area is extracellular vesicles and their role in cancer cell signalling, conducted a test on HEK 293 SNAP-ACKR3 and HEK 293 ΔQGRK SNAP-ACKR3 to see if there was a difference in ACKR3 EV secretion upon GRK depletion. The preliminary data showed reduced EV secretion in the absence of GRKs. However, the ΔQGRK cells released relatively more ACKR3 on their EV, suggesting an increased localisation in lysosomal compartments aligning with our findings. This preliminary finding suggests ACKR3 is present in EV and also possible GRK involvement in that trafficking process. Although this data is interesting, further investigation is required with endogenous and cancer cell backgrounds.

Finally, conducting more broad research involving other atypical chemokine receptors would provide valuable insight into whether the observed GRK effect in our study is specific to ACKR3 or if it applies similarly to other ‘scavenger’ receptors. A recent study with ACKR2 used phosphoproteomic mapping, where they could identify dynamic phosphorylation events and study phosphoproteins unique to ACKR2. They found that GRK2 is required to inhibit ACKR2 from degradation and plays an important to regulate ACKR2 stability [205]. Their findings suggest that GRK has a similar role to what our finding showed in post-endocytosis trafficking of ACKR3 where GRK might have a preventing role from receptor degradation. This approach could be useful for further investigating the role of GRKs in preventing ACKR3 degradation and exploring the involvement of phosphosites after ACKR3 activation in the absence of GRKs.

5.5. Conclusion

Our findings suggest that ACKR3 constitutive internalisation does not require the presence of GRKs. However, complete deletion of GRK isoforms has a dramatic effect on the intracellular localisation of ACKR3 (Figure 5.13). Upon further investigation with endocytic markers, we have shown that ACKR3 localisation within early endosomal vesicles is unchanged, while receptor co-localisation with lysosomes is significantly increased upon GRK KO. This suggests a role of GRKs in ACKR3 trafficking post-internalisation. Moreover, our data showed that both GRK2/3 and GRK5/6 pairs might be involved in the modified ACKR3 localisation.

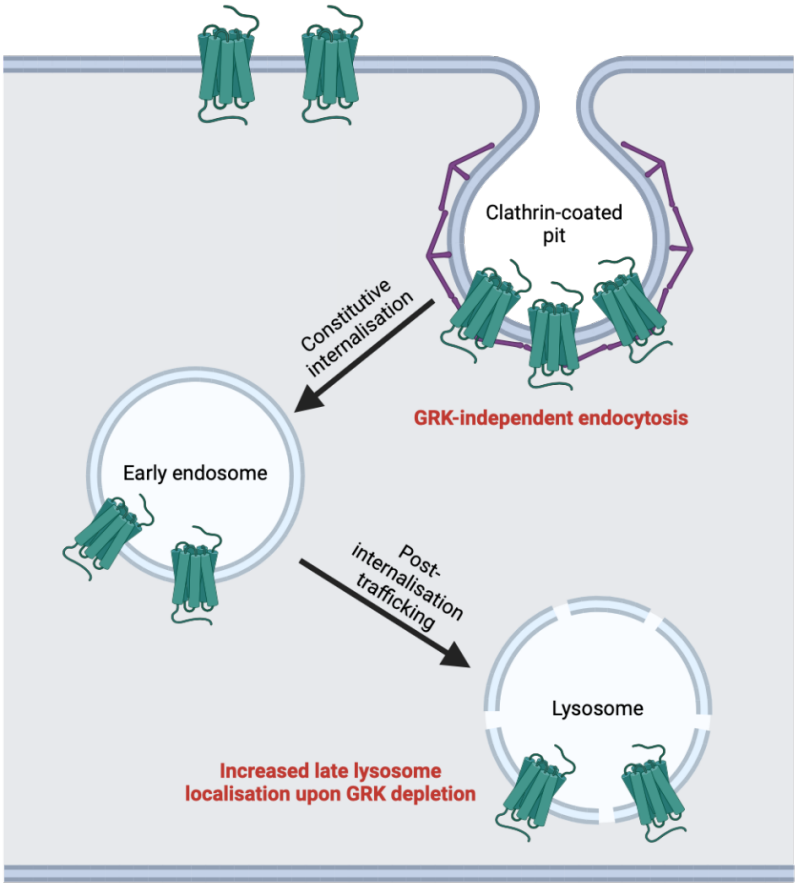

Figure 5.13: GRK role in the basal location of ACKR3 in HEK293 cells. *ACKR3 constitutive internalisation is GRK independent and GRK depletion does not change the receptor localisation with early endosomes. However, GRK KO resulted an increased lysosomal receptor localisation, suggesting a GRK involvement in ACKR3 trafficking post-internalisation. The figure was created with BioRender.com.*

Chapter 6: General Discussion

Chemokine receptor CXCR4 and atypical chemokine receptor ACKR3 are known to share the ligand CXCL12, and studies have shown their involvement in various cancers. The upregulation of ACKR3 and CXCR4 expression may promote tumour growth and contribute to cancer proliferation and metastasis [64]. However, their signalling differs greatly as CXCR4 signals canonically through G proteins, while ACKR3 does not couple to G proteins [206]. Although there is growing data on their signalling, structure, and role in different pathophysiological conditions, there are still gaps in the understanding of their spatiotemporal dynamics at the plasma membrane, despite its relevance to downstream signalling and regulation. Advanced spectroscopy techniques have previously been used to study the dynamics of other GPCRs [76, 77]. This thesis aimed to assess the dynamics and organisation of CXCR4 and ACKR3 at the plasma membrane. Moreover, it aimed to provide insight into the involvement of GRK in ACKR3 subcellular localisation.

Chapter 3 explored CXCR4 receptor dynamics and organisation at the plasma membrane in HEK G SNAP-CXCR4 cells, using confocal microscopy, fluorescence correlation spectroscopy (FCS) and fluorescence recovery after photobleaching (FRAP) techniques. This chapter also assessed the impact of agonist CXCL12 and antagonist IT1t on the dynamics of CXCR4. FCS revealed no significant changes in the CXCR4 diffusion coefficient and receptor density at the plasma membrane after stimulation with CXCL12 and IT1t. However, photon counting histogram (PCH) analysis suggested a change in the oligomeric state of CXCR4, indicating cluster formation upon CXCL12 addition. FRAP analysis also presented no significant changes in diffusion parameters, while the data suggested reduced receptor mobility upon both agonist and antagonist stimulation. Altogether, our data support the classical view that CXCR4 is primarily localised at the cell membrane, and upon CXCL12 stimulation, a proportion of CXCR4 is internalised.

Chapter 4 focused on the dynamics and organisation of ACKR3 at the plasma membrane, which was studied in HEK293 SNAP-ACKR3 cells using confocal microscopy, FCS, FRAP and raster image correlation spectroscopy (RICS). Due to ACKR3's known continuous recycling, assessing ***its*** dynamics at the

membrane was anticipated to be challenging and, indeed, required substantial additional optimisation to obtain meaningful data. In agreement with previous studies, confocal imaging revealed predominantly intracellular localisation of ACKR3, which remained unchanged upon CXCL12 addition. The ACKR3 dynamics on the nano and micro scales assessed with FCS and FRAP showed a significant slowdown in receptor diffusion following CXCL12 stimulation and presented reduced receptor mobility. However, RICS analysis at the macro scale indicated no ligand-induced changes in diffusion. Nonetheless, brightness data suggested cluster formation of ACKR3 in both basal and CXCL12 conditions compared to monomer and dimer controls.

In ***Chapter 5,*** we elaborated on an interesting discovery showing unusual distribution of AKCR3 upon GRK KO and used HEK293 ΔQGRK SNAP-ACKR3 cells to investigate the role of GRKs in ACKR3 distribution using confocal imaging and co-localisation imaging assays. Confocal imaging data showed that the constitutive internalisation of ACKR3 does not require the presence of GRKs. However, the depletion of GRKs had a significant effect on the intracellular location of ACKR3. Co-localisation imaging with early endosome marker and lysosomal marker revealed an enhanced co-localisation of ACKR3 receptor with lysosomes in the absence of GRKs. Further investigation suggested that both GRK2/3 and GRK5/6 isoform pairs might be involved in the altered location of ACKR3.

6.1. General Discussion: Membrane Organisation and Dynamics of CXCR4 and ACKR3

Our confocal imaging data confirmed that the membrane locations of the CXCR4 and ACKR3 receptors greatly differ. While CXCR4 is mainly localised at the plasma membrane, ACKR3 shows predominantly intracellular localisation. This aligns with previous findings showing that ACKR3 constitutively internalises and recycles to the plasma surface [73]. Important to note that we used membrane impermeable SNAP dye meaning in out data only detected receptors that was on the membrane at some point following SNAP labelling. Althouhg our data showed the different in the two receptor

membrane localisation and distribution, it is not providing information about the distribution of all the receptor in the cell. It would be interesting to image using cell permeable SNAP dye to provide more information about receptors not localised on the plasma membrane.

Comparing the basal dynamics data of the CXCR4 and ACKR3 collected by FCS, ACKR3 shows a significantly slower diffusion coefficient compared to CXCR4. In addition to the difference in dynamics, PCH analysis showed that approximately half of the ACKR3 cells exhibited a second brighter component. In contrast, this second component was present in only about 4% of the CXCR4 cells. This implies a different basal organisation of the two receptors at a nanoscale level, indicating a heterogeneously clustered ACKR3 population and a more homogenous CXCR4 population in a lower oligomeric state. This difference might also explain the slower receptor diffusion of ACKR3 as the dwell time of the measured species is linked to molecular mass [77], hence the clustered receptor population would present slower diffusion.

Upon CXCL12 stimulation, we observed different effects for the two receptors (Figure 6.1/FCS). While CXCR4 diffusion was unchanged upon ligand addition, ACKR3 presented a significant reduction in its diffusion coefficient. Furthermore, PCH analysis presented an increased percentage of cells with a second component in the case of CXCR4, suggesting the clustering of activated CXCR4 around the clathrin pit pre-internalisation, which aligns with the findings of a previous study focusing on the change in oligomerisation of CXCR4 [133] and also comparable to previous PCH data with μ-opioid receptor [84]. In contrast, CXCL12-activated ACKR3 1- vs 2-component distribution remained similar compared to the vehicle, which might indicate that ACKR3 does not require a change in oligomerisation for agonist-induced endocytosis or that agonist-induced endocytosis has minor contribution to the receptor oligomeric state or clustering, as basal ACKR3 is already continuously trafficking. While this difference is interesting, further validation with other techniques, such as single-molecule tracking [207] or super-resolution microscopy [208], would help clarify.

CXCR4 and ACKR3 dynamics were also assessed at a larger scale with FRAP, which provided complementary information about the diffusion on a micro-scale level as well as additional information regarding receptor mobility. In the basal condition, ACKR3 and CXCR4 showed similar microscale diffusion coefficients. However, ACKR3 revealed increased percentage of immobile receptor population compared to CXCR4. The difference in mobility and the similar lateral diffusion speed might suggest either that the clustered, slow-moving ACKR3 receptors are detected as an immobile receptor population or, that due to the continuous basal recycling of the receptor, it shows less lateral mobility within the membrane, thus being classed as immobile receptors.

Upon CXCL12 addition, ACKR3 presented a significant reduction in diffusion coefficient while CXCR4 remained unchanged (Figure 6.1/FRAP). This result agrees with the ligand-induced observation on the nanoscale using FCS. Furthermore, both receptors presented a significant increase in immobile fraction following CXCL12 addition which might be due to the clustering and endocytosis of the activated receptors.

Lastly, the dynamics of ACKR3 were measured on a macro scale with RICS and were compared with previous unpublished results of CXCR4 measured by Dr Joelle Goulding. Similar to the FRAP data, there was no difference in the macro diffusion coefficient of ACKR3 and CXCR4 in basal conditions. Number and Brightness data of the RICS data revealed significantly higher apparent brightness of ACKR3 in basal condition compared to CXCR4. The data indicated the ACKR3 population to be mostly in a clustered state, while CXCR4 lies between monomer and dimer control. This aligns with our PCH result obtained from FCS data, suggesting a distinct basal oligomeric state of the two receptors.

Following CXCL12 stimulation, neither of the receptors showed a ligand-induced effect on their dynamics or oligomerisation in the macroscale, although the number of particles per pixel was reduced in the case of ACKR3 compared to vehicle conditions (Figure 6.1/RICS). This may suggest larger cluster size formation or internalisation. However, further validation with different techniques is necessary.

It is important to note that the data of ACKR3 in basal and CXCL12 captured in this study is quite variable and might suggest a bimodal distribution and the presence of subpopulations of receptor species; to support and validate this, the study requires further data collection. While no ACKR3 antagonist was available at the time of this study, a CXCR4 antagonist, IT1t, was used to assess antagonist-induced changes in the membrane dynamics of CXCR4. Our finding revealed no changes in the diffusion and oligomeric properties of CXCR4.

Overall, this study presented new data that demonstrate the distinct organisation and diffusion properties of ACKR3 and CXCR4 at the plasma membrane. This organisation could be relevant to the scavenging function of the ACKR3 receptor and the signalling abilities of CXCR4. However, further investigation involving other atypical chemokine receptors is required to determine whether this organisation is unique to ACKR3 or observed more broadly across ‘scavenger’ receptors.

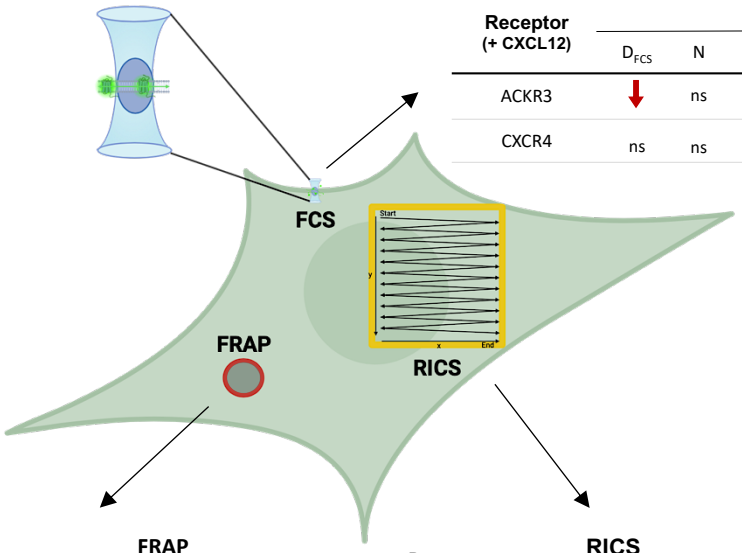

Receptor (+ CXCL12)	FCS		
	D_{FCS}	N	Second PCH component
ACKR3	↓	ns	ns
CXCR4	ns	ns	↑

Receptor (+ CXCL12)	FRAP	
	D_{FRAP}	Immobile fraction (%)
ACKR3	↓	↑
CXCR4	ns	↑

Receptor (+ CXCL12)	RICS		N&B	
	D_{RICS}	N (Amplitude)	Number	Brightness
ACKR3	ns	ns	↓	ns
CXCR4	ns	ns	ns	ns

Figure 6.1: Summary of our findings assessing the membrane dynamics of ACKR3 and CXCR4 on different scales. *Comparative illustration of the fluorescence spectroscopy techniques (FCS, FRAP and RICS) used to assess the membrane dynamics and organisation of ACKR3 and CXCR4. The tables summarise the effect of 10 nM CXCL12 compared to vehicle separately for ACKR3 and CXCR4.*

6.2. General Discussion: GRK Involvement in ACKR3 Trafficking

G protein-coupled receptor kinases (GRKs) are well known to have a role in the endocytosis of GPCRs via phosphorylating the activated receptor which then can bind to β-arrestin to induce receptor desensitisation and internalisation [171, 172]. Moreover, previous studies have shown the diverse roles of the different GRK isoforms in the signal regulation of GPCRs and in their intracellular trafficking [173, 193, 209]. Unexpectedly, our data showed no change in the constitutive internalisation of ACKR3 upon GRK depletion. However, confocal images indicated a different subcellular location in the absence of GRK2/3/5 and 6. This finding is in part, consistent with other recently published studies [186, 187], indicating that ACKR3 constitutive internalisation is GRK-independent. Previous research on CXCR4 constitutive internalisation showed similar arrestin-independent endocytosis which was only dependent on PKC and dynamin [181, 182]. Based on these data, while ACKR3 constitutively internalises to a different degree than CXCR4, the underlying mechanism might be similar to CXCR4.

Co-localisation with the subcellular compartments, early endosomes and lysosomes, was performed to check the intracellular location of the ACKR3 receptor and assess the change upon GRK deletion. The data showed unchanged ACKR3 co-localisation with early endosomes and a significant increase in receptor co-localisation with lysosomes in the absence of GRKs. This finding indicated an opposite trafficking effect compared to CXCR4, where previous studies showed that GRK6 is essential to the lysosomal degradation of CXCR4 [74]. Changes in GRK expression have been suggested to have a role in tumour development and maybe a regulatory role in GPCRs, including CXCR4 [200, 201]. As the results suggest GRK role in ACKR3 trafficking, it might be beneficial to further elucidate a GRK role in cancer and a potential role in CXCR4/ACKR3/CXCL12 axis.

ACKR3 is believed to act as a ‘scavenger’ receptor. Following ligand activation, ACKR3 internalises, resulting in a change in chemokine availability, and then recycles back to the plasma surface for further chemokine binding

[64, 147]. Previous studies suggested that receptor phosphorylation via GRKs might be essential for the scavenging function [73, 186]. It is important to highlight that all previous studies focused on assessing the role of GRKs and phosphorylation in CXCL12-activated ACKR3 while, we assessed the effect of GRK depletion in constitutive internalisation and trafficking of ACKR3. However, the altered basal ACKR3 trafficking in the absence of GRKs suggest that GRKs have a role in the receptor trafficking and might be crucial for receptor 'scavenging' nature independently of ligand activation.

Overall, the functional role of continuous basal recycling of ACKR3 remains unknown. However, our study revealed a potential role of GRKs in ACKR3 basal trafficking towards recycling. This finding requires further experimental validation to understand the underlying mechanism and function.

6.3. Outlook and Future Directions

In this study, we presented fluorescence spectroscopy and confocal imaging data elucidating the organisation and dynamics of ACKR3 and CXCR4 at the plasma membrane. Our findings reveal distinct basal oligomeric states of the two receptors and different effects upon CXCL12 stimulation. While these results offer valuable insights into the organisation of these two receptors, it is important to acknowledge that our study was conducted using stable HEK cell lines, overexpressing either SNAP-CXCR4 or SNAP-ACKR3. Previous studies have suggested that CXCR4 and ACKR3 have the potential to form heteromers with each other, influencing the signalling of one another [210, 211]. As a future direction, assessing the heteromer formation and its effect on the organisation and dynamics of CXCR4 and ACKR3 would provide further insight into understanding the dynamics of the CXCR4/ACKR3/CXCL12 axis. One of the possible approaches would involve the generation of HEK cell lines co-expressing ACKR3 and CXCR4, each tagged with two different fluorescence tags, such as SNAP and Halo-tag. This would enable the application of dual-colour fluorescence cross-correlation correlation spectroscopy (FCCS) combined with the Förster Resonance Energy transfer (FRET) technique, providing information about membrane dynamics and interactions between the two receptors. The protocol to use these two techniques was created and successfully used previously with another GPCR β_2-adrenergic receptor (β_2AR) [212]. Moreover, ACKR3 and CXCR4 are suggested to have a role in various cancers [63, 213] hence, investigating the dynamics of the two receptors in cancer cells at an endogenous expression level would be advantageous. White et al. previously created a NanoLuc-CXCR4 CRISPR/Cas9 genome-engineered cell line to study ligand binding and receptor conformational change at the endogenous expression level [135, 214]. Using this approach to create a SNAP-tagged CRISPR/Cas9 cell line would enable the evaluation of receptor dynamics at low expression levels. In addition, a previous study involving β2-adrenoceptors, another GPCR, showed it is possible to measure dynamics at low expression levels close to the endogenous receptor expression using FCS [79].

Our findings in this study provided evidence of increased co-localisation of basal ACKR3 receptors with lysosomes upon the depletion of GRKs. This data suggests that while the constitutive internalisation of ACKR3 occurs independently of GRKs, the trafficking of ACKR3 is directed more towards the lysosomal pathway in their absence. This study utilised quadruple GRK knock-out, GRK2/3 KO and GRK5/6 KO cell lines. It would be beneficial to use triple GRK knock-out cell lines, only expressing a single GRK isoform to elucidate the specific role of each isoform. Additionally, conducting further co-localisation studies with other subcellular markers, such as recycling endosome marker Rab 11 [195] would provide more details about the GRK role in ACKR3 trafficking. In Chapter 5, preliminary data showed the localisation of ACKR3 upon CXCL12 stimulation (Figure 5.12), indicating different receptor locations compared to basal conditions in GRK-depleted cell lines. While this preliminary data is interesting, it requires further experimentation to assess the distinct endocytosis and trafficking of the CXCL12-activated ACKR3 using co-localisation imaging studies.

Lastly, this thesis showed that the absence of GRK had no effect on the constitutive internalisation of the ACKR3 receptor. Our preliminary data shown in Chapter 5 (Figure 5.11) that inhibition of dynamin results in decreased internalisation, although additional validation is required. This suggests that basal ACKR3 internalisation might be clathrin-dependent. Further experiments are necessary with clathrin and dynamin inhibitors such as Pitstop2 [190] to provide more information about the mechanism of ACKR3 constitutive internalisation. Future research assessing the role and expression of GRKs in ACKR3 trafficking in cancer cells would be important, considering that a previous study suggested the role of GRK3 in the regulation of CXCR4 in cancer [200].

6.4. Key Conclusions

In summary, this thesis presented novel data using confocal microscopy and advanced spectroscopy methods to provide information about the different organisation and dynamics of CXCR4 and ACKR3 at the plasma membrane on various scales. Our data indicate that while CXCR4 is majorly located on the membrane and presents a lower oligomeric state, ACKR3 is predominantly located intracellularly, with nearly half of the receptor population existing in a clustered state. In the case of CXCR4, no ligand-induced changes in the lateral diffusion were observed; however, the oligomeric state was altered upon CXCL12 stimulation. Conversely, ACKR3 showed reduced diffusion speed following CXCL12 stimulation, while its oligomeric state remained unchanged. Additionally, our data suggested an increase in lysosomal localisation of ACKR3 in the absence of GRKs, suggesting an important role of GRKs in post-internalisation trafficking of this receptor.

This work was part of the ONCORNET 2.0 consortium, which aimed to understand the two oncogenic receptors, CXCR4 and ACKR3, through multiple projects assessing the two receptors from different aspects. The data from this thesis provided new information about the dynamics and trafficking of ACKR3 and contributed to the progress in understanding the CXCR4/ACKR3 axis. Combining the new knowledge throughout this international training network aimed to improve our understanding of the CXCR4 and ACKR3 mechanism and their role in tumours, and to potentially contribute to new drug development.

Chapter 7: References

1. Fredriksson, R., et al., *The G-protein-coupled receptors in the human genome form five main families. Phylogenetic analysis, paralogon groups, and fingerprints.* Mol Pharmacol, 2003. **63**(6): p. 1256-72.
2. Hauser, A.S., et al., *GPCR activation mechanisms across classes and macro/microscales.* Nature Structural & Molecular Biology, 2021. **28**(11): p. 879-888.
3. Palczewski, K., et al., *Crystal Structure of Rhodopsin: A G Protein-Coupled Receptor.* Science, 2000. **289**(5480): p. 739-745.
4. Rasmussen, S.G., et al., *Crystal structure of the human beta2 adrenergic G-protein-coupled receptor.* Nature, 2007. **450**(7168): p. 383-7.
5. García-Nafría, J. and C.G. Tate, *Structure determination of GPCRs: cryo-EM compared with X-ray crystallography.* Biochemical Society Transactions, 2021. **49**(5): p. 2345-2355.
6. Cheng, L., et al., *Structure, function and drug discovery of GPCR signaling.* Molecular Biomedicine, 2023. **4**(1): p. 46.
7. Lu, Z.L., J.W. Saldanha, and E.C. Hulme, *Seven-transmembrane receptors: crystals clarify.* Trends Pharmacol Sci, 2002. **23**(3): p. 140-6.
8. Rosenbaum, D.M., S.G. Rasmussen, and B.K. Kobilka, *The structure and function of G-protein-coupled receptors.* Nature, 2009. **459**(7245): p. 356-63.
9. Zhang, D., Q. Zhao, and B. Wu, *Structural Studies of G Protein-Coupled Receptors.* Mol Cells, 2015. **38**(10): p. 836-42.
10. Venkatakrishnan, A.J., et al., *Molecular signatures of G-protein-coupled receptors.* Nature, 2013. **494**(7436): p. 185-194.
11. Katritch, V., V. Cherezov, and R.C. Stevens, *Diversity and modularity of G protein-coupled receptor structures.* Trends Pharmacol Sci, 2012. **33**(1): p. 17-27.
12. Yang, D., et al., *G protein-coupled receptors: structure- and function-based drug discovery.* Signal Transduction and Targeted Therapy, 2021. **6**(1): p. 7.
13. Weis, W.I. and B.K. Kobilka, *The Molecular Basis of G Protein-Coupled Receptor Activation.* Annu Rev Biochem, 2018. **87**: p. 897-919.
14. Gurevich, V.V. and E.V. Gurevich, *GPCR Signaling Regulation: The Role of GRKs and Arrestins.* Front Pharmacol, 2019. **10**: p. 125.
15. Frank, M., et al., *G Protein activation without subunit dissociation depends on a G{alpha}(i)-specific region.* J Biol Chem, 2005. **280**(26): p. 24584-90.
16. Syrovatkina, V., et al., *Regulation, Signaling, and Physiological Functions of G-Proteins.* Journal of Molecular Biology, 2016. **428**(19): p. 3850-3868.
17. Oldham, W.M. and H.E. Hamm, *Heterotrimeric G protein activation by G-protein-coupled receptors.* Nat Rev Mol Cell Biol, 2008. **9**(1): p. 60-71.

18. Offermanns, S., *G-proteins as transducers in transmembrane signalling.* Progress in Biophysics and Molecular Biology, 2003. **83**(2): p. 101-130.
19. Dupré, D.J., et al., *The role of Gbetagamma subunits in the organization, assembly, and function of GPCR signaling complexes.* Annu Rev Pharmacol Toxicol, 2009. **49**: p. 31-56.
20. Ritter, S.L. and R.A. Hall, *Fine-tuning of GPCR activity by receptor-interacting proteins.* Nat Rev Mol Cell Biol, 2009. **10**(12): p. 819-30.
21. Gurevich, E.V., et al., *G protein-coupled receptor kinases: more than just kinases and not only for GPCRs.* Pharmacol Ther, 2012. **133**(1): p. 40-69.
22. Premont, R.T., et al., *Characterization of the G protein-coupled receptor kinase GRK4. Identification of four splice variants.* J Biol Chem, 1996. **271**(11): p. 6403-10.
23. Pitcher, J.A., N.J. Freedman, and R.J. Lefkowitz, *G protein-coupled receptor kinases.* Annu Rev Biochem, 1998. **67**: p. 653-92.
24. Chen, Q., et al., *Structures of rhodopsin in complex with G-protein-coupled receptor kinase 1.* Nature, 2021. **595**(7868): p. 600-605.
25. Zhao, X., et al., *A novel form of rhodopsin kinase from chicken retina and pineal gland.* FEBS Lett, 1999. **454**(1-2): p. 115-21.
26. Pugh, E.N. and T.D. Lamb, *Chapter 5 Phototransduction in vertebrate rods and cones: Molecular mechanisms of amplification, recovery and light adaptation*, in *Handbook of Biological Physics*, D.G. Stavenga, W.J. DeGrip, and E.N. Pugh, Editors. 2000, North-Holland. p. 183-255.
27. Miess, E., et al., *Multisite phosphorylation is required for sustained interaction with GRKs and arrestins during rapid μ-opioid receptor desensitization.* Sci Signal, 2018. **11**(539).
28. Smith, J.S. and S. Rajagopal, *The β-Arrestins: Multifunctional Regulators of G Protein-coupled Receptors.* J Biol Chem, 2016. **291**(17): p. 8969-77.
29. Lohse, M.J. and C. Hoffmann, *Arrestin interactions with G protein-coupled receptors.* Handb Exp Pharmacol, 2014. **219**: p. 15-56.
30. Seyedabadi, M., et al., *Receptor-Arrestin Interactions: The GPCR Perspective.* Biomolecules, 2021. **11**(2).
31. Underwood, O., et al., *Arrestin-centred interactions at the membrane and their conformational determinants.* Br J Pharmacol, 2024.
32. Wess, J., et al., *β-Arrestins: Structure, Function, Physiology, and Pharmacological Perspectives.* Pharmacol Rev, 2023. **75**(5): p. 854-884.
33. Pavlos, N.J. and P.A. Friedman, *GPCR Signaling and Trafficking: The Long and Short of It.* Trends Endocrinol Metab, 2017. **28**(3): p. 213-226.
34. Grundmann, M., et al., *Lack of beta-arrestin signaling in the absence of active G proteins.* Nat Commun, 2018. **9**(1): p. 341.
35. Luttrell, L.M., et al., *Manifold roles of β-arrestins in GPCR signaling elucidated with siRNA and CRISPR/Cas9.* Sci Signal, 2018. **11**(549).
36. Eichel, K. and M. von Zastrow, *Subcellular Organization of GPCR Signaling.* Trends Pharmacol Sci, 2018. **39**(2): p. 200-208.

37. Bahouth, S.W. and M.M. Nooh, *Barcoding of GPCR trafficking and signaling through the various trafficking roadmaps by compartmentalized signaling networks.* Cellular signalling, 2017. **36**: p. 42-55.
38. Oakley, R.H., et al., *Differential affinities of visual arrestin, beta arrestin1, and beta arrestin2 for G protein-coupled receptors delineate two major classes of receptors.* J Biol Chem, 2000. **275**(22): p. 17201-10.
39. Burton, J.C. and N.J. Grimsey, *Ubiquitination as a Key Regulator of Endosomal Signaling by GPCRs.* Frontiers in Cell and Developmental Biology, 2019. **7**.
40. Skieterska, K., P. Rondou, and K. Van Craenenbroeck, *Regulation of G Protein-Coupled Receptors by Ubiquitination.* Int J Mol Sci, 2017. **18**(5).
41. Shenoy, S.K. and R.J. Lefkowitz, *Receptor-specific Ubiquitination of β-Arrestin Directs Assembly and Targeting of Seven-transmembrane Receptor Signalosomes*.* Journal of Biological Chemistry, 2005. **280**(15): p. 15315-15324.
42. Calebiro, D., *EJE AWARD 2020: Signalling by G protein-coupled receptors: why space and time matter.* European Journal of Endocrinology, 2021. **184**(2): p. R41-R49.
43. Godbole, A., et al., *Internalized TSH receptors en route to the TGN induce local Gs-protein signaling and gene transcription.* Nature Communications, 2017. **8**(1): p. 443.
44. Kliewer, A., R.K. Reinscheid, and S. Schulz, *Emerging Paradigms of G Protein-Coupled Receptor Dephosphorylation.* Trends in Pharmacological Sciences, 2017. **38**(7): p. 621-636.
45. Moser, B., et al., *Chemokines: multiple levels of leukocyte migration control.* Trends Immunol, 2004. **25**(2): p. 75-84.
46. Proudfoot, A.E., *Chemokine receptors: multifaceted therapeutic targets.* Nat Rev Immunol, 2002. **2**(2): p. 106-15.
47. Sanchez, J., et al., *Influence of Chemokine N-Terminal Modification on Biased Agonism at the Chemokine Receptor CCR1.* Int J Mol Sci, 2019. **20**(10).
48. Bachelerie, F., et al., *International Union of Basic and Clinical Pharmacology. [corrected]. LXXXIX. Update on the extended family of chemokine receptors and introducing a new nomenclature for atypical chemokine receptors.* Pharmacol Rev, 2014. **66**(1): p. 1-79.
49. Arimont, M., et al., *Chemokine Receptor Crystal Structures: What Can Be Learned from Them?* Mol Pharmacol, 2019. **96**(6): p. 765-777.
50. Proudfoot, A.E., et al., *Glycosaminoglycan binding and oligomerization are essential for the in vivo activity of certain chemokines.* Proc Natl Acad Sci U S A, 2003. **100**(4): p. 1885-90.
51. Bachelerie, F., et al., *An atypical addition to the chemokine receptor nomenclature: IUPHAR Review 15.* British Journal of Pharmacology, 2015. **172**(16): p. 3945-3949.
52. Zheng, Y., et al., *Structure of CC Chemokine Receptor 5 with a Potent Chemokine Antagonist Reveals Mechanisms of Chemokine Recognition and Molecular Mimicry by HIV.* Immunity, 2017. **46**(6): p. 1005-1017.e5.

53. Sanchez, J., et al., *Evaluation and extension of the two-site, two-step model for binding and activation of the chemokine receptor CCR1.* J Biol Chem, 2019. **294**(10): p. 3464-3475.
54. Zheng, Y., et al., *Structure of CC chemokine receptor 2 with orthosteric and allosteric antagonists.* Nature, 2016. **540**(7633): p. 458-461.
55. Lazennec, G. and A. Richmond, *Chemokines and chemokine receptors: new insights into cancer-related inflammation.* Trends in Molecular Medicine, 2010. **16**(3): p. 133-144.
56. Esche, C., C. Stellato, and L.A. Beck, *Chemokines: Key Players in Innate and Adaptive Immunity.* Journal of Investigative Dermatology, 2005. **125**(4): p. 615-628.
57. Scholten, D.J., et al., *Pharmacological modulation of chemokine receptor function.* Br J Pharmacol, 2012. **165**(6): p. 1617-1643.
58. Mollica Poeta, V., et al., *Chemokines and Chemokine Receptors: New Targets for Cancer Immunotherapy.* Frontiers in Immunology, 2019. **10**(379).
59. Janssens, R., S. Struyf, and P. Proost, *The unique structural and functional features of CXCL12.* Cellular & Molecular Immunology, 2018. **15**(4): p. 299-311.
60. Döring, Y., et al., *The CXCL12/CXCR4 chemokine ligand/receptor axis in cardiovascular disease.* Frontiers in Physiology, 2014. **5**(212).
61. Wu, B., et al., *Structures of the CXCR4 chemokine GPCR with small-molecule and cyclic peptide antagonists.* Science, 2010. **330**(6007): p. 1066-71.
62. Qin, L., et al., *Crystal structure of the chemokine receptor CXCR4 in complex with a viral chemokine.* Science, 2015. **347**(6226): p. 1117-1122.
63. Santagata, S., et al., *CXCR4 and CXCR7 Signaling Pathways: A Focus on the Cross-Talk Between Cancer Cells and Tumor Microenvironment.* Front Oncol, 2021. **11**: p. 591386.
64. Smit, M.J., et al., *The CXCL12/CXCR4/ACKR3 Axis in the Tumor Microenvironment: Signaling, Crosstalk, and Therapeutic Targeting.* Annual Review of Pharmacology and Toxicology, 2021. **61**(1): p. 541-563.
65. Ulvmar, M.H., E. Hub, and A. Rot, *Atypical chemokine receptors.* Exp Cell Res, 2011. **317**(5): p. 556-68.
66. Otun, O., et al., *Conformational dynamics underlying Atypical Chemokine Receptor 3 activation.* bioRxiv, 2023: p. 2023.07.17.549382.
67. Yen, Y.C., et al., *Structures of atypical chemokine receptor 3 reveal the basis for its promiscuity and signaling bias.* Sci Adv, 2022. **8**(28): p. eabn8063.
68. Yen, Y.-C., et al., *Cryo-EM Structure of Atypical Chemokine Receptor 3 (ACKR3) in Complex with its Endogenous Ligand CXCL12.* The FASEB Journal, 2021. **35**(S1).
69. Bonecchi, R. and G.J. Graham, *Atypical Chemokine Receptors and Their Roles in the Resolution of the Inflammatory Response.* Front Immunol, 2016. **7**: p. 224.

70. Meyrath, M., et al., *The atypical chemokine receptor ACKR3/CXCR7 is a broad-spectrum scavenger for opioid peptides.* Nature Communications, 2020. **11**(1): p. 3033.
71. Fumagalli, A., et al., *CXCR4/ACKR3 Phosphorylation and Recruitment of Interacting Proteins: Key Mechanisms Regulating Their Functional Status.* Molecular Pharmacology, 2019. **96**(6): p. 794-808.
72. Canals, M., et al., *Ubiquitination of CXCR7 controls receptor trafficking.* PLoS One, 2012. **7**(3): p. e34192.
73. Zarca, A., et al., *Differential Involvement of ACKR3 C-Tail in β-Arrestin Recruitment, Trafficking and Internalization.* Cells, 2021. **10**(3): p. 618.
74. Caballero, A., et al., *Heterologous regulation of CXCR4 lysosomal trafficking.* J Biol Chem, 2019. **294**(20): p. 8023-8036.
75. Elliott, A.D., *Confocal Microscopy: Principles and Modern Practices.* Current protocols in cytometry, 2020. **92**(1): p. e68-e68.
76. Kilpatrick, L.E. and S.J. Hill, *The use of fluorescence correlation spectroscopy to characterize the molecular mobility of fluorescently labelled G protein-coupled receptors.* Biochem Soc Trans, 2016. **44**(2): p. 624-9.
77. Briddon, S.J., L.E. Kilpatrick, and S.J. Hill, *Studying GPCR Pharmacology in Membrane Microdomains: Fluorescence Correlation Spectroscopy Comes of Age.* Trends Pharmacol Sci, 2018. **39**(2): p. 158-174.
78. Briddon, S.J. and S.J. Hill, *Pharmacology under the microscope: the use of fluorescence correlation spectroscopy to determine the properties of ligand-receptor complexes.* Trends Pharmacol Sci, 2007. **28**(12): p. 637-45.
79. Goulding, J., et al., *The use of fluorescence correlation spectroscopy to monitor cell surface β2-adrenoceptors at low expression levels in human embryonic stem cell-derived cardiomyocytes and fibroblasts.* The FASEB Journal, 2021. **35**(4): p. e21398.
80. Briddon, S.J., et al., *Quantitative analysis of the formation and diffusion of A1-adenosine receptor-antagonist complexes in single living cells.* Proc Natl Acad Sci U S A, 2004. **101**(13): p. 4673-8.
81. Kilpatrick, L.E., S.J. Briddon, and N.D. Holliday, *Fluorescence correlation spectroscopy, combined with bimolecular fluorescence complementation, reveals the effects of β-arrestin complexes and endocytic targeting on the membrane mobility of neuropeptide Y receptors.* Biochim Biophys Acta, 2012. **1823**(6): p. 1068-81.
82. Ishikawa-Ankerhold, H.C., R. Ankerhold, and G.P.C. Drummen, *Advanced fluorescence microscopy techniques--FRAP, FLIP, FLAP, FRET and FLIM.* Molecules (Basel, Switzerland), 2012. **17**(4): p. 4047-4132.
83. Lippincott-Schwartz, J., E.L. Snapp, and R.D. Phair, *The Development and Enhancement of FRAP as a Key Tool for Investigating Protein Dynamics.* Biophys J, 2018. **115**(7): p. 1146-1155.
84. Gondin, A.B., et al., *GRK Mediates μ-Opioid Receptor Plasma Membrane Reorganization.* Front Mol Neurosci, 2019. **12**: p. 104.
85. Rossow, M.J., et al., *Raster image correlation spectroscopy in live cells.* Nature Protocols, 2010. **5**(11): p. 1761-1774.

86. Digman, M.A. and E. Gratton, *Scanning image correlation spectroscopy.* Bioessays, 2012. **34**(5): p. 377-85.
87. Digman, M.A., M. Stakic, and E. Gratton, *Raster image correlation spectroscopy and number and brightness analysis.* Methods Enzymol, 2013. **518**: p. 121-44.
88. Bacart, J., et al., *The BRET technology and its application to screening assays.* Biotechnol J, 2008. **3**(3): p. 311-24.
89. Borroto-Escuela, D.O., et al., *Bioluminescence resonance energy transfer methods to study G protein-coupled receptor-receptor tyrosine kinase heteroreceptor complexes.* Methods Cell Biol, 2013. **117**: p. 141-64.
90. Stoddart, L.A., et al., *Application of BRET to monitor ligand binding to GPCRs.* Nat Methods, 2015. **12**(7): p. 661-663.
91. Harikumar, K.G., et al., *Bioluminescence Resonance Energy Transfer (BRET) Assay for Determination of Molecular Interactions in Living Cells.* Bio Protoc, 2017. **7**(22).
92. Donthamsetti, P., et al., *Using Bioluminescence Resonance Energy Transfer (BRET) to Characterize Agonist-Induced Arrestin Recruitment to Modified and Unmodified G Protein-Coupled Receptors.* Curr Protoc Pharmacol, 2015. **70**: p. 2.14.1-2.14.14.
93. Avet, C., et al., *Effector membrane translocation biosensors reveal G protein and βarrestin coupling profiles of 100 therapeutically relevant GPCRs.* Elife, 2022. **11**.
94. Dekkers, S., et al., *Small-Molecule Fluorescent Ligands for the CXCR4 Chemokine Receptor.* Journal of Medicinal Chemistry, 2023. **66**(7): p. 5208-5222.
95. Drube, J., et al., *GPCR kinase knockout cells reveal the impact of individual GRKs on arrestin binding and GPCR regulation.* Nat Commun, 2022. **13**(1): p. 540.
96. Mo, X.L. and H. Fu, *BRET: NanoLuc-Based Bioluminescence Resonance Energy Transfer Platform to Monitor Protein-Protein Interactions in Live Cells.* Methods Mol Biol, 2016. **1439**: p. 263-71.
97. Cole, N.B., *Site-specific protein labeling with SNAP-tags.* Curr Protoc Protein Sci, 2013. **73**: p. 30.1.1-30.1.16.
98. PicoQuant. *https://www.picoquant.com/images/uploads/page/files/7353/appnote_diffusioncoefficients.pdf*. 2010.
99. BROWN, C.M., et al., *Raster image correlation spectroscopy (RICS) for measuring fast protein dynamics and concentrations with a commercial laser scanning confocal microscope.* Journal of Microscopy, 2008. **229**(1): p. 78-91.
100. Fukushima, R., J. Yamamoto, and M. Kinjo, *Number and Brightness Analysis: Visualization of Protein Oligomeric State in Living Cells.* Advances in experimental medicine and biology, 2021. **1310**: p. 31-58.
101. Rizk, A., et al., *Segmentation and quantification of subcellular structures in fluorescence microscopy images using Squassh.* Nat Protoc, 2014. **9**(3): p. 586-96.
102. Schneider, C.A., W.S. Rasband, and K.W. Eliceiri, *NIH Image to ImageJ: 25 years of image analysis.* Nature Methods, 2012. **9**(7): p. 671-675.

103. Team, R.C. *R: A language and environment for statistical computing. R Foundation for Statistical Computing*. 2021; Available from: www.R-project.org.
104. Schindelin, J., et al., *Fiji: an open-source platform for biological-image analysis.* Nature Methods, 2012. **9**(7): p. 676-682.
105. Pierce, K.L., R.T. Premont, and R.J. Lefkowitz, *Seven-transmembrane receptors.* Nat Rev Mol Cell Biol, 2002. **3**(9): p. 639-50.
106. Hilger, D., M. Masureel, and B.K. Kobilka, *Structure and dynamics of GPCR signaling complexes.* Nat Struct Mol Biol, 2018. **25**(1): p. 4-12.
107. Hilger, D., *The role of structural dynamics in GPCR-mediated signaling.* The FEBS Journal, 2021. **288**(8): p. 2461-2489.
108. Kayser, C., et al., *Spatiotemporal GPCR signaling illuminated by genetically encoded fluorescent biosensors.* Current Opinion in Pharmacology, 2023. **71**: p. 102384.
109. Halls, M.L. and M. Canals, *Genetically Encoded FRET Biosensors to Illuminate Compartmentalised GPCR Signalling.* Trends in Pharmacological Sciences, 2018. **39**(2): p. 148-157.
110. Mondal, S., et al., *Membrane Driven Spatial Organization of GPCRs.* Scientific Reports, 2013. **3**(1): p. 2909.
111. Ferré, S., et al., *G protein-coupled receptor oligomerization revisited: functional and pharmacological perspectives.* Pharmacol Rev, 2014. **66**(2): p. 413-34.
112. Pétrin, D. and T.E. Hébert, *The functional size of GPCRs - monomers, dimers or tetramers?* Subcell Biochem, 2012. **63**: p. 67-81.
113. Canals, M., et al., *Homodimerization of adenosine A2A receptors: qualitative and quantitative assessment by fluorescence and bioluminescence energy transfer.* J Neurochem, 2004. **88**(3): p. 726-34.
114. May, L.T., et al., *Allosteric interactions across native adenosine-A3 receptor homodimers: quantification using single-cell ligand-binding kinetics.* Faseb j, 2011. **25**(10): p. 3465-76.
115. Weinberg, Z.Y. and M.A. Puthenveedu, *Regulation of G protein-coupled receptor signaling by plasma membrane organization and endocytosis.* Traffic, 2019. **20**(2): p. 121-129.
116. Calebiro, D. and T. Sungkaworn, *Single-Molecule Imaging of GPCR Interactions.* Trends Pharmacol Sci, 2018. **39**(2): p. 109-122.
117. Hill, S.J. and S.P. Watson, *Fluorescence Approaches Unravel Spatial and Temporal Aspects of GPCR Organisation, Location, and Intracellular Signalling.* Trends Pharmacol Sci, 2018. **39**(2): p. 91-92.
118. Fessl, T., M. Majellaro, and A. Bondar, *Microscopy and spectroscopy approaches to study GPCR structure and function.* British Journal of Pharmacology. **n/a**(n/a).
119. Cordeaux, Y., et al., *Agonist-occupied A3 adenosine receptors exist within heterogeneous complexes in membrane microdomains of individual living cells.* Faseb j, 2008. **22**(3): p. 850-60.
120. Wohland, T., et al., *Study of Ligand−Receptor Interactions by Fluorescence Correlation Spectroscopy with Different Fluorophores: Evidence That the Homopentameric 5-Hydroxytryptamine Type 3As Receptor Binds Only One Ligand.* Biochemistry, 1999. **38**(27): p. 8671-8681.

121. Hegener, O., et al., *Dynamics of beta2-adrenergic receptor-ligand complexes on living cells.* Biochemistry, 2004. **43**(20): p. 6190-9.
122. Rose, R.H., S.J. Briddon, and S.J. Hill, *A novel fluorescent histamine H(1) receptor antagonist demonstrates the advantage of using fluorescence correlation spectroscopy to study the binding of lipophilic ligands.* Br J Pharmacol, 2012. **165**(6): p. 1789-1800.
123. Herrick-Davis, K., et al., *Fluorescence correlation spectroscopy analysis of serotonin, adrenergic, muscarinic, and dopamine receptor dimerization: the oligomer number puzzle.* Mol Pharmacol, 2013. **84**(4): p. 630-42.
124. Zhang, L., et al., *Using FCS to accurately measure protein concentration in the presence of noise and photobleaching.* Biophys J, 2021. **120**(19): p. 4230-4241.
125. Diekmann, S. and C. Hoischen, *Biomolecular dynamics and binding studies in the living cell.* Physics of Life Reviews, 2014. **11**(1): p. 1-30.
126. Vámosi, G., et al., *EGF Receptor Stalls upon Activation as Evidenced by Complementary Fluorescence Correlation Spectroscopy and Fluorescence Recovery after Photobleaching Measurements.* Int J Mol Sci, 2019. **20**(13).
127. Caspar, B., et al., *CXCR4 as a novel target in immunology: moving away from typical antagonists.* Future Drug Discov, 2022. **4**(2): p. Fdd77.
128. Freitas, C., et al., *The relevance of the chemokine receptor ACKR3/CXCR7 on CXCL12-mediated effects in cancers with a focus on virus-related cancers.* Cytokine Growth Factor Rev, 2014. **25**(3): p. 307-16.
129. Busillo, J.M., et al., *Site-specific phosphorylation of CXCR4 is dynamically regulated by multiple kinases and results in differential modulation of CXCR4 signaling.* J Biol Chem, 2010. **285**(10): p. 7805-17.
130. Marchese, A., *Endocytic trafficking of chemokine receptors.* Current Opinion in Cell Biology, 2014. **27**: p. 72-77.
131. Venkatesan, S., et al., *Distinct mechanisms of agonist-induced endocytosis for human chemokine receptors CCR5 and CXCR4.* Mol Biol Cell, 2003. **14**(8): p. 3305-24.
132. Martínez-Muñoz, L., et al., *Separating Actin-Dependent Chemokine Receptor Nanoclustering from Dimerization Indicates a Role for Clustering in CXCR4 Signaling and Function.* Molecular Cell, 2018. **70**(1): p. 106-119.e10.
133. Işbilir, A., et al., *Advanced fluorescence microscopy reveals disruption of dynamic CXCR4 dimerization by subpocket-specific inverse agonists.* Proceedings of the National Academy of Sciences, 2020. **117**(46): p. 29144-29154.
134. Huang, B., T.D. Perroud, and R.N. Zare, *Photon counting histogram: one-photon excitation.* Chemphyschem, 2004. **5**(10): p. 1523-31.
135. White, C.W., et al., *CRISPR-Mediated Protein Tagging with Nanoluciferase to Investigate Native Chemokine Receptor Function and Conformational Changes.* Cell Chem Biol, 2020. **27**(5): p. 499-510.e7.

136. Corriden, R., et al., *Kinetic analysis of antagonist-occupied adenosine-A3 receptors within membrane microdomains of individual cells provides evidence of receptor dimerization and allosterism.* Faseb j, 2014. **28**(10): p. 4211-22.
137. Weiss, M., H. Hashimoto, and T. Nilsson, *Anomalous protein diffusion in living cells as seen by fluorescence correlation spectroscopy.* Biophys J, 2003. **84**(6): p. 4043-52.
138. Herrick-Davis, K., et al., *Oligomer size of the serotonin 5-hydroxytryptamine 2C (5-HT2C) receptor revealed by fluorescence correlation spectroscopy with photon counting histogram analysis: evidence for homodimers without monomers or tetramers.* J Biol Chem, 2012. **287**(28): p. 23604-14.
139. Kenworthy, A.K., et al., *Dynamics of putative raft-associated proteins at the cell surface.* J Cell Biol, 2004. **165**(5): p. 735-46.
140. Beletkaia, E., et al., *CXCR4 signaling is controlled by immobilization at the plasma membrane.* Biochimica et Biophysica Acta (BBA) - Molecular Cell Research, 2016. **1863**(4): p. 607-616.
141. Wysoczynski, M., et al., *Incorporation of CXCR4 into membrane lipid rafts primes homing-related responses of hematopoietic stem/progenitor cells to an SDF-1 gradient.* Blood, 2005. **105**(1): p. 40-8.
142. Bruckbauer, A., et al., *Selective diffusion barriers separate membrane compartments.* Biophys J, 2010. **99**(1): p. L1-3.
143. Balabanian, K., et al., *The chemokine SDF-1/CXCL12 binds to and signals through the orphan receptor RDC1 in T lymphocytes.* J Biol Chem, 2005. **280**(42): p. 35760-6.
144. Murphy, P.M. and L. Heusinkveld, *Multisystem multitasking by CXCL12 and its receptors CXCR4 and ACKR3.* Cytokine, 2018. **109**: p. 2-10.
145. Nagarsheth, N., M.S. Wicha, and W. Zou, *Chemokines in the cancer microenvironment and their relevance in cancer immunotherapy.* Nat Rev Immunol, 2017. **17**(9): p. 559-572.
146. Neves, M., et al., *Crosstalk between CXCR4/ACKR3 and EGFR Signaling in Breast Cancer Cells.* Int J Mol Sci, 2022. **23**(19).
147. Rajagopal, S., et al., *Beta-arrestin- but not G protein-mediated signaling by the "decoy" receptor CXCR7.* Proc Natl Acad Sci U S A, 2010. **107**(2): p. 628-32.
148. Abe, P., et al., *CXCR7 prevents excessive CXCL12-mediated downregulation of CXCR4 in migrating cortical interneurons.* Development, 2014. **141**(9): p. 1857-63.
149. Sánchez-Alcañiz, J.A., et al., *Cxcr7 controls neuronal migration by regulating chemokine responsiveness.* Neuron, 2011. **69**(1): p. 77-90.
150. Luker, K.E., et al., *Constitutive and chemokine-dependent internalization and recycling of CXCR7 in breast cancer cells to degrade chemokine ligands.* Oncogene, 2010. **29**(32): p. 4599-4610.
151. Digman, M.A. and E. Gratton, *Analysis of diffusion and binding in cells using the RICS approach.* Microsc Res Tech, 2009. **72**(4): p. 323-32.
152. Makaremi, S. and J. Moran-Mirabal, *Measuring the Lateral Diffusion of Plasma Membrane Receptors Using Raster Image Correlation Spectroscopy.* Methods Mol Biol, 2022. **2440**: p. 289-303.

153. Makaremi, S., et al., *Lateral diffusion of CD14 and TLR2 in macrophage plasma membrane assessed by raster image correlation spectroscopy and single particle tracking.* Sci Rep, 2020. **10**(1): p. 19375.
154. Brejchová, J., et al., *TRH-receptor mobility and function in intact and cholesterol-depleted plasma membrane of HEK293 cells stably expressing TRH-R-eGFP.* Biochimica et Biophysica Acta (BBA) - Biomembranes, 2015. **1848**(3): p. 781-796.
155. Cutrale, F., et al., *Using enhanced number and brightness to measure protein oligomerization dynamics in live cells.* Nature Protocols, 2019. **14**(2): p. 616-638.
156. Digman, M.A., et al., *Mapping the number of molecules and brightness in the laser scanning microscope.* Biophys J, 2008. **94**(6): p. 2320-32.
157. Işbilir, A., et al., *Determination of G-protein–coupled receptor oligomerization by molecular brightness analyses in single cells.* Nature Protocols, 2021. **16**(3): p. 1419-1451.
158. Zamai, M., et al., *Number and brightness analysis reveals that NCAM and FGF2 elicit different assembly and dynamics of FGFR1 in live cells.* J Cell Sci, 2019. **132**(1).
159. Dorsch, S., et al., *Analysis of receptor oligomerization by FRAP microscopy.* Nat Methods, 2009. **6**(3): p. 225-30.
160. Hoffmann, F., et al., *Rapid uptake and degradation of CXCL12 depend on CXCR7 carboxyl-terminal serine/threonine residues.* J Biol Chem, 2012. **287**(34): p. 28362-77.
161. Chen, Y., et al., *The photon counting histogram in fluorescence fluctuation spectroscopy.* Biophys J, 1999. **77**(1): p. 553-67.
162. Kask, P., et al., *Fluorescence-intensity distribution analysis and its application in biomolecular detection technology.* Proc Natl Acad Sci U S A, 1999. **96**(24): p. 13756-61.
163. Jacobson, K., P. Liu, and B.C. Lagerholm, *The Lateral Organization and Mobility of Plasma Membrane Components.* Cell, 2019. **177**(4): p. 806-819.
164. Mikuni, S., et al., *Negative Correlation between the Diffusion Coefficient and Transcriptional Activity of the Glucocorticoid Receptor.* Int J Mol Sci, 2017. **18**(9).
165. R, D.E.M., et al., *Dynamic range and background filtering in raster image correlation spectroscopy.* J Microsc, 2020. **279**(2): p. 123-138.
166. Wiseman, P.W., et al., *Two-photon image correlation spectroscopy and image cross-correlation spectroscopy.* J Microsc, 2000. **200**(Pt 1): p. 14-25.
167. Wolfe, B.L. and J. Trejo, *Clathrin-Dependent Mechanisms of G Protein-coupled Receptor Endocytosis.* Traffic, 2007. **8**(5): p. 462-470.
168. Kohout, T.A. and R.J. Lefkowitz, *Regulation of G protein-coupled receptor kinases and arrestins during receptor desensitization.* Mol Pharmacol, 2003. **63**(1): p. 9-18.
169. Schmid, E.M., et al., *Role of the AP2 beta-appendage hub in recruiting partners for clathrin-coated vesicle assembly.* PLoS Biol, 2006. **4**(9): p. e262.

170. Laporte, S.A., et al., *The interaction of beta-arrestin with the AP-2 adaptor is required for the clustering of beta 2-adrenergic receptor into clathrin-coated pits.* J Biol Chem, 2000. **275**(30): p. 23120-6.
171. Shenoy, S.K. and R.J. Lefkowitz, *Multifaceted roles of beta-arrestins in the regulation of seven-membrane-spanning receptor trafficking and signalling.* Biochem J, 2003. **375**(Pt 3): p. 503-15.
172. Jala, V.R., W.-H. Shao, and B. Haribabu, *Phosphorylation-independent β-Arrestin Translocation and Internalization of Leukotriene B₄ Receptors *.* Journal of Biological Chemistry, 2005. **280**(6): p. 4880-4887.
173. Kim, J., et al., *Functional antagonism of different G protein-coupled receptor kinases for beta-arrestin-mediated angiotensin II receptor signaling.* Proc Natl Acad Sci U S A, 2005. **102**(5): p. 1442-7.
174. Chen, Z., et al., *Agonist-induced internalization of leukotriene B(4) receptor 1 requires G-protein-coupled receptor kinase 2 but not arrestins.* Mol Pharmacol, 2004. **66**(3): p. 377-86.
175. Vines, C.M., et al., *N-formyl peptide receptors internalize but do not recycle in the absence of arrestins.* J Biol Chem, 2003. **278**(43): p. 41581-4.
176. Chen, B., et al., *Adaptor protein complex-2 (AP-2) and epsin-1 mediate protease-activated receptor-1 internalization via phosphorylation- and ubiquitination-dependent sorting signals.* J Biol Chem, 2011. **286**(47): p. 40760-70.
177. Diviani, D., et al., *The adaptor complex 2 directly interacts with the alpha 1b-adrenergic receptor and plays a role in receptor endocytosis.* J Biol Chem, 2003. **278**(21): p. 19331-40.
178. Dannhauser, P.N. and E.J. Ungewickell, *Reconstitution of clathrin-coated bud and vesicle formation with minimal components.* Nat Cell Biol, 2012. **14**(6): p. 634-9.
179. Hinrichsen, L., et al., *Bending a membrane: How clathrin affects budding.* Proceedings of the National Academy of Sciences, 2006. **103**(23): p. 8715-8720.
180. Scarselli, M. and J.G. Donaldson, *Constitutive internalization of G protein-coupled receptors and G proteins via clathrin-independent endocytosis.* J Biol Chem, 2009. **284**(6): p. 3577-85.
181. Signoret, N., et al., *Phorbol esters and SDF-1 induce rapid endocytosis and down modulation of the chemokine receptor CXCR4.* J Cell Biol, 1997. **139**(3): p. 651-64.
182. Signoret, N., et al., *Differential regulation of CXCR4 and CCR5 endocytosis.* J Cell Sci, 1998. **111 (Pt 18)**: p. 2819-30.
183. Claing, A., et al., *Endocytosis of G protein-coupled receptors: roles of G protein-coupled receptor kinases and ß-arrestin proteins.* Progress in Neurobiology, 2002. **66**(2): p. 61-79.
184. Marchese, A., et al., *The ins and outs of G protein-coupled receptor trafficking.* Trends Biochem Sci, 2003. **28**(7): p. 369-76.
185. Montpas, N., et al., *Ligand-specific conformational transitions and intracellular transport are required for atypical chemokine receptor 3-mediated chemokine scavenging.* J Biol Chem, 2018. **293**(3): p. 893-905.

186. Saaber, F., et al., *ACKR3 Regulation of Neuronal Migration Requires ACKR3 Phosphorylation, but Not β-Arrestin.* Cell Rep, 2019. **26**(6): p. 1473-1488.e9.
187. Schafer, C.T., et al., *Atypical Chemokine Receptor 3 "Senses" CXC Chemokine Receptor 4 Activation Through GPCR Kinase Phosphorylation.* Mol Pharmacol, 2023. **104**(4): p. 174-186.
188. Spiess, K., et al., *Arrestin-independent constitutive endocytosis of GPR125/ADGRA3.* Annals of the New York Academy of Sciences, 2019. **1456**(1): p. 186-199.
189. Paing, M.M., et al., *Clathrin Adaptor AP2 Regulates Thrombin Receptor Constitutive Internalization and Endothelial Cell Resensitization.* Molecular and Cellular Biology, 2006. **26**(8): p. 3231-3242.
190. Szewczyk-Roszczenko, O.K., et al., *The Chemical Inhibitors of Endocytosis: From Mechanisms to Potential Clinical Applications.* Cells, 2023. **12**(18).
191. Matthees, E.S.F., et al., *GRK specificity and Gβγ dependency determines a GPCR's potential in biased agonism.* bioRxiv, 2023: p. 2023.07.14.548990.
192. Zhang, Y., et al., *Intracellular localization and constitutive endocytosis of CXCR4 in human CD34+ hematopoietic progenitor cells.* Stem Cells, 2004. **22**(6): p. 1015-29.
193. Reiter, E. and R.J. Lefkowitz, *GRKs and beta-arrestins: roles in receptor silencing, trafficking and signaling.* Trends Endocrinol Metab, 2006. **17**(4): p. 159-65.
194. Wong, M., et al., *Dynamic Buffering of Extracellular Chemokine by a Dedicated Scavenger Pathway Enables Robust Adaptation during Directed Tissue Migration.* Dev Cell, 2020. **52**(4): p. 492-508.e10.
195. Podinovskaia, M., et al., *A novel live-cell imaging assay reveals regulation of endosome maturation.* Elife, 2021. **10**.
196. Vercauteren, D., et al., *Dynamic colocalization microscopy to characterize intracellular trafficking of nanomedicines.* ACS Nano, 2011. **5**(10): p. 7874-84.
197. Neves, M., et al., *The Role of ACKR3 in Breast, Lung, and Brain Cancer.* Molecular Pharmacology, 2019. **96**(6): p. 819-825.
198. Yu, S., et al., *The Role of G Protein-coupled Receptor Kinases in Cancer.* Int J Biol Sci, 2018. **14**(2): p. 189-203.
199. Nogués, L., et al., *G Protein-coupled Receptor Kinase 2 (GRK2) Promotes Breast Tumorigenesis Through a HDAC6-Pin1 Axis.* EBioMedicine, 2016. **13**: p. 132-145.
200. Fitzhugh, D.J., et al., *G Protein Coupled Receptor Kinase 3 (GRK3) Negatively Regulates CXCL12/CXCR4 Signaling and Tumor Migration in Breast Cancer.* Journal of Allergy and Clinical Immunology, 2011. **127**(2): p. AB230.
201. Yuan, L., et al., *Growth factor receptor-Src-mediated suppression of GRK6 dysregulates CXCR4 signaling and promotes medulloblastoma migration.* Mol Cancer, 2013. **12**: p. 18.
202. Raghuwanshi, S.K., et al., *G protein-coupled receptor kinase 6 deficiency promotes angiogenesis, tumor progression, and metastasis.* J Immunol, 2013. **190**(10): p. 5329-36.

203. Bebelman, M.P., et al., *The Convergence of Extracellular Vesicle and GPCR Biology.* Trends Pharmacol Sci, 2020. **41**(9): p. 627-640.
204. Bebelman, M.P., et al., *The forces driving cancer extracellular vesicle secretion.* Neoplasia, 2021. **23**(1): p. 149-157.
205. Vacchini, A., et al., *Phosphoproteomic mapping of CCR5 and ACKR2 signaling properties.* Frontiers in Molecular Biosciences, 2022. **9**.
206. Heuninck, J., et al., *Context-Dependent Signaling of CXC Chemokine Receptor 4 and Atypical Chemokine Receptor 3.* Mol Pharmacol, 2019. **96**(6): p. 778-793.
207. Nguyen, T.D., et al., *Recent Advances in Single-Molecule Tracking and Imaging Techniques.* Annual Review of Analytical Chemistry, 2023. **16**(Volume 16, 2023): p. 253-284.
208. Joseph, M.D., et al., *Quantitative Super-Resolution Imaging for the Analysis of GPCR Oligomerization.* Biomolecules, 2021. **11**(10).
209. Ribas, C., et al., *The G protein-coupled receptor kinase (GRK) interactome: role of GRKs in GPCR regulation and signaling.* Biochim Biophys Acta, 2007. **1768**(4): p. 913-22.
210. Martínez-Muñoz, L., et al., *Remodeling our concept of chemokine receptor function: From monomers to oligomers.* Journal of Leukocyte Biology, 2018. **104**(2): p. 323-331.
211. Levoye, A., et al., *CXCR7 heterodimerizes with CXCR4 and regulates CXCL12-mediated G protein signaling.* Blood, 2009. **113**(24): p. 6085-93.
212. Hemmen, K., et al., *Dual-Color Fluorescence Cross-Correlation Spectroscopy to Study Protein-Protein Interaction and Protein Dynamics in Live Cells.* J Vis Exp, 2021(178).
213. Kucia, M., et al., *Trafficking of normal stem cells and metastasis of cancer stem cells involve similar mechanisms: pivotal role of the SDF-1-CXCR4 axis.* Stem Cells, 2005. **23**(7): p. 879-94.
214. White, C.W., et al., *NanoBRET ligand binding at a GPCR under endogenous promotion facilitated by CRISPR/Cas9 genome editing.* Cell Signal, 2019. **54**: p. 27-34.